
**UNIVERSITY OF BIRMINGHAM**

# INVESTIGATION INTO THE EFFECT OF MESH SIZE ON ADSORBER BED PRESSURE DROP PERFORMANCE FOR SOLAR POWERED AIR CONDITIONING SYSTEM

**by**

**IZAZI AQILAH MOSLI**

**A thesis submitted to the University of Birmingham for the degree of MASTER OF SCIENCE BY RESEARCH**

**School of Mechanical Engineering**
**College of Engineering and Physical Sciences**
**University of Birmingham**
**January 2015**

**ABSTRACT**

Adsorption systems have the potential to provide cooling for air conditioning applications particularly in countries where solar energy is abundant. However, they suffer from low Coefficient of Performance (COP), being large and having high capital cost. New adsorbent materials like Metal Organic Framework (MOF) materials are being developed with enhanced adsorption properties; such materials show high potential to be used in the development of high efficiency adsorption cooling systems in research and commercial fields. In a typical adsorbent system the adsorbent material powder or granules are kept in the adsorber beds using fine mesh so that they will not be washed away by the refrigerant vapour. Therefore it is important to predict pressure losses across the adsorbent bed since this will have an impact on the bed design and system performance. This research presents experimental and numerical investigations to determine the effects of woven wire mesh size on pressure drop across the mesh using wire mesh sheets of size: 120x0.090, 150x0.047, 200x0.039 and 500x0.025 (wires per inch × mm). Also experimental tests and computational fluid dynamic (CFD) simulations were carried out for air flow across a representative unit of adsorber bed when packed with granular adsorbent material of 2 mm diameter as well as an empty honeycomb unit. Results showed that capsular cylinders can be used to model the granular material to give pressure drop predictions similar to experimental values and can be used to find permeability values of adsorbent materials without having to test experimentally. Also, the CFD studies showed that using 'Porous and Free Media Flow' to model the mesh and adsorbent materials gave similar pressure drop results to experimental values and can be used to predict pressure losses for large and complex adsorbent bed systems. Finally, CFD work showed that the pressure drop in the porous adsorbent material is significantly higher than that through the mesh sheets thus indicating that the effect of the mesh on the pressure drop performance is negligible.

**ACKNOWLEDGEMENTS**

First and foremost, I would like to express my sincerest gratitude to my supervisor Dr Raya Al-Dadah for her endless support and invaluable academic experience. I would also like to thank Dr Saad Mahmoud for his advice and most helpful input in the project progression, as well as Dr Ahmed Elsayed for the many different forms of learning help throughout my year in research. I would also like to truly thank Mr. Simon Rowan for many days of helping me in the laboratory, helping me produce and set-up the experiments and ensuring that tests go smoothly. Not to forget, I would like to thank the Government of His Majesty, the Sultan of Brunei Darussalam for giving me this opportunity to study in the form of a scholarship and for the financial support. Last but not least I would like to give a big thank you to my parents and close friends for their informal but nonetheless strengthening support in times of hardship.

# TABLE OF CONTENTS

**LIST OF FIGURES**

**LIST OF TABLES**

**ABBREVIATION**

| | |
|---|---|
| AC | Activated carbon |
| AlPO | Aluminophosphate |
| BTC | Bis(trichloromethyl) carbonate |
| CFD | Computational Fluid Dynamics |
| COP | Coefficient of Performance |
| CPC | Compound parabolic collector |
| CPO | Carbon Phosphate |
| DVS | Dynamic vapour sorption |
| FAM | Fluorescein amidite |
| HFC | Hydrofluorocarbon |
| HP | Heat pipe |
| LED | Light emitting diode |
| MAlPO | Metal Aluminophospate |
| MOF | Metal organic framework |
| PTC | Parabolic trough collector |
| SAPO | Silico-alumino-phosphate |
| SCE | Solar collector east |
| SCP | Specific Cooling Performance |
| SCW | Solar collector west |
| SPA | Solar powered adsoption |

**NOMENCLATURE**

| Symbol | Quantity | SI Unit |
|---|---|---|
| COP | Coefficient of Performance | - |
| d | Wire diameter | m |
| K | Permeability coefficient | $m^2$ |
| n | Wires per unit length | - |
| $p_0$ | Initial pressure | Pa |
| $p_{atm}$ | Absolute pressure | Pa |
| $P_c$ | Condensation pressure | Pa |
| $P_e$ | Evaporation pressure | Pa |
| $p_{ref}$ | Reference pressure | Pa |
| $p_S$ | Static pressure | Pa |
| $p_T$ | Total pressure | Pa |
| $\Delta$ p | Pressure difference | Pa |
| SCP | Specific cooling performance | $W.kg^{-1}$ |
| $T_{ambient}$ | Ambient temperature | K |
| $T_{atm}$ | Absolute temperature | K |
| $T_{cond}$ | Condensation temperature | K |
| $T_{evap}$ | Evaporation temperature | K |
| $T_{regeneration}$ | Regeneration temperature | K |
| u | Fluid velocity | $m.s^{-1}$ |
| $u_0$ | Initial velocity | $m.s^{-1}$ |
| $u_{ref}$ | Reference velocity | $m.s^{-1}$ |
| $\Delta$ x | Flow length | m |
| $\beta$ | Free hole area | - |
| $\epsilon$ | Void fraction or porosity | - |
| $\eta$ | Fluid viscosity | Pa.s |
| $\rho$ | Density of fluid | $kg.m^{-3}$ |

# *Chapter 1* : Introduction

## *1.1 Introduction*

Air-conditioning systems are required for thermal comfort in buildings and are increasingly seen as an essential aspect of a developed lifestyle. As world population increase there is an increase of built area and increase in time spent inside buildings and the requirement of enhanced building services and comfort level [1], especially in regions with warmer climates. It is predicted that from 2010 to 2035, the world energy demand will increase by 35 percent due to economic and population growth [2]. Presently, most air-conditioning systems use electrical power generated mostly from fossil fuels, to drive mechanical vapour compression systems. Some of conventional systems still contain environmentally harmful refrigerants such as R-12 or HFC's [3-4], which are now banned due to environmental regulations such as the Kyoto and Montreal Protocols. Solar powered air-conditioners employing adsorption systems are more environmentally friendly because adsorption systems do not involve any harmful chemicals and can utilise lower-grade heat thus reducing the use of high-grade electrical power. Furthermore, generation and utilization of renewable energy has received an increased interest to help meet the energy demand. Additionally, further improvements to existing adsorption air-conditioning systems can be done by using a wide range of new advanced material with enhanced performance, available in a range of sizes from granules to fine powder. Material in fine powder forms have better adsorption capabilities due to the absence of binders that is usually used to hold the shape of granule-form adsorbents. These binding materials hinder the mass uptake of active material and finding a method to contain the powder-form material that does not impede fluid flow can mean that it can be used in the design of high-efficiency adsorption systems.

### *1.2 Aims and objectives*

The main aim of this MSc Research project is to investigate the suitability of using fine mesh to securely contain adsorbent material for use in adsorbent beds by assessing the pressure drop characteristics of different mesh sizes.

To achieve the research aim, the objectives of this project are set out below.

1-Review of literature regarding computational and experimental research work of solar air-conditioning using adsorption cooling systems.

2-Review airflow and pressure drop studies of mesh sheets of different sizes.

3-Develop a computational fluid dynamics (CFD) simulation model of flow across single mesh sheets of various sizes.

4-Develop a computational fluid dynamics simulation model of flow across detailed model of adsorbent material in micro scale as part of two-stage CFD modeling method of representative beds.

5-Design and construct a test facility to help understand the effect of various mesh sizes and representative bed of adsorbent material on pressure drop.

6- Study the effects of mesh size on the pressure drop of airflow compared to pressure drop caused by adsorbent material.

### *1.3 Thesis outline*

This thesis consists of seven chapters. Chapter one introduces the research topic covered by this thesis. This section includes project aim, objectives and thesis outline.

Chapter two reviews new and existing research studies as well as progress on solar air-conditioning systems using adsorption cooling systems. It also explains the basic principles of adsorption systems, bed designs and mentions the variety of adsorbent materials that can be used in the design of adsorption cooling, including high performance adsorbent materials.

Chapter three presents the development of an experimental test rig to find pressure drop characteristics of airflow across a single sheet of woven wire mesh of various sizes. This section also describes the set up of the representative bed using honeycomb integrated with mesh, as well as the packing of adsorbent granules.

Chapter four presents the CFD analyses for the air flow through four sizes of woven mesh sheets. It describes the parametric analysis of modeling adsorbent material granules in micrometer scale in hexagonal cells and studying pressure drop with velocity. The granules are also modeled as cylindrical, spherical and capsular solids to compare the CFD predicted pressure drop. CFD pressure drop predictions were then done for flow across the honeycomb section, the honeycomb fitted with mesh and the honeycomb fitted with mesh and filled with granules using porous media flow physics

Chapter five presents experimental results of the set up of the wire mesh sheets of four sizes as well as pressure drop results across the representative bed of adsorbent material fashioned from a honeycomb section sandwiched between two mesh sheets of size 150 wires per inch×0.047 mm then with 500 wires per inch×0.025 mm. Pressure drop is recorded for the honeycomb unit when empty and then filled with adsorbent material granules.. This section also shows the experimental and CFD comparisons for the studies of single mesh sheet, empty and packed honeycombs, as well as the suitability of using the capsular granule modeling over the other two geometries when finding the permeability of adsorbent granules to be used in porous media modeling.

The study of the pressure drop caused by fine mesh and packed adsorbent material in adsorbent bed design is concluded in chapter six, where findings from the investigations are summarized and potential improvements are discussed.

# *Chapter 2* : Literature review

## *2.1 Introduction*

The adsorption cooling cycle is a thermodynamic cycle that consists of two heat sources and two heat sinks and operates using three temperature levels as shown in Figure 2.1. The cycle operates between two adsorbent-refrigerant concentration levels and between two pressures ($P_e$ and $P_c$) [5]. The refrigerant is also usually known as the adsorbate. Process 1-2 in Figure 2.2 shows the adsorbent bed with high concentration of refrigerant being heated up by the high temperature source ($T_{regeneration}$) to dissociate or desorb the refrigerant from the adsorbent, which causes the pressure within the adsorbent bed to rise from $P_e$ to $P_c$. Process 2-3 is the continued heating by the same temperature source, $T_{regeneration}$ and 2-3` is showing the condensation of the refrigerant when the bed is connected to the condenser and passed back into the evaporator (3`-4`). The adsorbent bed containing low concentrations of refrigerant is then cooled to $T_{ambient}$ and pressure is also reduced (3-4). The low pressure, low concentration bed is then cooled (4-1) and readsorbs the refrigerant vapour from the evaporator. The cooling effect is achieved at $T_{evap}$ as the liquid refrigerant is evaporated (4`-1) to be able to be adsorbed by the bed.

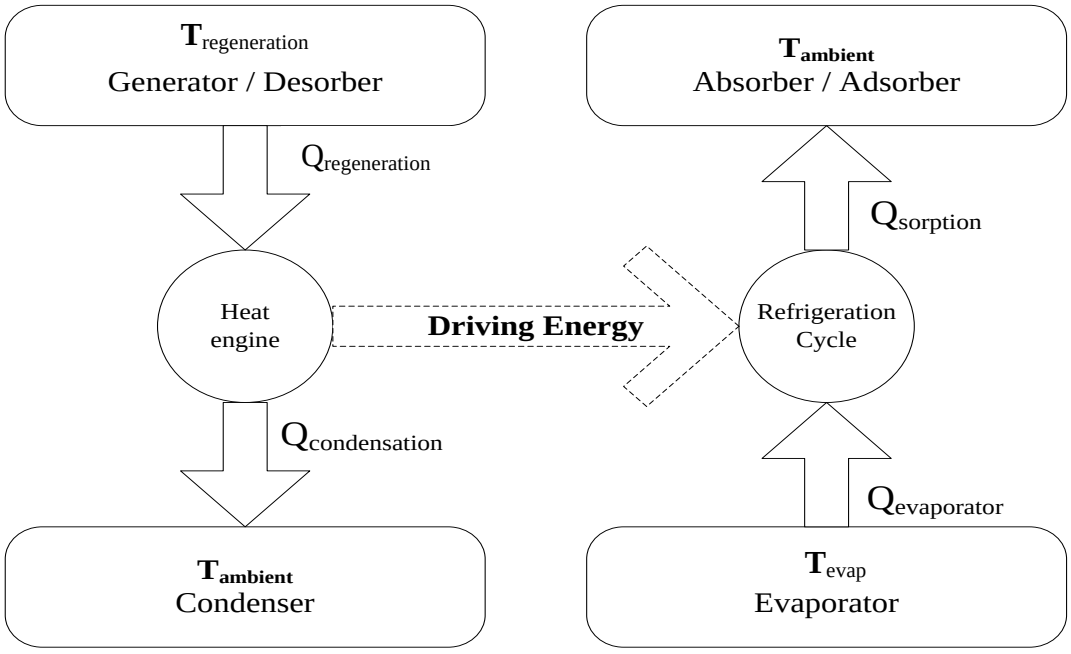


**Figure 2.1 Adsorption thermodynamic cycle [5]**

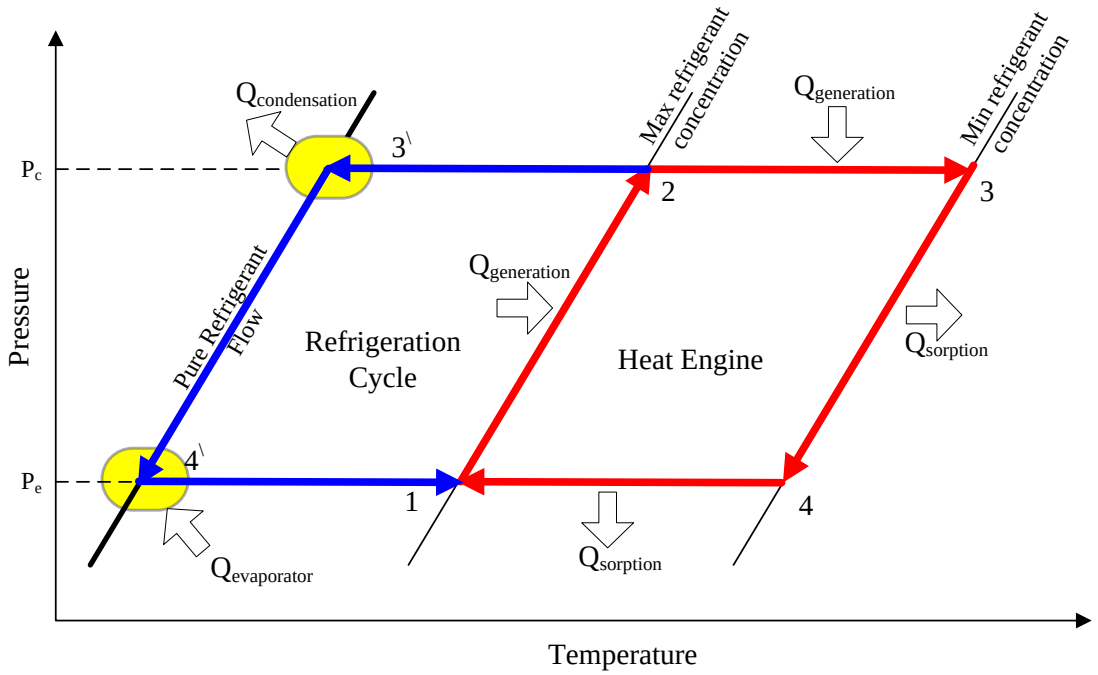


**Figure 2.2 Sorption Clapeyron diagram [5]**

The conventional cycles used in the bed designs can either be single or multi-beds cycles. A single bed adsorption system works by alternating processes of adsorption and desorption and cooling is achieved intermittently. A dual or multi-bed design can have two or more cycles at different stages of adsorption/desorption. For example, in a dual bed design, the first bed could be undergoing desorption while the other undergoes adsorption and vice versa so cooling can be achieved continually as long as the regeneration heat energy is provided. Due to this, the dual or multi-bed adsorption system is more commonly used in practical and experimental applications. There are also other available cycle operation strategies such as incorporating heat and mass recovery, cascading and thermal wave cycles but these methods have limited practical applications [6-7].

An example of a multi-bed system is from an experimental investigation by Saha *et al.* (2001) of a double-stage, four bed, non-regenerative adsorption chiller powered by low-grade solar heat sources between 50 to 70°C [8]. The prototype in the experiment produced a cooling power of 3.2 kW with a COP of 0.36 when $T_{regeneration}$ was 55 and condensation temperature was 30°C. Flat plate collectors were used to produce hot water at 55°C, for adsorbent regeneration in the chiller.

Luo *et al.* (2007) has also built a novel solar-powered adsorption cooling systems for low-temperature grain storage, using silica gel-water adsorption pair [9]. The chiller in Figure 2.3 has two identical adsorption units that were operated out of phase to improve the system efficiency and continuity of cooling, in addition to using heat and mass recovery processes. There was 49.4 $m^2$ of all-glass evacuated tube solar collectors to produce a desorption temperature of 70°C. The system had an average specific cooling power (SCP) ranging from 66 and 90 W per $m^2$ collector surface, with maximum SCP of 4.4 $kWkg^{-1}$ for the whole system. The daily solar cooling COP for the grain bin reached a maximum of 0.13 and the temperature in the grain storage box was kept below 14°C.

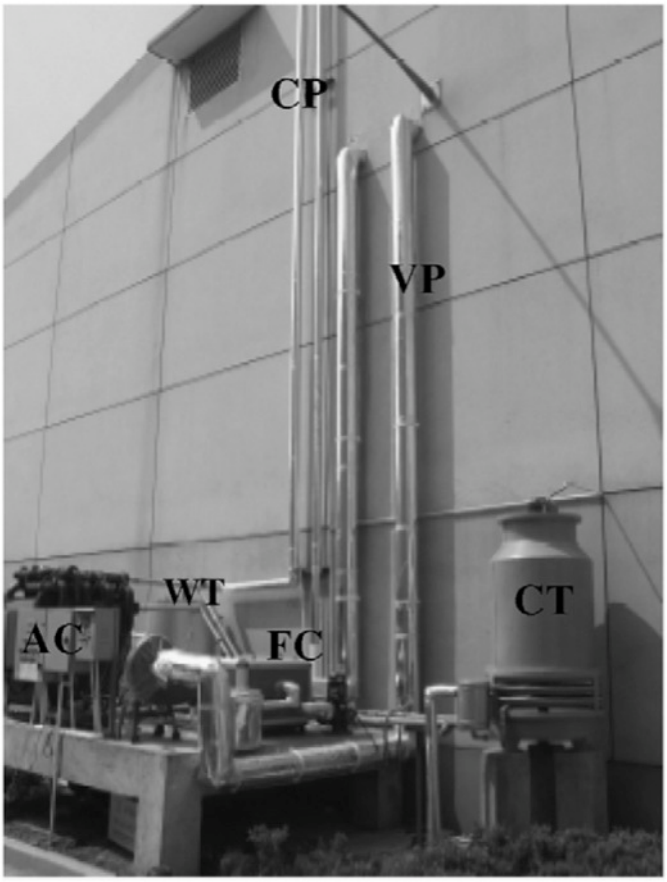


**Figure 2.3 Photograph of the grain storage experiment. AC, adsorption chiller; CT, cooling tower; FC, fan coil unit; WT, partitioned hot water tank; CP, solar collector water pipes; VP, ventilation pipes [9]**

Lu *et al.* (2013c) conducted experimental research on solar adsorption air conditioning using microporous silica-gel/water as the working refrigeration pair [24]. In the dual

bed design, each of the adsorbent bed contained 65 kg of microporous silica-gel. Experiments were conducted under typical summer weather conditions and the average COP was evaluated to be 0.44, with a solar COP of 0.16. When the regeneration, condensation and evaporation temperatures were 79°C, 25.4°C and 13.7°C, respectively, the COP reached 0.63 and the cooling capacity was 17.9 kW

Throughout the literature review, there are more examples of dual and multi-bed systems, but they are from studies that focus on bed design improvement, novel solar collector designs or application of high performance adsorbent materials.

### *2.2 Existing solar-driven adsorption technology*

Table 2.1 highlights work carried out in the field of solar powered air conditioning systems highlighting the working pairs, operating conditions, type of solar collectors and performance outcomes.

## Table 2.1 summary of solar powered conditioning systems

| Author | Solar collector | Working pair | Type of study | Tregeration (°C) | Tcond (°C) | Tevap (°C) | adsorption COP | Solar COP | Cooling capacity (kW) | SCP (W/kg) |
|---|---|---|---|---|---|---|---|---|---|---|
| Abu Hamdeh et al. (2010) [10] | Flat plate collector | Methanol/activated carbon | Experimental | 110 | 25 | 8 | 0.68 | 0.18 | 0.07 | |
| Fadar et al. (2009) [11] | Parabolic trough collector | Ammonia/activated carbon | Modelling | 100 | 30 | 0 | 0.43 | 0.18 | 0.03 | 104 |
| Zhai (2008) [12] | U-type evacuated tubular and heat pipe evacuated tubular | Silica gel/water | Experimental | 85 | 32 | 18 | 0.35 | 0.15 | 19 | |
| Ferreira-Leite (2011) [13] | Flat plate collector | Methanol/activated carbon | Modelling | 105 | | | 0.6 | | 20 | 39.7 |
| Restuccia et al. (2004) [14] | Flat plate collector | Silica gel-CaCl2/water | Experimental, modelling | 90 | 35 | | 0.6 | | 20 W/kg | 20 |
| Clausse (2008) [15] | Enhanced compound parabolic | Methanol/activated carbon | Modelling | 130 | 15 | 10 | 0.49 | 0.2 | 4.6 kW | 230 |
| Habib et al. (2013) [16] | Triple coated evacuated glass tube | Silica gel/water | Experimental, modelling | 80 | 20 | | 0.52 | | 7 kW | |
| Santori et al. (2012) [17] | Flat plate collector | Silica gel/water | Modelling | | | | 0.18 | | 4.1 kW | 69.3 |
| Nunez et al. (2004) [18] | Flat plate collector | Silica gel/water | Experimental | 75-95 | 25-35 | 10-20 | 0.4-0.6 | | 3.5 kW | |
| Alam et al. (2013) [19] | Compound parabolic concentrator (CPC) | Silica gel/water | Modelling | 85 | 30 | | 0.55 | 0.3 | 10 kW | |
| Tchernev (1982) [20] | Flat plate collector | Z13X/water | Experimental | 120 | 40 | 10 | | 0.15 | | |
| Lu (2013a) [21] | Compound parabolic concentrator (CPC) | Silica gel/water | Experimental | 65 | 30 | 15 | 0.36 | 0.16 | 7.5 kW | |
| Lu (2013b) [22] | CPC with mass recovery | Microporous silica gel/water | Experimental | 55-80 | 30 | 15 | 0.50-0.53 | | 15.3-15.8 kW | |

| **Author** | **Solar collector** | **Working pair** | **Type of study** | **Treg °C** | **Tcond °C** | **Tevap °C** | **adsorption COP** | **solar COP** | **Cooling capacity** | **SCP** W/kg |
|---|---|---|---|---|---|---|---|---|---|---|
| Lu et al. (2011) [23] | n/a | Silica gel/water | Experimental | 57-80 | 27 | 15 | 0.32-0.41 | - | 3.6-5.7 kW | - |
| Lu et al. (2013c) [24] | n/a | Microporous silica gel/water | Experimental | 79 | 25 | 13 | 0.63 | - | 17.9 kW | - |
| Buchter et al. (2003) [25] | Flat plate collector | Activated carbon/methanol | Experimental | 100 | 27-38 | 0 | - | 0.13 | - | - |
| Luo et al. (2007) [9] | Evacuated tube | Silica gel/water | Experimental | 68-90 | 32 | - | - | 0.096-0.13 | - | - |
| Thomas et al. (2012) [26] | Flat plate collector | N/A | Experimental, modelling | 55-65 | - | - | 0.47 | - | 9 kW | - |
| Hassan (2011) [27] | Flat plate collector | Activated carbon/methanol | Modelling | 60 | - | - | - | 0.211 | - | 2.326 |
| Hassan et al. (2013) [28] | Flat plate collector | Activated carbon/methanol | Modelling | 120 | 35 | 0 | 0.66 | - | 183 W | 1.59 W/kg |
| Alghoul et al. (2009) [29] | Evacuated tube | Activated carbon/methanol | Modelling | 98 | 30 | -5 | 0.44 | 0.091 | - | - |
| Chekirou et al. (2013) [30] | Flat plate collector | Activated carbon/methanol | Modelling | 82.5 | 30 | -5 | 0.424 | 0.143 | - | - |
| Wang et al. (2009) [31] | Solar cooling tube | Silica gel/water | Experimental | 85 | 30 | - | 0.5 | - | 2.5 kW | 85 W/kg |
| Zhao et al. (2012) [32] | Evacuated cooling tube | Zeolite/water | Experimental | 223 | 31.6-40.5 | 10-15 | 0.215 | - | 12 kW | - |
| Benelmir et al. (2012) [33] | Flat plate collector | Silica gel/water | Experimental | 55-95 | 22-37 | - | 0.6 | - | 8 kW | - |
| Yang et al. (2006) [34] | n/a | Silica gel/water | Experimental | 85 | 30 | - | 0.446 | - | 790 W | - |
| Ara Rouf et al. (2013) [35] | Compound parabolic collector | Silica gel/water | Modelling | 87 | 31 | - | 0.6 | 0.35 | 10 kW | - |
| Abdul Majeed et al. (2014) [36] | Evacuated tube collector | Activated carbon fibre/ethanol | Experimental | 55-95 | 30 | 7 | 0.63 | - | 12 kW | - |
| Li et al. (2003) [37] | Evacuated cooling tube | Zeolite/water | Modelling | 200 | 35 | 10 | 0.255 | - | - | - |
| Hossain et al. (2013) [38] | n/a | Activated carbon/ammonia | Experimental | 110 | 40 | -10 | 0.22 | - | 4 kW | - |
| Abu Hamdeh et al. (2013) [39] | Parabolic trough collector | Olive waste/methanol | Modelling | 120 | 25 | 8 | 0.75 | 0.18-0.2 | - | - |

Kalogirou (2004) compared the efficiency of different types of solar energy collectors as well as the operating temperatures [40]. For flat plate collectors, the range is from 30°C and only up to 80°C while an evacuated tube collector has a range of 50-200°C. With compound parabolic collectors, the indicative temperature range reaches 240°C when stationary and up to 300°C with single-axis tracking. A cylindrical trough collector has the range of 60-300°C and a parabolic trough collector 60-400°C.

Abu Hamdeh and Al-Muhtaseb (2010) designed a prototype of a solar adsorption cooling unit using activated carbon-methanol as the adsorbent-adsorbate pair [10]. Figure 2.4 shows four flat plate collector of area of 1.39 $m^2$ each were tilted at 40 degrees above ground. The minimum temperature reached by the unit was 9°C at ambient temperature of 26°C. The temperature decrease was achieved in 4 hours 20 minutes and the gross cycle coefficient of performance was calculated to be 0.688. The maximum regeneration temperature $T_{regeneration}$ was 110°C, with condensing temperature, $T_{cond}$, and evaporating temperature, $T_{evap}$, were 25 and 8°C, respectively. The solar coefficient of performance was up to 0.18 with collector area of between 3.5 and 4.6 $m^2$. Figure 2.5 shows the contour plot of the COP of the system as a function of adsorbent mass and collector area, and that the optimum value of COP lies in the region when the collector area is between 3 and 4.5 $m^2$, and adsorbent mass between 40 to 50 kg.

**Figure 2.4 Solar adsorption system prototype [10]**

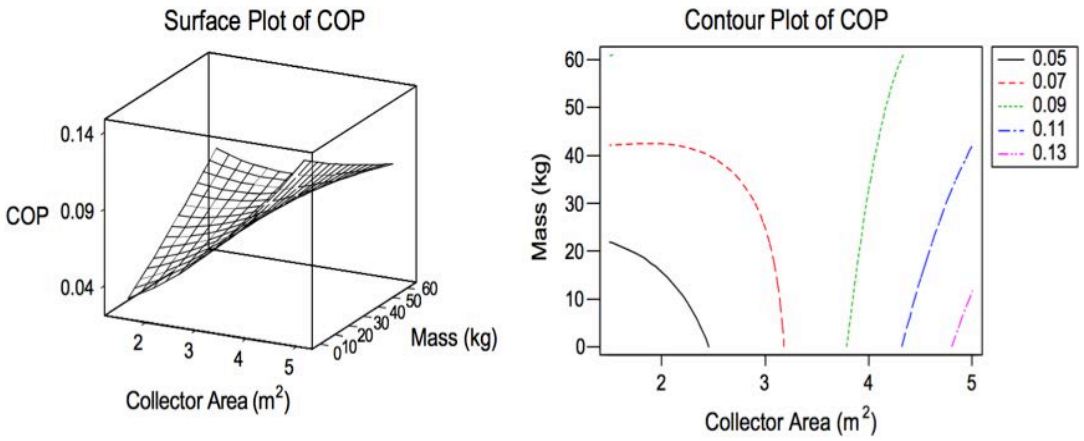


**Figure 2.5 Response surface of the COP of the system as a function of mass and collector area, contour plot of the COP as a function of mass and collector area [10]**

An analysis on the operation of a small-scale solar cooling system based on adsorption was done by Thomas *et al.* (2012) based on a laboratory located in temperate Belgium [26]. Using flat plate solar collectors of 14 $m^2$, the COP was monitored for different time scales, as well as cooling capacity of the adsorption chiller (Figure 2.6) that has a nominal power of 9kW. Using solely solar driven cooling, the COP of the system was found to be about 0.47 at driving temperature, $T_{regeneration}$ of about 55-65°C. Due to the region's temperate climate, the solar air-conditioning system with 14$m^2$ was concluded to not save energy compared to classical air-conditioning due to cloudy conditions, low driving temperature and intermittent operation.


**Figure 2.6 Solar air-conditioner with adsorption machine (left) and dry cooling tower (right) [26]**

Benelmir *et al.* (2012), in France, has analysed by experimentation the performance of an adsorption chiller fitted into a cold chamber ceiling (Figure 2.7) that was integrated in a basic micro-cogeneration technology system with a solar system [33]. Along with analysis of performance and effectiveness, the study showed the interest in such tri-generation systems especially the usability in areas with a large solar field. The flat plate solar collectors provided regeneration temperatures from 55°C up to 95°C for the working pair silica gel and water. The system produced a cooling capacity of 8 kW and the COP was calculated to be about 0.6.

**Figure 2.7 Inside the cold chamber (left) and the chilled ceiling (right) installed with adsorption chiller [33]**

In Ouagadougou, Burkina-Faso, Buchter *et al.* (2003) built and tested an adsorptive solar refrigerator with integrated adsorber and solar collector unit [25], using activated carbon and methanol as the working pair. The solar collector is single glazed flat-plate selective collector (Figure 2.8), has an area of 2 $m^2$ and produces a driving temperature of around 100°C. The condenser temperature is similar to ambient, which is about 27-38°C depending the time of day. The experimental value of the solar COP reached a value of 0.13. This study supports the development of adsorption technology for air conditioning and the possibilities for sahelian and tropical climates.

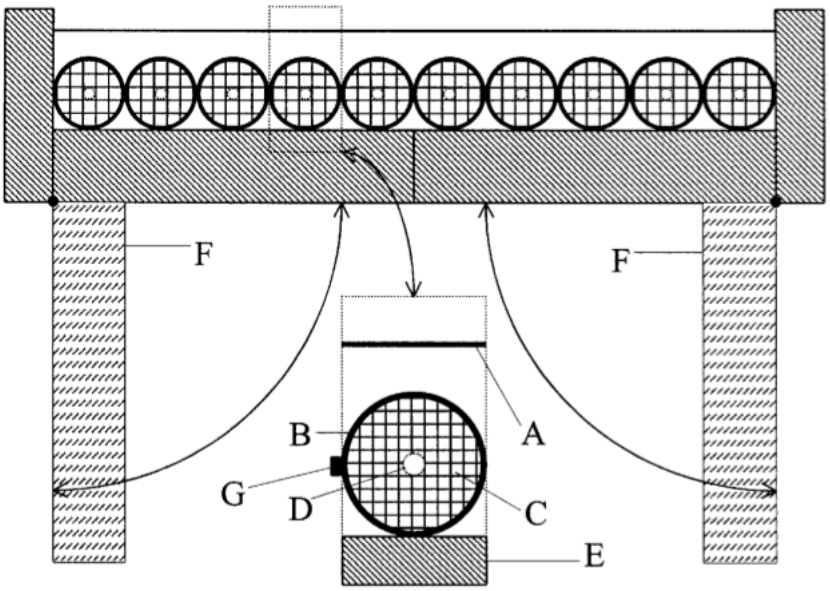


**Figure 2.8 Schematic of Buchter's (2003) solar collector-adsorber: glass cover (A), tube covered with selective surface (B), active carbon (C), central tube for vapour transport (D), thermal insulation around the collector (E); insulating dampers also shown in open position (F) [25]**

Zhai *et al.* (2008a) reported on the experiences of solar thermal utilization in China that included solar hot water systems with different design methods in residential buildings and solar-powered integrated energy systems in public buildings [41]. The report discussed the different types of solar collectors being employed in adsorption cooling systems such as evacuated tubular, flat plate, U-type tubular with CPC and all glass evacuated collectors. It was also mentioned that the collector type must be chosen to adapt to the building façade and the building integration should have a sensible combination of functions. For example, solar collectors may form multifunctional building components such as act as balcony sideboard, exterior facing wall or awning. In one of the examples mentioned, 150 $m^2$ of U-type solar collectors (Figure 2.9) were used to provide 15 kW of cooling, with a maximum of 21 kW in summer.

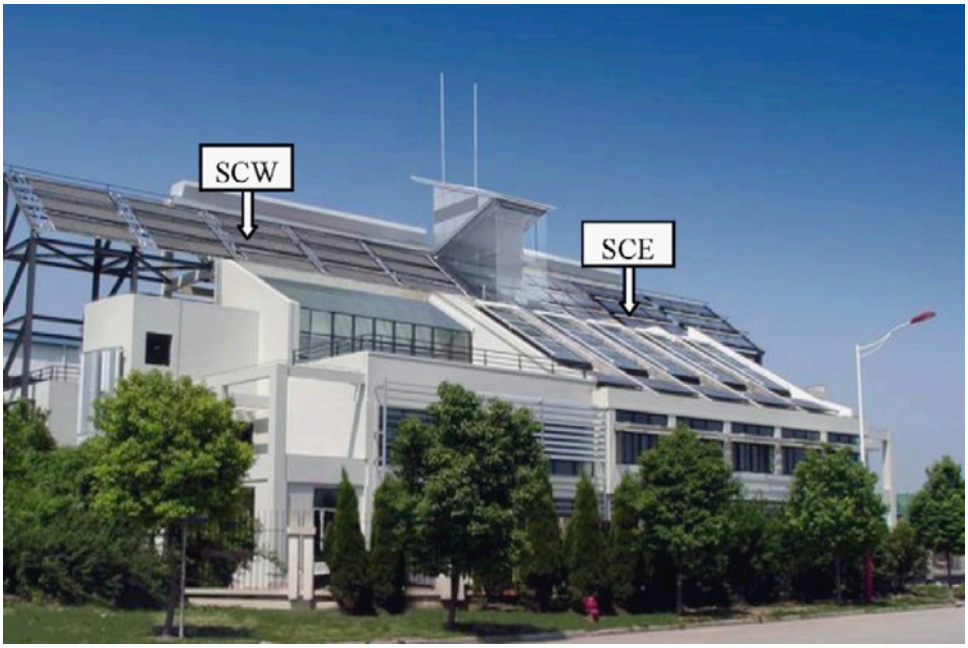


**Figure 2.9 Green building integrated with solar collector with east (SCE) and west (SCW) sides [41]**

Evacuated tube collectors can be used to supply hot water close to 100°C for systems requiring higher regeneration temperatures. In Malaysia, a dual-purpose solar adsorption refrigerator and water heater was tested by Alghoul *et al.* (2009) [29]. The chiller has two adsorber beds of carbon AC-5060/methanol pair, and regeneration temperature of 98°C was provided by evacuated tube solar collectors. During operation, the condenser temperature $T_{cond}$ was 30°C and $T_{evap}$ of the evaporator was -5°C. The cycle COP was found to be 0.44 and the solar COP for the chiller was 0.091. It was suggested that the system performance can be improved further by using high efficiency solar collectors such as heat sheets and using better quality adsorbent such as activated carbon fibre.

Also in Malaysia, the performance of a solar driven two-bed adsorption air-conditioning system was studied by Abdul Majeed *et al.* (2014) [36]. In their work, the regeration temperature is provided by evacuated tube solar collectors and activated carbon fibre and methanol was used as the adsorption pair. It was found that the chiller system can deliver an evaporation temperature of 7°C and be driven by temperature ranging from 55 to 95°C. When the regeneration temperature is set at 85°C and the condenser temperature is 30°C, the cooling

capacity is 12 kW and COP is 0.6. However, when the cooling water temperature in the condenser is lowered, the cooling capacity was increased up to 20 kW.

Zhai (2008b) designed a solar-powered adsorption air-conditioning system and installed it in the green building of Shanghai Research Institute of Building Science [12]. The system used 90 $m^2$ of U-type evacuated tubular solar collectors with compound parabolic collectors and 60 $m^2$ of heat pipe evacuated tubular solar collectors (Figure 2.10), and the air-conditioning was optimized by maintaining a phase shift of 540s between two adsorption chillers. The study used silica gel/water as an adsorption working pair and a hot water temperature of 85°C for regeneration. The cooling power obtained by the system was 15.3 kW and the system COP was 0.35 with solar COP of 0.15.

**Figure 2.10 Heat pipe solar collector arrays (left) and U-type evacuated tubular solar collector array (right) [12]**

In Paris, Clausse *et al.* (2008) has installed an adsorption air-conditioning system that uses enhanced compound parabolic solar collectors [15] as the heat source for desorption, with activated carbon and methanol acting as a working pair. Indoor temperature was kept below 25°C during five testing days with ambient temperature of 31°C. The average cycle COP was 0.49 and the solar COP was 0.2 with regeneration temperature reaching 130°C due to the Compound Parabolic Concentrator's (CPC) increased efficiency. In one day, it was recorded that the unit can produce cooling effect totaling 42.7 kWh.

Lu (2013a) conducted a study of a novel solar adsorption cooling system using 105 $m^2$ of new CPC collectors shown in Figure 2.11 by investigating a two-phase

thermo-syphon silica gel-water solar adsorption chiller [21]. The regeneration, condensation and evaporation temperatures were 65, 30 and 15°C respectively. The cooling capacity is 7.5kW and the COP is 0.36.

**Figure 2.11 Medium temperature evacuated tube Compound Parabolic Concentrator collector [21]**

Lu (2013b) further improved on the performance of the adsorption air-conditioning by mass-heat recovery to increase the COP of a microporous silica gel-water adsorption chiller (Figure 2.12) [22]. The system can be driven by temperatures of 50-80°C. The study showed that when the hot water temperature is lower, longer mass recovery time is needed for the readsorption of the cold adsorption bed and the redesorption of the hot adsorbent bed. When the regeneration temperature is 55°C, the COP can reach 0.31 with 180 seconds of mass recovery compared to the 0.27 COP with just 90s recovery. With a regeneration temperature of 80°C, the COP was 0.50 without heat recovery and increased to 0.53 with 30 s heat recovery.

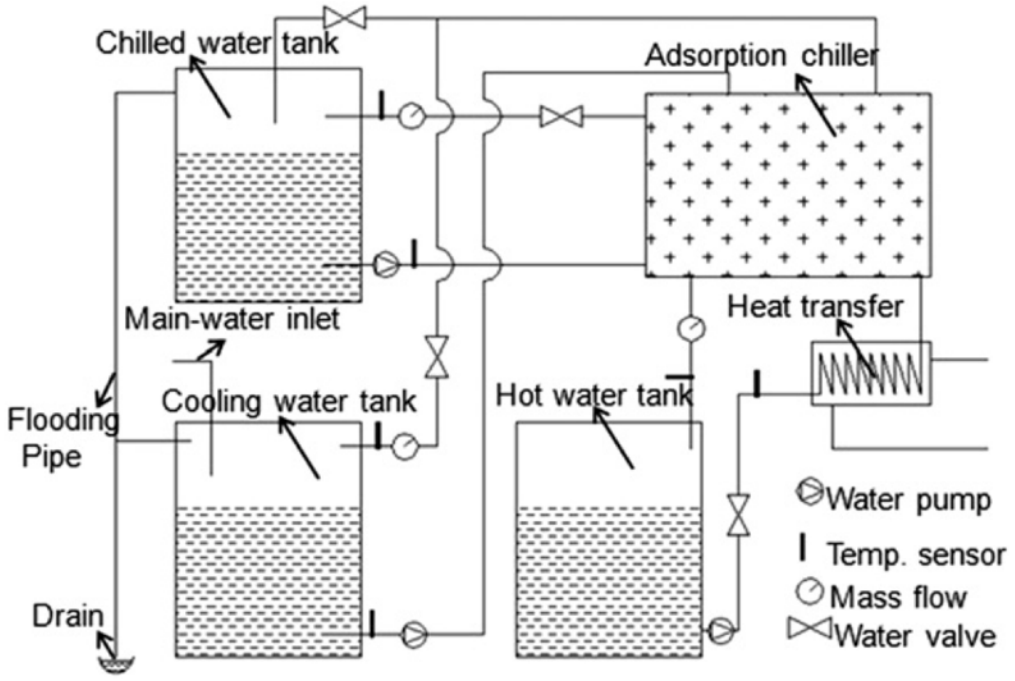


**Figure 2.12 Schematic diagram of Lu's [22] adsorption chiller test**

In terms of modeling, Hassan *et al.* (2011) has introduced a theoretical simulation model for a tubular solar adsorption refrigeration system that uses activated carbon and methanol [27] where the model represents the heat and mass transfer inside the adsorption bed, the condenser, and the evaporator (Figure 2.13). A solar flat plate collector with area 1 $m^2$ was used in the model integrated with 20 stainless steel tubes containing the adsorption working pair. In this case, the driving temperature for regeneration starts at 60°C and it was found that when the regeneration temperature reaches 120°C, the methanol starts to decompose. The solar coefficient of performance was calculated to be 0.211 and the specific cooling power was 2.326 W/kg. In a follow up study [28], Hassan and Mohamad (2013) addressed the challenge of producing continuous 24-hour adsorption air-conditioning cooling power by using a movable supporting frame installed with a flat plate collector (Figure 2.14). The analysis used the Dubinin-Astakhov adsorption equilibrium equation and the system coefficient of performance was calculated to be 0.66. The cooling capacity of this new system was found to be 183 W and the specific cooling power was 1.59 W/kg.

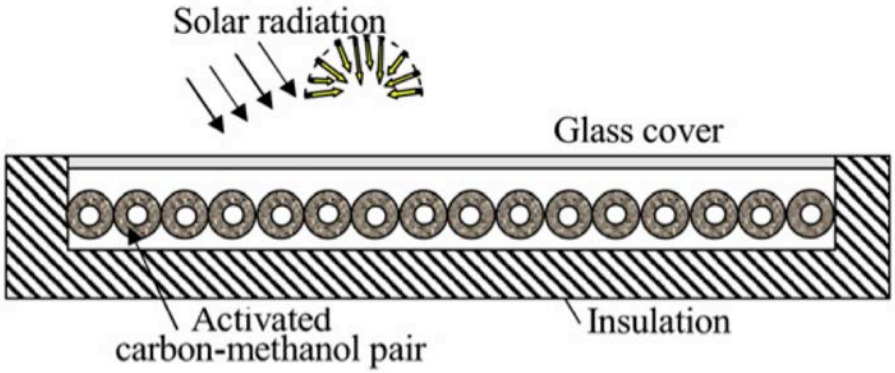


**Figure 2.13 Configuration diagram of the solar adsorption cooling reactor [27]**

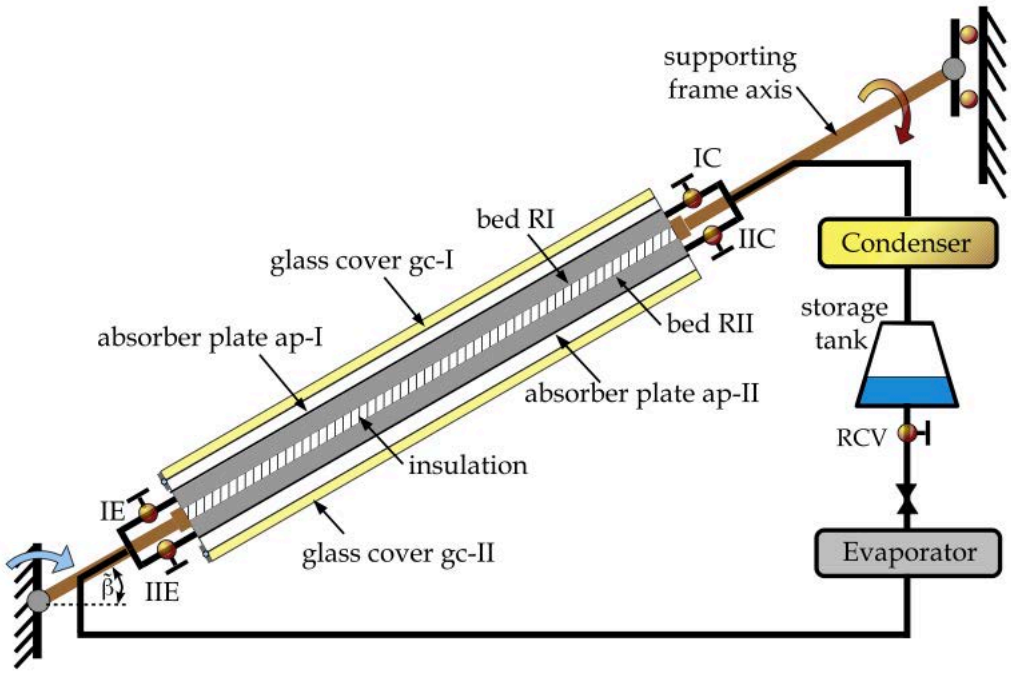


**Figure 2.14 Schematic of the continuously operating system [28]**

A solar powered two bed adsorption air conditioning system was investigated by Sumathy and Li (1999) using a simple lumped parameter model [45]. The system was driven by three configurations of flat-type solar collector with different glazes: single glaze cover, double glaze cover and transparent insulation material cover. The three different glazes made no big difference on performance. With

collector area of 3 $m^2$, the average SCP for the three configurations was 13 W/kg and the solar COP were between 0.07 and 0.08.

A study was made by Fadar *et al.* (2009) on a solar adsorption cooling machine [11] where a parabolic trough collector (PTC) of area 0.8 $m^2$ heats up the reactor and is coupled with a heat pipe (HP) shown in Figure 2.15. The reactor contains a porous medium of activated carbon as the adsorbate with ammonia as the adsorbent. A heat source temperature of 100°C was reached with $T_{cond}$ of 30°C and $T_{evap}$ of 0°C. With these conditions, the system achieved SCP of 104 W/kg, a refrigeration cycle COP of 0.43 and solar COP reaching 0.18.

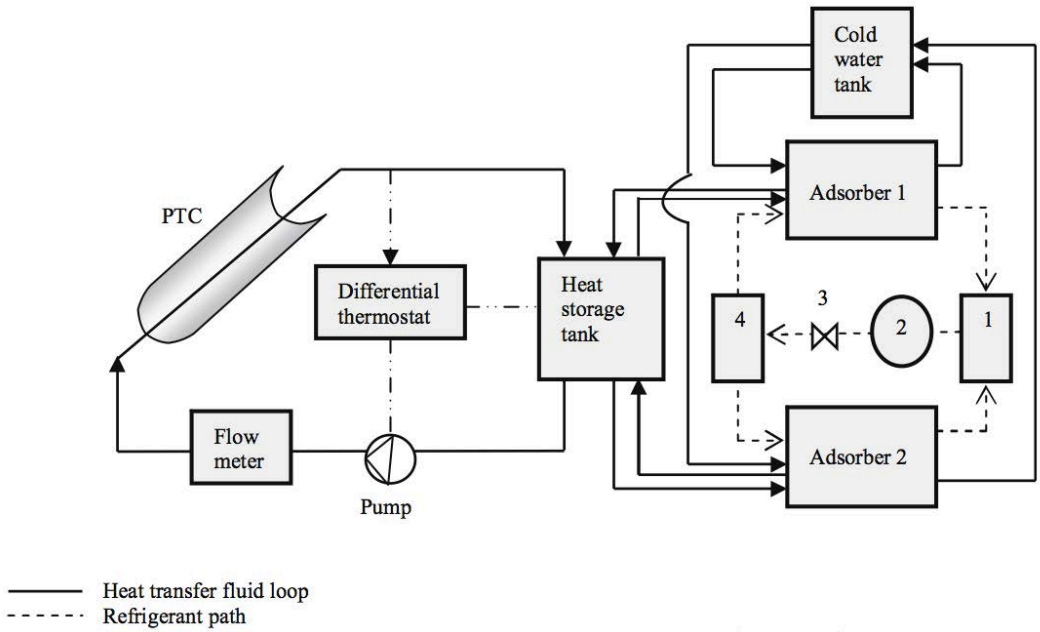


**Figure 2.15 Schematic of adsorption system utilising parabolic trough collector: 1. condenser; 2. ammonia tank; 3. expansion valve; 4. Evaporator [11]**

Alam *et al.* (2013) has used the climatic conditions of Tokyo, Japan, to set up an analytical investigation to study the possibility of application of solar cooling [19]. A lumped parameter model has been used to investigate the performance of the system, when using silica gel and water adsorbent/adsorbate pair. Based on the solar radiation data, it was found that at least 36.2 $m^2$ of compound parabolic

solar collector area (Figure 2.16) was required to achieve the required heat source temperature of 85°C for operating the cooling unit. The model also predicted that the cooling unit provided a cooling capacity of around 10 kW with a solar COP of around 0.3 and system COP of 0.55. It was also mentioned that the size of the solar collector could be reduced by optimizing the cycle time.

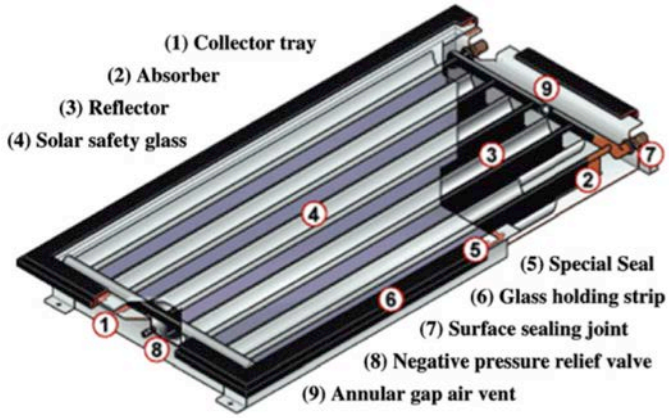


**Figure 2.16 Solar powered adsorption cooling unit modeled by Alam *et al.* [19]**

Similar to the above, Ara Rouf *et al.* (2013) also ran a simulation to study the effect of operating conditions on the performance of solar powered adsorption chiller using the climatic conditions of Dhaka, Bangladesh [35]. The numerical system saw the analysis of 13 CPC collectors of area 2.42 $m^2$ each, required to reach the driving temperature of 87°C. When the condenser temperature $T_{cond}$ is 31°C, the chiller is capable of producing 10kW of cooling, giving a cycle COP of 0.6 and solar COP of 0.35. This model also used silica gel-water as the working pair in the simulation.

Abu Hamdeh *et al.* (2013) designed and analysed performance characteristics of a solar adsorption refrigeration system that used a parabolic trough collector (PTC) to drive the adsorption desorption cycle [39]. The system used olive waste as adsorbent and methanol as adsorbate. The maximum generation temperature achieved was 120°C and during operation, condensing temperature was 25°C and evaporating temperature was 8°C. From the results, it was found that the best possible value of the cooling production located in the zone where the adsorbent mass ranged from 30 to 40 kg, and collector area between 3.5 and

5m$^2$. With these conditions, the calculated cycle COP was 0.75 with a solar COP of 0.18-0.2, and the minimum temperature achieved within the unit (Figure 2.17) was 4°C.

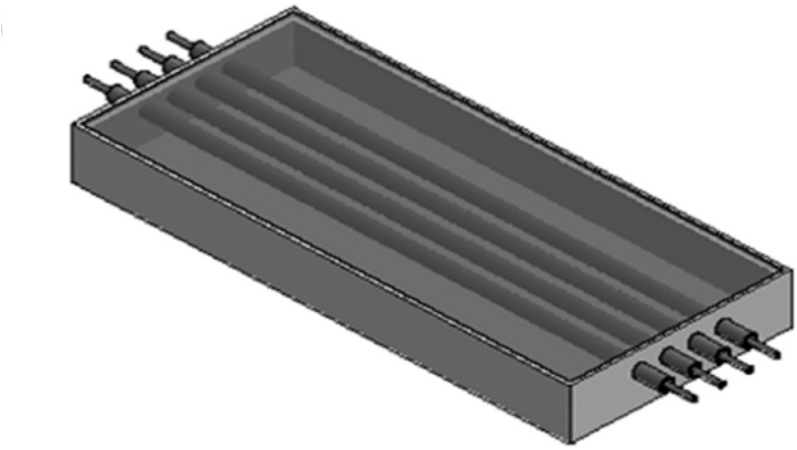

**Figure 2.17 Adsorption unit adopted by Abu Hamdeh [39]**

Henning (2007) raised some issues concerning the use of solar thermal energy for air conditioning of buildings in his report that compiled and described some examples of installation of such applications in Europe [43]. It was mentioned that at that time in 2006, there were about 70 solar cooling systems installed in Europe that used solar collectors but included absorption and dessicant cooling. The total collector area of the installations was about 17, 500 m$^2$ which showed the progression and interest in solar powered air conditioning. However, only 11% involved adsorption due to the bulky nature of the technology. An example of adsorption cooling systems given in the paper is one installed in Freiburg, Germany. The system ran a 10 kW cooling capacity using 170 m$^2$ of evacuated tube solar collector. The COP was calculated to be 0.6 during time of day when high solar fraction occurs. However, for this installation, the electrical consumption for the cooling tower cycle was seen as too high.

In an experimental study, Lu *et al.* (2011) investigated the performance of a novel silica-gel water adsorption chiller with self-balance device of refrigerant [23]. The results of this study showed that self-balance of refrigerant can improve reliability of the chiller. When the driving temperature, condenser temperature and evaporation temperature were 57°C, 27°C and 15°C,

respectively, the COP was 0.32 and the cooling capacity was 3.6 kW. However, when the driving temperature was increased to 80°C, the COP reached 0.41 and the cooling capacity increased up to 5.7 kW.

The effect of driving temperature is further investigated by Afshar *et al.* (2012) [44], who presented a review to compare the importance of solar collector design and efficiency compared to adsorption bed design, which can be used as a guideline to designing a solar air-conditioning system. The most important part of the solar refrigeration system was the collector because efficiency in thermal engines or COP in cooling systems depends on driving temperatures as well as the evaporation temperatures. Using a parabolic solar collector instead of a plate collector may increase efficiency in cooling and thermal system, and although designing trough collectors is difficult and costly, COP and SCP achieved may be higher.

In some of these experiments and modeling, a solar collector area that is too big can decrease the COP when having an aperture area of beyond $5m^2$ for low tank volumes. This is due to the fact that the cooling production does not increase much once the water reaches above 100°C. With the further increase in the water temperature as a result of increasing collector area, the cooling production remains stable but the COP decrease. Also as seen from the Table 2.1, the range of COP values of solar adsorption cooling systems is from 0.3 to 0.7 approximately and this value can be considered quite low and presents the biggest limitation of the technology's commercial development.

### *2.3 Adsorbent bed designs*

In addition to the effects of solar collector designs and performance, there have also been many studies done that focus on the adsorbent bed and heat exchanger design improvements. Some examples of these designs have configurations such as tube and plates, fins, tube and fins, adsorption cooling tubes, evacuated tube adsorber. All these design improvements aim to facilitate heat transfer between adsorbent material and the regeneration heat source.

One of the works by Wang and Zhang (2009) was the design of an adsorption cooling tube [46] and an adsorption heat pump with multi-cooling tubes (Figure 2.19). The cooling tube uses a small-scale adsorption unit also called the shell which consists of one tube with two hemispherical heads (Figure 2.18) where the adsorber, evaporator and condenser are all housed in. The working pair in this study is silica gel and water and there is 15.1 kg of adsorbent per tube. For the model, the designed cooling capacity of the heat pump was 2.5 kW when the driving heat source temperature was 85°C. The whole unit was calculated to have a COP of 0.5 and SCP of 85 W/kg. Additionally it was also concluded in the study that the cyclic heating-cooling time and increase of the hot water temperature both increase the COP but the former is more effective than the latter. However for SCP, heating-cooling time has minimal effect but the SCP will double when the hot water is increased from 65°C to 90°C.

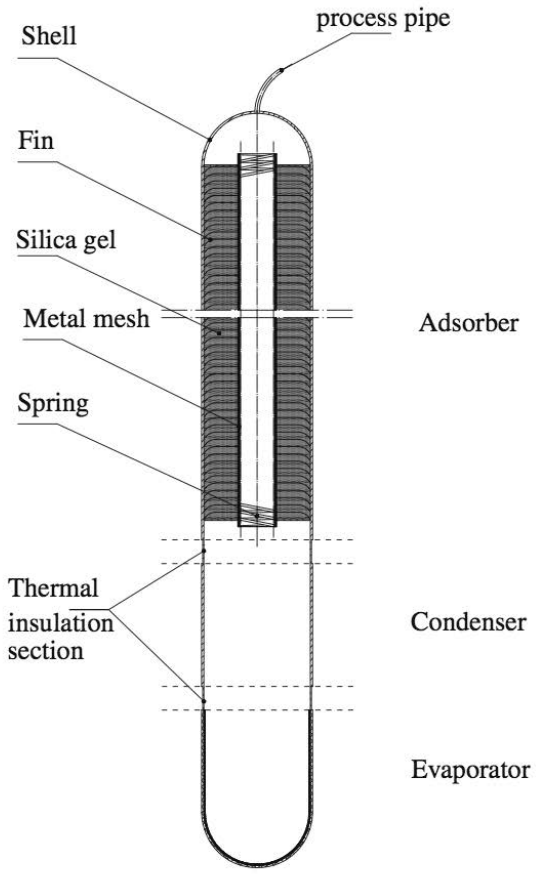


**Figure 2.18 Structure of cooling tube [46]**

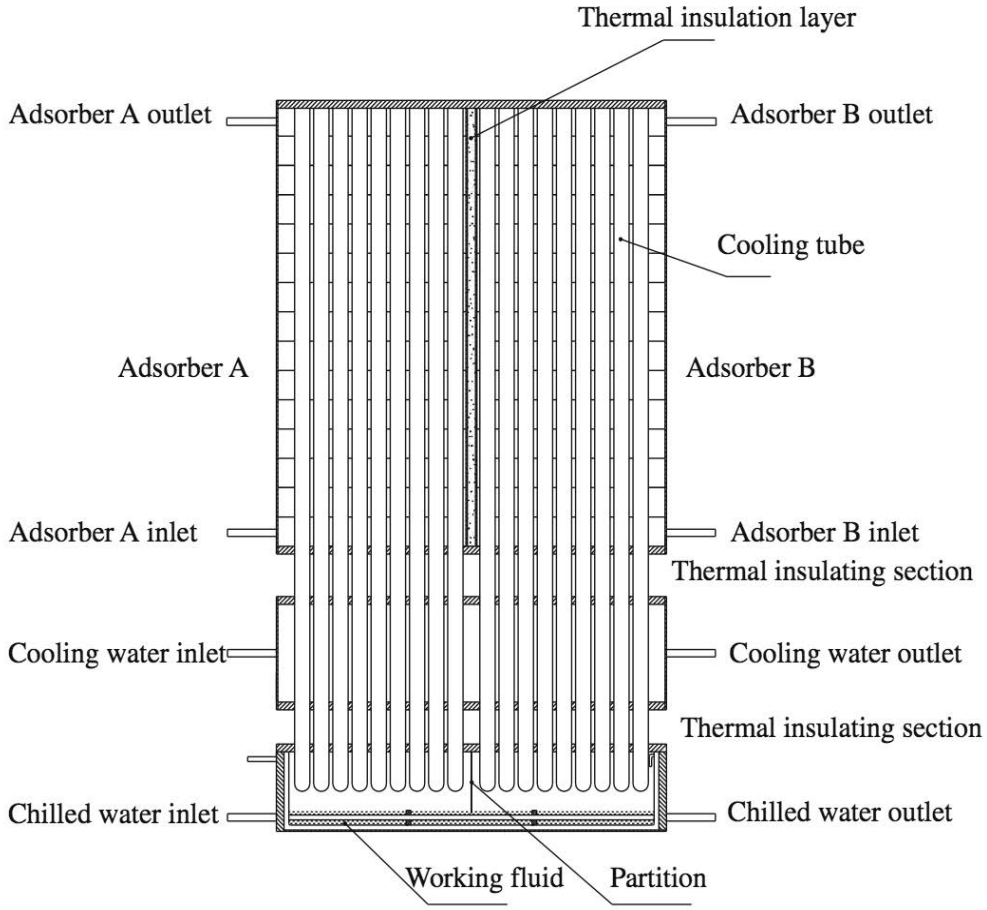


**Figure 2.19 Whole unit with multiple cooling tubes [46]**

Another experiment that involved a solar cooling tube was one conducted by Zhao *et al.* (2012) [32], who also studied the use of thermal/vacuum emptying method. A thermal vacuum pump was combined with vacuum pump method to increase the vacuum state of the solar cooling tubes and reduce the thermal loss of the adsorbent bed, which employed 13X zeolite and water as the working pair. The cooling tube (Figure 2.20) containing the adsorbent bed is exposed to solar energy so acts as the solar collector and can reach up to 233°C to give the desorption thermal energy for the zeolite. The condensation and evaporation temperature ranges were 31.6-40.5°C and 10-15°C, respectively. The cooling power of each of the tubes were evaluated to reach a maximum of 12 W and the COP of the solar cooling tube is about 0.215.

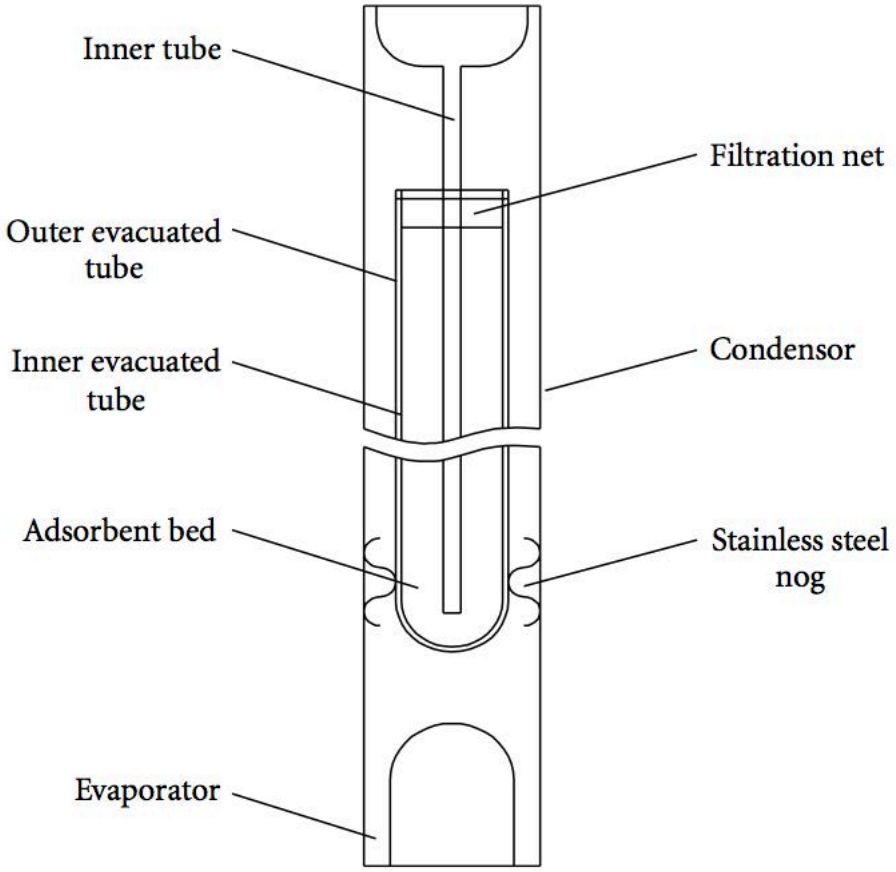


**Figure 2.20 sketch of Zhao's solar cooling tube [32]**

Hossain *et al.* (2013) built a prototype of a polygeneration system that can run on pure plant oils, such as Jatropha or Pongamia, or standard diesel fuel [38], constructed using a compression ignition engine of 9.9 kW shaft output. The adsorption refrigeration system is driven from the engine water jacket heat and uses a tube and fin exchanger in the design. The adsorption unit consists of 4 bed of activated carbon of 7.25 kg each and ammonia is used as the adsorbate. When a regeneration temperature of of 110°C is provided, and condensation and evaporation temperatures are 40°C and -10°C, respectively, a cooling load of 4 kW is produced and the system COP can be calculated to be 0.22.

A compact adsorption room air conditioner with a cooling capacity of 1 kW has been designed by Yang *et al.* (2006) [34], and two prototypes have been built for experiment and research, employing microporous spherical silica gel and water as the working pair for adsorption. The conditions used in the experiments were

regeneration temperature of 85°C and condenser temperature of 30°C. The second prototype was a modified version of the first with improved assembly accuracy and redesigned methanol evaporator fins (Figure 2.21), where the water condensate is removed quickly to improve heat removal and therefore cold production. The new design gave a cooling capacity of 790 W for the unit and a COP of 0.446.

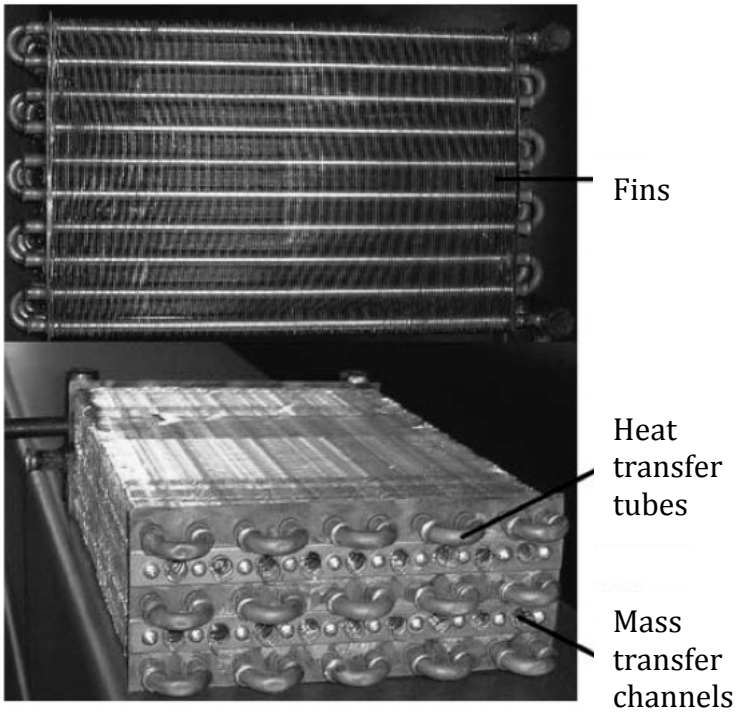


**Figure 2.21 Compact adsorption unit [34]**

An adsorption air-conditioning system was developed by Wang (2001) with two carbon adsorbers and using methanol as a refrigerant [31]. In this study, the effect of cycle time on COP and cooling power was found to be significant. A cycle time of 30 minutes gave a COP of 0.15 and a cooling power of 3.84 kW while a cycle time of 60 minutes gave a COP of 0.21 and a cooling power of 3.03 kW. Wang then repeated the experiment exchanging the adsorbers with tube and plate heat exchangers (Figure 2.22), the carbon placed outside the tubes, between the plates. The new design gave a COP of 0.4 and cooling power of 3.80 kW when regeneration temperature was 100°C and cycle time of 50 minutes.

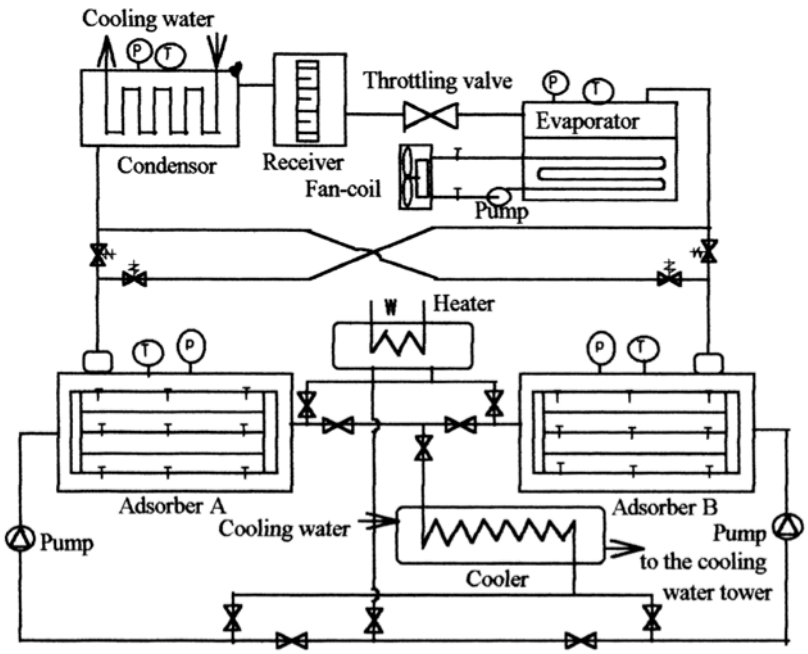


**Figure 2.22 Schematic of the adsorption heat pump system with plate heat exchanger [31]**

Chekirou *et al.* (2003) presented a modeling and analysis of heat and mass transfer in the tubular adsorber of a solar adsorption cooling machine [30]. The adsorber porous material was made of activated carbon AC-35 reacting by adsorption with methanol (Figure 2.24). For the simulation, the carbon adsorber were contained in nine copper tubes (Figure 2.23) and integrated with 1 $m^2$ of flat plate collector. In the study, the maximum regeration temperature was 82.5°C, $T_{cond}$ was set as 30°C and the evaporation temperature $T_{evap}$ was -5°C. The results achieved was a system COP of 0.424 and solar COP of 0.143, with the ideal mass of adsorbent investigated to be 35.05 kg for the system and ideal solar collector surface area of 1 $m^2$ for the highest COP.

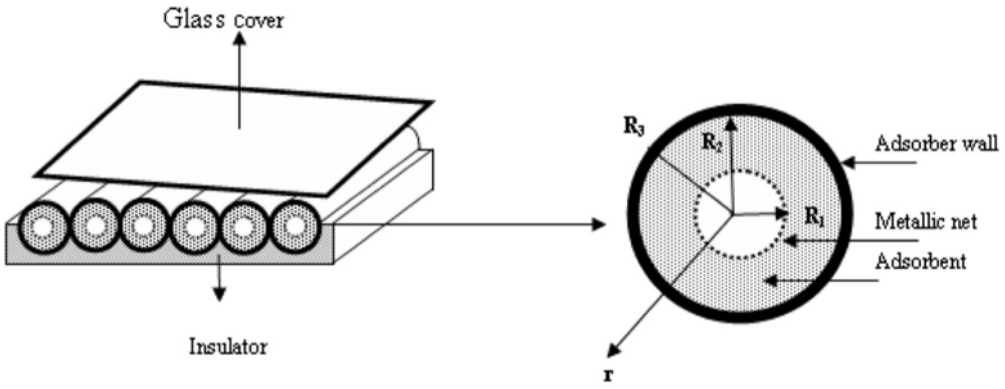


**Figure 2.23 Diagram of the adsorptive reactor coupled to the solar collector [30]**

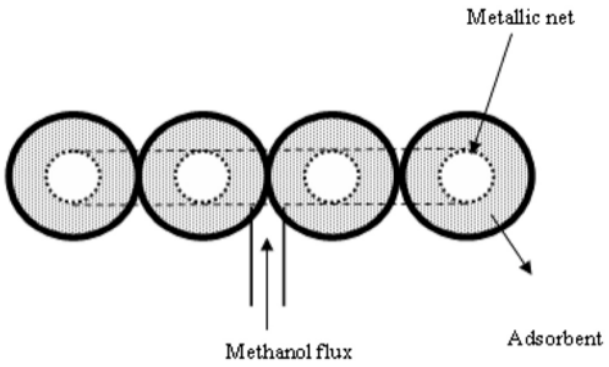


**Figure 2.24 Link tubes of the adsorber [30]**

To study the heat transfer of an evacuated tube applied in solar-power adsorption refrigerator, Li *et al.* (2003) conducted a detailed analysis and simulation of inhomogenous radiation heat transfer [37] between the inner and outer tubes (Figure 2.25), the back plate and interaction of sunlight reflection. The numerical calculations have been done with a zeolite-water pair for the evacuated tube adsorber. This study also included an economic analysis and defined a new cost effective parameter called the Solar Powered Adsorption (SPA) where a larger value indicates better economic performance. Using this economic analysis, and with zeolite adsorbent, it was calculated that the optimum thickness of adsorbent is about 10mm. However, the COP reaches its maximum value of 0.255 when the tube diameter is 70mm and adsorbent thickness is 15 mm. The calculation and analysis in this study used the parameters of 35°C cooling temperature and 10°C as evaporation temperature.

The driving temperature in the evacuated tube can reach up to 200°C average depending on the time of day and the diameter of evacuated tube.

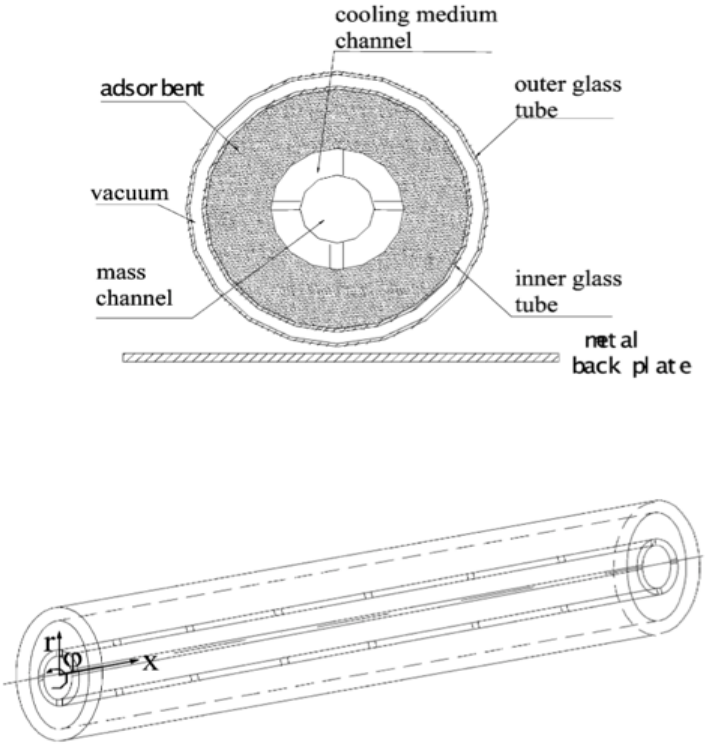


**Figure 2.25 evacuated tube adsorber cross section (top) and third-angle projection (bottom) [37]**

### *2.4 Adsorbent materials*

There are various adsorbent-refrigerant pairs that can be used in air-conditioning because sub-zero temperatures are not required and water can be used as an adsorbate (refrigerant) without the risk of freezing. Additionally, air-conditioning systems do not demand as high specific cooling performances compared to refrigeration and ice-making applications so these adsorption systems can be integrated into common domestic solar energy collector. Flat plate solar collectors can be used with systems utilizing a regeneration temperature of 80-90°C and systems requiring higher temperatures can use evacuated tube collectors. As mentioned previously and in Table 2.1, the most conventional adsorbent pair that have been used are silica gel/water [9, 12, 16-19, 21, 23, 31, 33-35] and activated carbon/methanol [10, 13, 15, 25, 27-30,]. Other pairs are activated carbon/ammonia [11, 38], silica gel-$CaCl_2$/water [14],

zeolite or Z13X/water [20, 32, 37], microporous silica gel/water [22, 24] and olive waste/water [39].

New adsorbent materials that have been developed include materials such as Metal Organic Framework (MOF) [54, 55], large-pore zeolites (SAPO, MAIPO, AlPO) [52, 53], and mesostructured silicates [63]. Adsorbent materials can either have a crystalline structure or an amorphous structure, where atoms are not arranged in an ordered structure. An example of an amorphous adsorbent material is silica gel, which can adsorb water most readily compared to other refrigerants or adsorbates. Silica gel is usually in the form of beads or granules made using sodium silicate. As mentioned above, silica gel is normally used as an adsorbent pair with water, but can also be used with ethanol [47] and methanol [48]. Microporous silica gel [22, 24] also known as high density silica gel and can adsorb water 2.75 times that of regular density silica gel [49]. Restuccia *et al.* (2004) developed an adsorption chiller that employed silica gel impregnated with $CaCl_2$ as sorption material [14]. This adsorbent was chosen because it has high sorption ability of up to 0.7 kg of water per kg of dry sorbent, and most of the water content can be desorbed at generation temperatures between 90 and 100°C. When the condensation temperature was 35°C, the COP of the chiller was close to 0.6 in the range of generation temperatures from 85 to 95°C, but it varied between 0.3 and 0.4 when the condensation temperature was 40°C. The SCP was 20 W/kg when the generation temperature was 95°C and the condensing temperature was 40°C.

Activated carbon can be used in adsorption cooling systems in the form of pellet, granules or powder to adsorb refrigerants such as ammonia, ethanol and methanol, because the surface of activated carbon is non-polar due to surface oxides and inorganic impurities. Carbonaceous raw material such as olive waste [39], oil palm biomass [50] and similar seed-based materials can be classified within this group. Carbon materials are carbonized at temperatures of around 800 °C in inert gases and activated by exposing it to oxygen or steam.

An example of crystalline adsorbent material is the zeolite group [51] including microporous aluminasilicate minerals. These materials adsorb water and their hydrophilic ability is related to the silicon/aluminium ratio. The lower this ratio is, the more aluminium ions present to attract water molecules [32, 37]. Zeolites require high regeneration temperatures of about 200 °C [32,37] and therefore not suitable for low generation temperature applications. Metal aluminophosphates (AlPOs) have pore structures similar to zeolites but have better adsorption performance compared to silica gel and zeolites [52]. Silica-aluminophosphates (SAPOs) are examples of AlPOs and have been used in research of advanced adsorption cooling technologies.

Chen *et al.* (2014) conducted a study to investigate the hydrothermal stability of SAPO-34 in adsorption refrigeration applications and used an intelligent gravimetric analyzer to study the water adsorption performance of SAPO-34. The equilibrium water uptake reaches 0.35 kg/kg of dry adsorbent, 25% higher than that of zeolite 13X. Most importantly, SAPO-34 showed no significant decrease in cyclic water uptake over a 60-cycle run of adsorption and desorption [53], showing excellent hydrothermal stability with the regular cubic-like morphology kept well (Figure 2.26) and presented suitable adsorption performance for application in adsorption refrigeration.

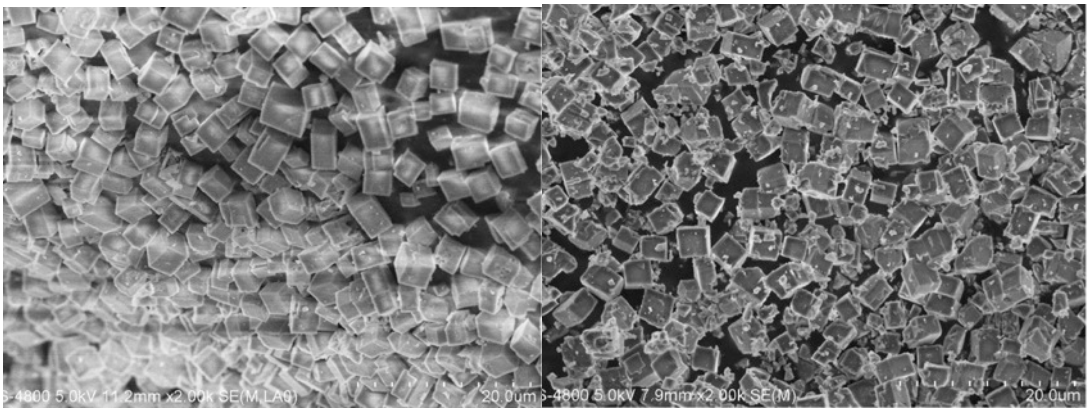

**Figure 2.26 SEM micrographs of fresh (left) and aged (right) SAPO-34 [53]**

Figure 2.27 shows the water loading performance of various adsorbent materials that include silica gel, AlPOs and SAPOs [52]. Even though the SAPO-34 and AlPO-18 have slightly lower adsorption capabilities by mass after Cu-BTC, SAPO-

34 and AlPO-18 have better hydrothermal stability with higher desorption temperature at 95 °C.

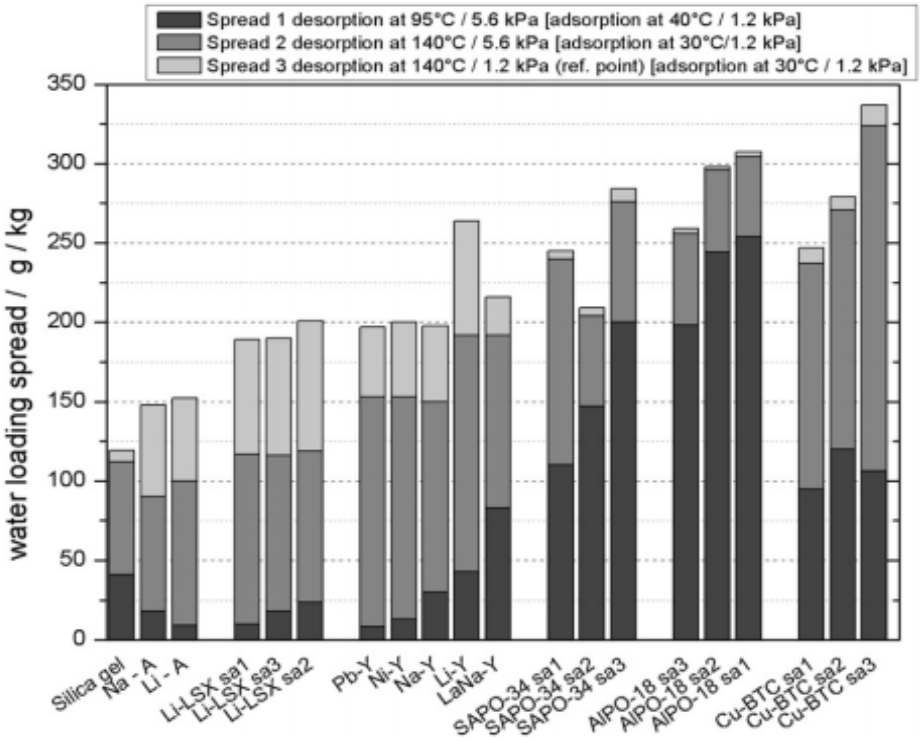


**Figure 2.27 Comparison of water loading spread for three cycle conditions for different materials with respect to the reference adsorbent mass at 140C and 1.2 kPa water vapour pressure [52]**

Metal Organic Framework (MOF) material are crystalline adsorbents with clusters of metal ions connected by carboxylates, phosphonates, or N-functional groups, also known as organic linkers. These advance materials have enhanced performance and adsorption capabilities reaching 1.3 $g.g^{-1}$ for MIL-101(Cr) [54] as shown in Figure 2.28.

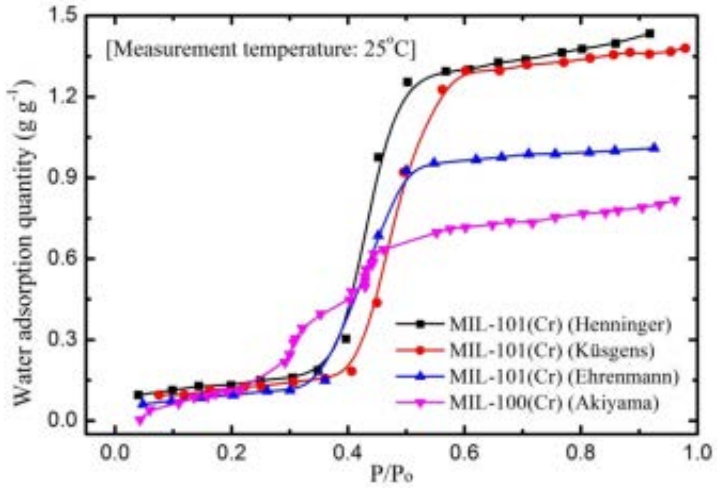


**Figure 2.28 MIL-101(Cr) developed in defferent laboratories [54]**

Figure 2.29 shows the water uptake versus partial pressure of various MOFs compares to silica gel and zeolite (NAX13) from research done by Al-Dadah [55]. MIL-101 showed the highest uptake by mass exceeding 1.4 but can only be reached at partial pressure of 0.5. CPO-27Ni showed the fastest water uptake at low partial pressures.

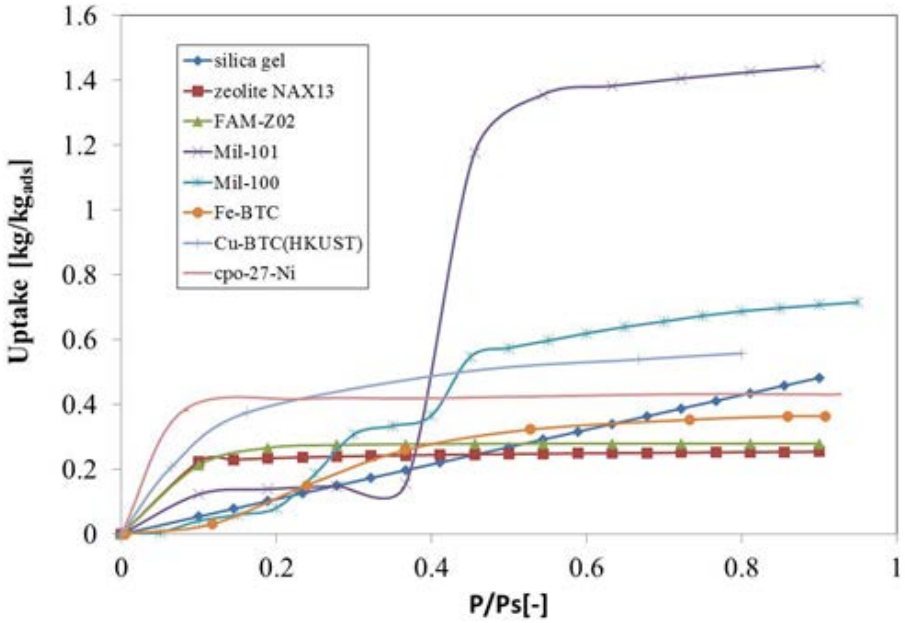


**Figure 2.29 Water uptake of wide range of adsorbent materials [55]**

From the same research, the material CPO-27Ni was characterized and the particle size was profiled from a 2 kg sample (Figure 2.30). Table 2.2 shows the range of diameters taken from the sample and the average particle diameter was

37.7 µm, so must be contained by mesh sheets with effective pore diameters smaller than that.


**Figure 2.30 sample of CPO-27Ni of various granule sizes [55]**

**Table 2.2 Showing the diameters of CPO-27Ni powder**

| | **JIM CPO-27Ni powder** |
|---|---|
| **$D_{10\%}$ (µm)** | 6.7 ± 0.4 |
| **$D_{16\%}$ (µm)** | 9.6 ± 0.6 |
| **$D_{50\%}$ (µm)** | 30.2±1.7 |
| **$D_{84\%}$ (µm)** | 68.7±6.1 |
| **$D_{90\%}$ (µm)** | 80.7±5.9 |
| **$D_{99\%}$ (µm)** | 124.8±13.2 |

Additionally, MOFs in powder form show better adsorption performance when compared to tablet form that contains binders. Figure 2.31 shows the adsorption curves for powder form CPO-27Ni where the lines overlap for the eight sorption cycles, which means that there is no cyclic degradation or loss in terms of performance. On the other hand, CPO-27Ni tablets shows that the adsorption by mass performance decreases as the sorption cycles progresses from 1 to 8, where the lines do not overlap and each subsequent sorption cycle shows lower adsorption capabilities by the tablets compared to the previous cycle. This shows that powder form is preferable and studying a method of containing powder MOF can mean that the design and production of adsorption systems with improved COP can be designed.

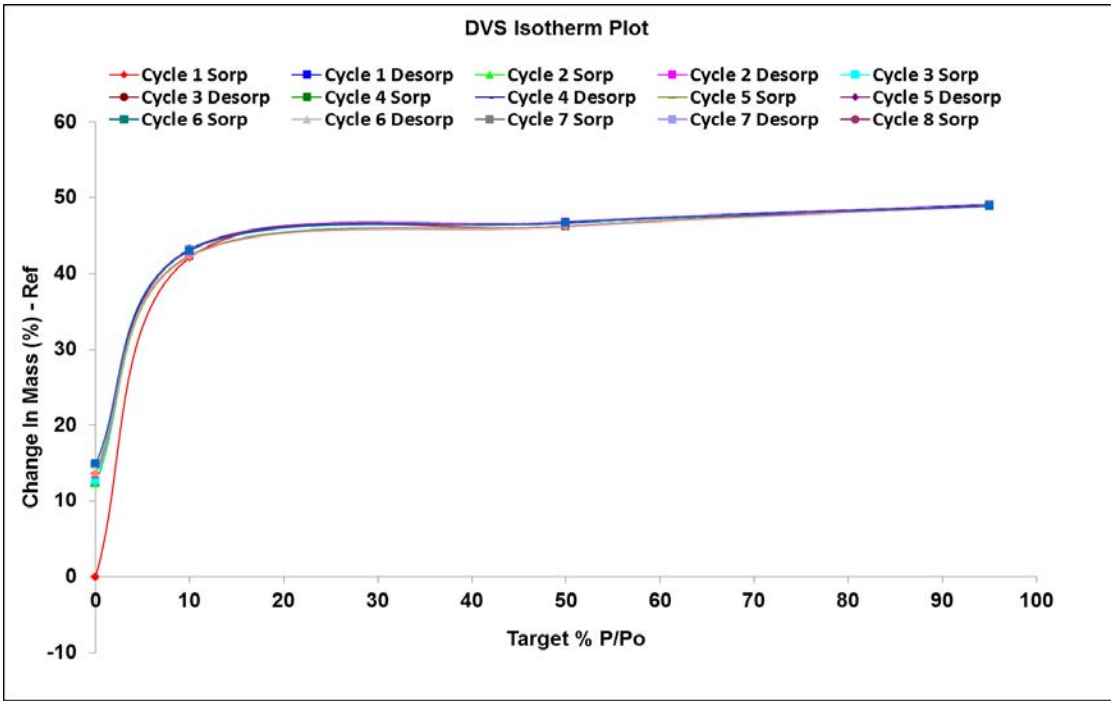


**Figure 2.31 Dynamic Vapour Sorption Isotherm plot for CPO-27Ni powder [5]**

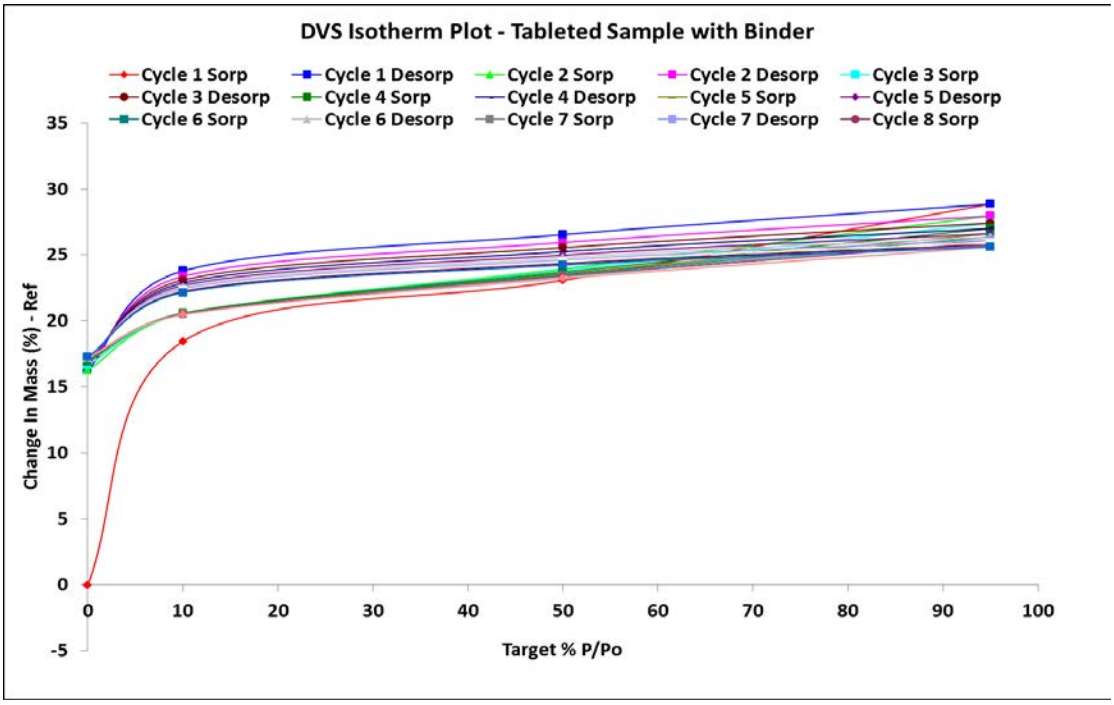


**Figure 2.32 Dynamic Vapour Sorption Isotherm plot CPO-27Ni tablets with binder [55]**

### *2.5 Flow in mesh and porous media*

As concluded from above, the disadvantages of presently developed adsorber bed cooling systems include low COPs of between 0.3 to 0.7. Additionally, these adsorption air-conditioning units tend to be very bulky due to the adsorbents being in the solid state and cannot flow as well as the low specific cooling powers of units that employ conventional adsorption materials such as silica gel. The challenges that are posed with designing a compact and efficient adsorbent bed cooling system is to improve heat transfer of the adsorbent material and to use higher performance adsorption pairs.

These high performance adsorbent materials that have been developed have very high adsorbing capacity and would increase COP if used in adsorption cooling and examples of these materials are zeolites such as SAPO-34 and metal-organic framework like CPO-27Ni. MOFs in fine powder form have higher adsorption efficiency with an uptake of up to 0.4kg/$kg_{ads}$ [55] and finding a suitable method of fine powder confinement would mean that designing and developing a compact solar adsorption air conditioning or cooling systems can be achieved.

The use of fine mesh sheets in adsorption is very common in the design and manufacture of cooling and air-conditioning systems that employ adsorption technology. The metal mesh is used as a barrier that keeps granular or fine powder adsorption material in place within adsorbent bed units. As the high performance materials used by these technologies are powders and have an average particle diameter of 37.7μm [55], the mesh sheets used in the designs of the adsorbent bed are also fine with very small effective pore diameters, approximately 100 to 30 micrometre diameter. The very small pore diameters paired with the low velocities of airflow (less than 2 m/s) within these adsorption beds means that the diameters of the metal wires within the mesh sheets have to also be very small, at the most about 25 to 50 microns wire diameter.

Several research studies have addressed the issue of fluid flow across woven metal mesh sheets or screens. Armour and Cannon (1968) have developed a widely used mathematical correlation between woven mesh sheet geometry and pressure drop. They concluded that pressure drop for laminar flow can be modeled by visualizing the mesh sheet as a collection of submerged spheres and for turbulent flow, using a bundle of tubes to model the mesh screen [56]. The research managed to predict pressure drop of nitrogen and helium flow across a variety of metal screen weave types including plain square, full twill, fourdrinier, plain dutch and twilled dutch weaves. However, using this method would prove difficult in designing a CFD setup if the mesh is needed in the design of an adsorbent bed within an adsorption cooling system that contains many various components of different mechanic and thermodynamic properties.

A porous medium approach was used by Teitel (2009) where insect-proof screens were simulated as porous media using calculated values of void fraction and permeability K using CFD analyses [59]. In the study, the permeability K of the porous slab was calculated using a correlation that related the permeability to the void fraction or porosity of meshes that was developed by Miguel *et al.* (1997) [58] and Miguel (1998) [57] which is:

$$K = 3.44\times10^{-9}\epsilon^{1.6} \qquad \text{(Eq. 1)}$$

where K is the permeability coefficient ($m^2$) and $\varepsilon$ is the porosity, also known as void fraction. However, using this method yielded erroneous values of pressure drops across meshes when using the equations for calculating K for input in CFD modeling. The CFD simulation containing the calculated permeability always resulted in values lower than those yielded by simulations of flow through a realistic woven screen. Teitel mentioned that the wide range of velocities tested by Miguel and also the large variety of screens with different weave types could have caused the anomaly [59].

Additionally, the nature of mesh screen sheets used in the design and manufacture of adsorbent beds being very fine, required to contain fine particles. The correlation of permeability and porosity developed by Miguel (1998) that was cited and used by Teitel in his porous method was concluded from a study to

determine airflow characteristics of greenhouse screening materials. Miguel et al. (1997) tested fourteen screens in a wind tunnel, mostly woven mesh made of metal or polyester and some are made of polyethylene strips held by thread. The width of the wires or strips vary from a range of 0.1 to 1.12 mm which can be considered too big to be compared to the meshes used in adsorbent bed applications which are 0.05 mm and smaller [58]. So the large wire diameters together with the erroneous results obtained by Teitel in his study suggests that another method needs to be used to obtain the value of permeability K to be used in adsorbent bed simulations other than by the correlation developed by Miguel (1998) from the mesh testings. The above studies were very dependent on the porosity of the mesh screens as a parameter for causing pressure loss, which may be inconsistent when the mesh diameter and effective pore opening decreases significantly. For example, for a mesh *x* and when the wire thickness and the opening width are both halved for mesh *y*, the porosity for both the meshes *x* and *y* stay the same as it is a ratio of free hole area divided by the total area. However, the pressure could be higher for the finer mesh *y* due to it having a higher surface area causing higher friction losses.

A recent study by Kouhikamali et al. (2014) investigated numerically the effects of geometry on the pressure drop and separation efficiency of wire mesh mist eliminators [60]. Among the variables tested were the wire diameter and the vapor velocity across the demister mesh. The results show that the separation efficiency and pressure drop increases as vapor velocity increases. The pressure drop was also found to be inversely related to the wire size caused by the increase of the wire surface area for smaller wire diameter. The study also conducted a comparison of using circular cross-section of the wire and square cross-sectional shape. It showed that the separation efficiency across the mesh screen is larger for the square cross section and the pressure drop of the demister is insensitive of the cross-sectional shape. Again for this study, the mesh wire diameters are from 0.1 to 0.3 mm, which is again too big. For a study of fine mesh, the geometry difference may cause an observable difference especially when a lot of wires are modeled so a round wire cross-section should be used due to it being more realistic.

Maddocks and Van Sciver (1988) studied the pressure drop of helium II flow through fine mesh screens of effective pore diameter about 5 microns where pressure drop across a mesh screen was measured experimentally when it is submerged in a vessel and subjected to a flow of liquid helium [62]. Results were then compared with predictions based on equations developed by Armour-Cannon. The helium II data showed significant deviation from the predicted Armour-Cannon values so the paper continued on to develop a more completed form of the friction factor based on the two-fluid model to accurately predict the pressure drop of He II flowing through fine mesh as liquid helium below 2.17 K behave differently in narrow passages and the mentioned temperature is involved in He II transfer devices that is of focus in the paper.

In a study by Zivkovic et al. (2012) a pressure drop correlation was developed for low Reynolds number Newtonian flows through a rectangular orifice in a micro channel using CFD methods, which can be said would be similar to the pore opening size of fine mesh sheets. The results and the consequently developed correlation indicated that the pressure drop is proportional to the average velocity through the orifice and depends on the orifice contraction ratio and the aspect ratio [61]. The research involved using COMSOL Multiphysics 3.5 to solve the Navier-Stokes equations for steady state, incompressible Newtonian fluid flow of very low velocity of 10 and 250 μm/s through the model domain. This method can be used and modified to find pressure drop across circular wire geometry instead of the rectangular passage and for higher velocities corresponding to airflow inside adsorber beds and values of permeability K can be derived to be used in the second stage of adsorber bed CFD modeling.

Additionally, it would have been too complex to simulate an actual three-dimensional CFD model that describes the flow through the mesh sheet, adsorbent material granule or powder and the adsorbent bed design altogether, due to the very high ratio between the characteristic scales of the fine mesh sheet and the adsorbent bed. A more stable CFD method that saves on computing power and makes errors more detectable is by simulating flow through the

screen first, then the adsorbent material granules or powder and using the results as input for a virtual model of the mesh sheet and adsorbent material incorporated in the simulations of flow within the adsorbent bed.

### *2.6 Summary*

Adsorption systems have the potential to provide cooling for air conditioning applications particularly in countries where solar energy is abundant. However, they suffer from low Coefficient of Performance (COP), being large and having high capital cost. New adsorbent materials such as Metal Organic Framework (MOF) materials are being developed possessing enhanced adsorption properties that are being used in development of high efficiency adsorption cooling systems in research and commercial fields. Typical adsorbent systems hold the powder or granular material in place using fine mesh. There have not been research done on CFD modeling involving whole adsorbent beds with complex geometries containing multiple components. The aim of this research paper is to study CFD modeling methods that can be used to simulate complex adsorption systems involving advanced materials, and shorten computational time using 'Porous Media Flow' physics.

# *Chapter 3* : Experimental test facility

The pressure drop characteristics of airflow through various metal mesh sheets and honeycomb section packed with adsorbent material representative of adsorbent beds were studied. In this chapter, a detailed description of the airflow test facility will be given. Section 3.1 describes the experimental test facility while section 3.2 describes the various mesh sheets used and their characterization. Section 3.3 describes the air flow and pressure drop measuring devices. Section 3.4 and 3.5 describe the honeycomb test section and its fitting with mesh and packing with adsorbent granules

## *3.1 Experimental set up*

The experiments were conducted using a pre-existing experimental rig of an air duct with a Perspex section as shown in Figures 3.1 and 3.2. The air duct has a fan at the outlet end to produce airflow that pulls air at atmospheric pressure from the inlet. Several tappings along the air duct were made (Figure 3.1) so that static pressure can be measured at several points across the air duct. The test pieces (mesh sheet or honeycomb section) were fitted between flanges and located at approximately 2 m downstream from the inlet. This upstream length of 2 m as well as a honeycomb flow straightener ensured uniform upstream air flow entering the Perspex test section.

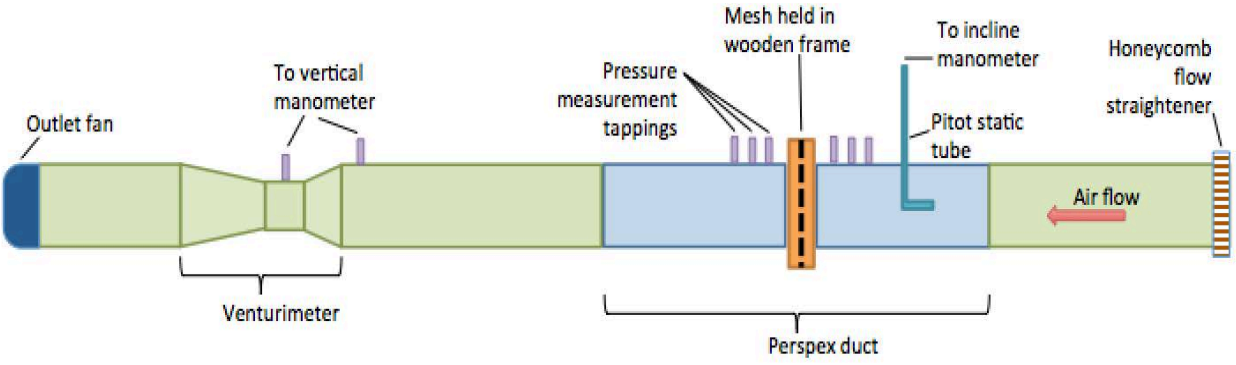


**Figure 3.1 Schematic of air duct used in experimental set-up**

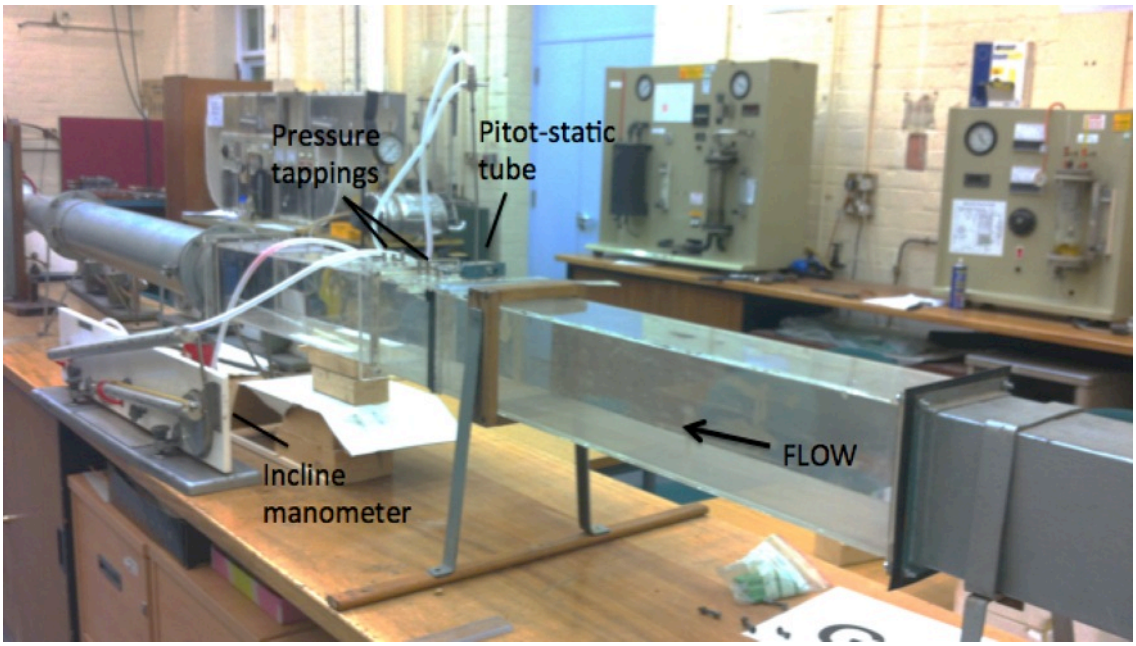


**Figure 3.2 Experimental set-up in lab**

### *3.2 Mesh sheet characteristion*

Four types of woven mesh sheets were used in the experiment which were selected from a range of mesh sizes that were suitable for containing adsorbent materials in fine powder form. The four meshes are supplied by Locker Wire Weavers Ltd and are of sizes 120, 150, 200 and 500 wires per inch.

The mesh test pieces were characterized to determine their wire and effective pore widths using a Leica light microscope (Leica Microsystems Ltd). The Leica microscope used was a material microscope for inspection of large materials as well as small dimensions. It has reflected light illumination using LEDs and is normally used to detect micro scratches on materials when the highest magnification is used. The microscope is connected to a computer and using imaging software, the width of the wires and openings can then be measured.

Figures 3.3 and 3.4 are micrographs of the mesh 120 wires per inch×0.09 mm and 500 wires per inch×0.25 mm taken by the Leica light microscope. The pictures are of the mesh sheets under one of the three magnifications: x50, x200 and x500 magnifications.

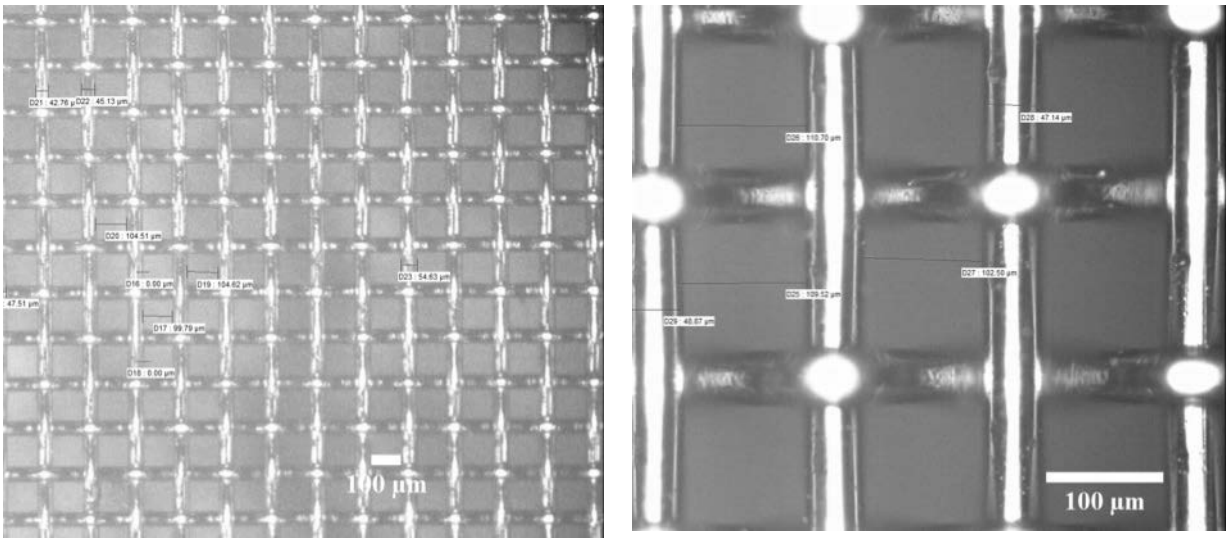


**Figure 3.3 Mesh 120 under x50 (left) and x200 (right) magnification**

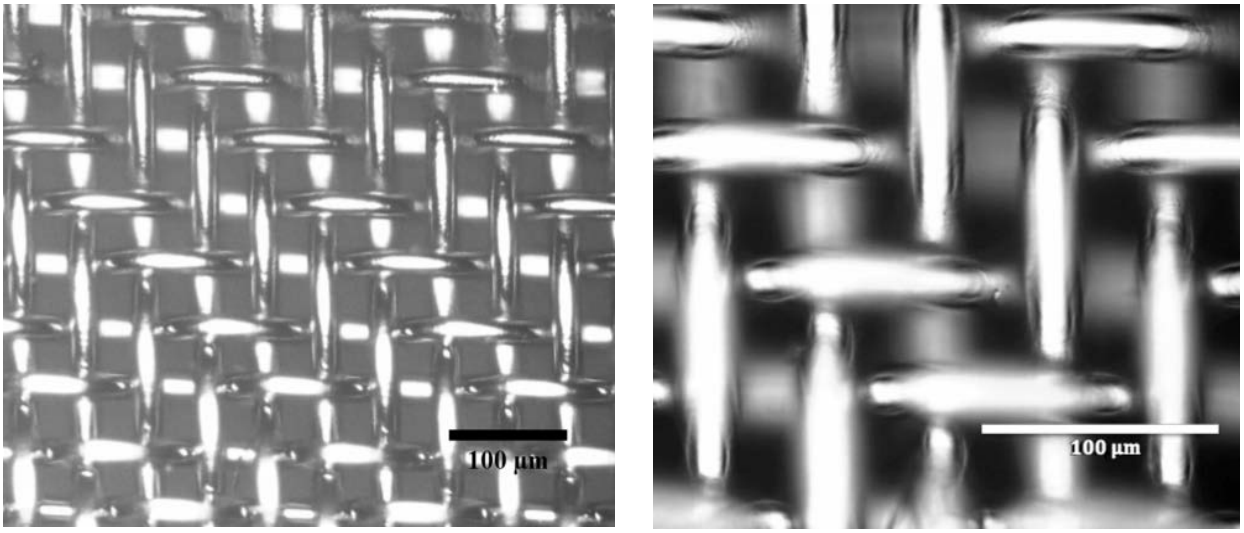


**Figure 3.4 Mesh 500 under x200 (left) and x500 (right) magnification**

The mean wire diameter and pore opening size were determined from ten measurements taken horizontally and ten taken vertically for wire diameter and opening width, for all four meshes. The opening widths were measured between the edge of one wire to the edge of the wire next and parallel to it. This will be the parameter that will decide if the mesh sheet can contain small particles or fine powder. Table 3.1 shows the mean wire diameter and mean opening size for the mesh sheets.

**Table 3.1 Mean values of wire diameter and opening for the four mesh layers**

| Mesh size (wires per inch) | Mean wire diameter (mm) | Mean opening size (mm) |
|---|---|---|
| 120 | 0.090 | 0.135 |
| 150 | 0.047 | 0.105 |
| 200 | 0.039 | 0.085 |
| 500 | 0.025 | 0.027 |

The mesh test pieces were fitted in the test rig between two wooden frames (Figure 3.5) that were held together by two pairs of nuts and bolts and were then mounted between the two Perspex sections of the air duct and screwed tightly into place. Masking tape was then put around the fitted wooden frame and mesh as well as the joining parts of the air duct as a precaution to make sure that there is no air leaking into the duct via gaps between the frames and Perspex duct sides that might affect the experiment results. The fitting and leak-proofing steps are repeated for all the experimental work.

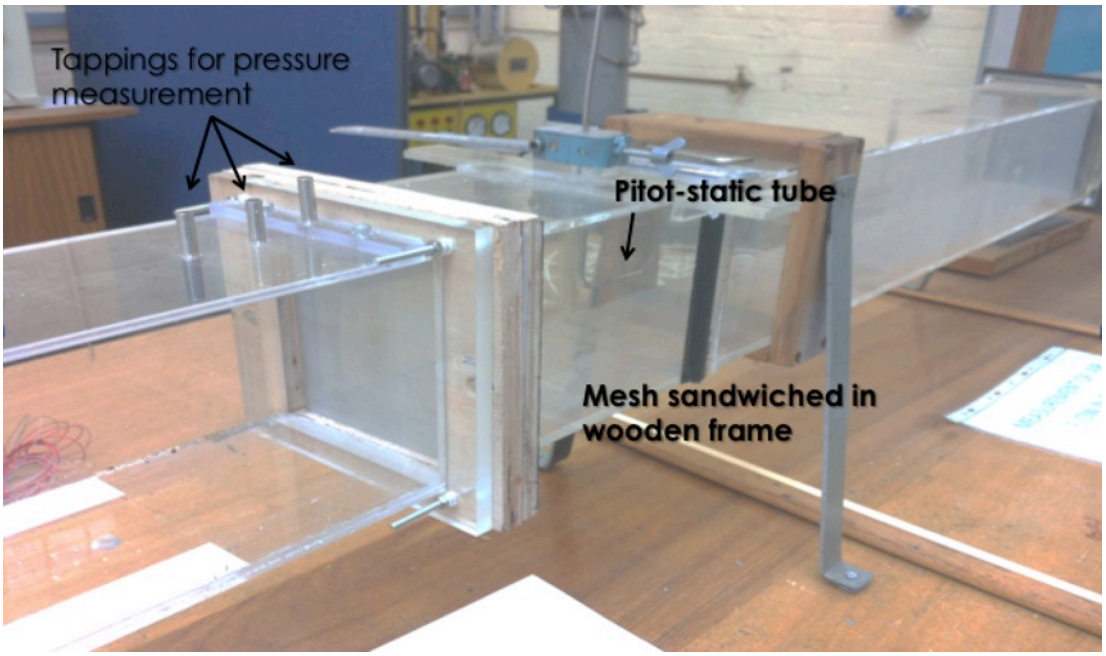


**Figure 3.5 Positions of mesh in frame and tappings for pressure measurement**

### *3.3 Air velocity and pressure drop measuring devices*

Figure 3.6 shows the different tapping points upstream (A, B and C) and downstream (X, Y and Z) where static pressure measurements were taken.

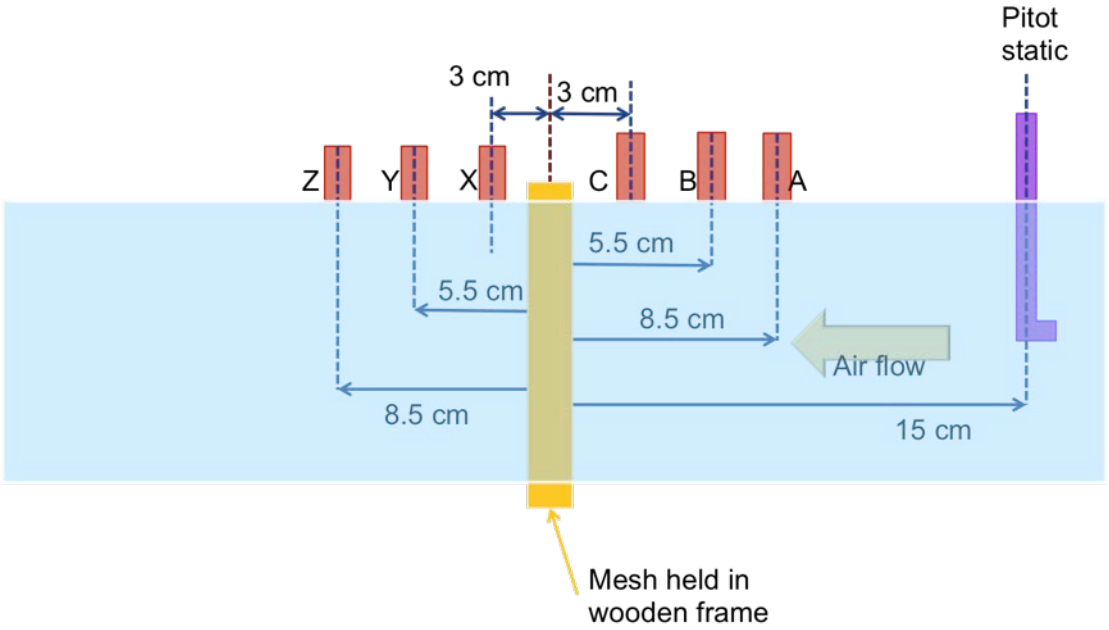


**Figure 3.6 Schematic showing the experimental set-up**

A pitot-static tube was connected to an inclined differential manometer containing alcohol manometer fluid, to measure the dynamic pressure 15 cm upstream of the mesh. From dynamic pressure readings, the upstream air velocity can be calculated, using Bernoulli's equation:

$$u = \sqrt{\frac{2}{\rho}(p_T - p_S)} \qquad \text{(Eq. 2)}$$

$$\rho = \frac{p_{atm}}{R_{(air)}.T_{atm}} \qquad \text{(Eq. 3)}$$

where u is the fluid velocity (m/s), $\rho$ is the density of fluid (kg/m$^3$) in this case for air, $p_{atm}$ is the absolute pressure (Pa), $T_{atm}$ is the absolute temperature (K) and $R_{(air)}$ is the specific gas constant which is 287 Jkg$^{-1}$K$^{-1}$ for air.

The Pitot-static tube (figure 3.7) used in the experiment is a single probe containing static pressure and total pressure transmitting ports at $p_S$ and $p_T$ respectively. The tube in the probe that faces the flow direction measures the total pressure in the duct at that point. The total pressure is the algebraic sum of

the static pressure and dynamic pressure. The static pressure can be determined when the dynamic pressure has no influence on the measurement, which is through small holes on the wall of the duct ($p_S$) positioned at right angles to the flow. Therefore the dynamic pressure also known as the velocity pressure can be calculated from the difference between total and static pressure as measured using a differential manometer.

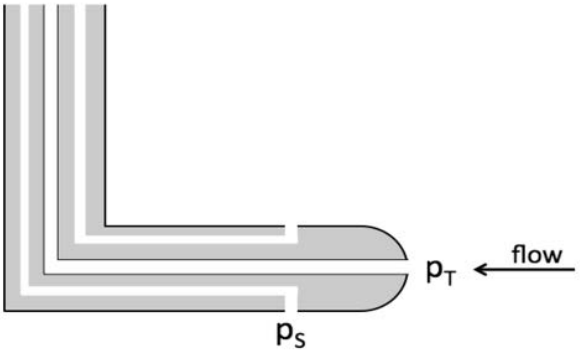


**Figure 3.7 Pitot-static tube**

The air velocity of the air duct was varied to find the corresponding static pressure values and pressure drop, to investigate the effect of velocity on pressure drop across the various test pieces. However, the experimental rig consists of a fan with fixed airflow, so the airflow velocity was varied by partially blocking the inlet gradually to obtain a range of velocities.

When the experiment was conducted, the maximum velocities upstream of the mesh sheet that was measured by the pitot-static tube gave different values for the four mesh types. When the inlet was fully open, the maximum velocity achieved upstream of the four mesh sheets were:

**Table 3.2 maximum velocity achievable in duct when four sizes of mesh sheets installed**

| Mesh size | Free hole area, β | Maximum upstream velocity (m/s) |
|---|---|---|
| 120x0.090 | 0.330 | 9.99 |
| 150x0.047 | 0.474 | 11.75 |
| 200x0.039 | 0.469 | 11.44 |
| 500x0.025 | 0.258 | 7.52 |

The pressure tappings A, B, C, X, Y and Z as well as the pitot static tube are connected to either an incline differential alcohol manometer or a differential pressure transducer. The inclined differential manometer has a range of 0-10 mbar and an accuracy of 0.2% of full scale, which is equivalent to 0-1000 Pa with an accuracy of ± 2 Pa. The pressure transducer used in the experiment is the OMEGA PX653-0.05BD5V which is high accuracy, low pressure laboratory transducer with bidirectional pressure measurement with range ± 0.05" water column (equivalent to ± 24.9 Pa) with and accuracy of 0.3% of full scale which means that the accuracy level is approximately ± 0.15 Pa.

Throughout the experimental study, dry air is used as the fluid medium because pressure drop in dry air flow is affected by fewer variables compared to moist air or steam. Therefore, dry air is more suitable for preliminary studies and simple analysis can be done as dry air introduces fewer inconsistencies. Due to time constraints, further analysis using moist air or steam was not conducted in this piece of research.

### *3.4 Set-up of honeycomb integrated with mesh*

This section involves the study of pressure drop across a certain thickness of packed adsorbent granules as part of a representative bed of adsorption air-conditioner. For this, a honeycomb of depth 10mm is sandwiched between two sheets of 150x0.047 mesh sheets that have 105 microns opening. The honeycomb integrated with mesh was tested first empty and then tested packed with 2mm granules of adsorbent material (metal aluminosilicate). The results were then compared to results of CFD studies for the same set-up.

The depth of the honeycomb adsorber bed is representative of the thickness of adsorber material used in the design of adsorption systems. As adsorber bed thickness increases, COP increases but SCP deteriorates [67]. 10 mm adsorber thickness was chosen as a compromise of the two properties, taking into consideration that if the adsorbent bed is too thick, mass flow would be

significantly obstructed. However, if the bed is too shallow, the performance will be too low due to the smaller amount of adsorbent.

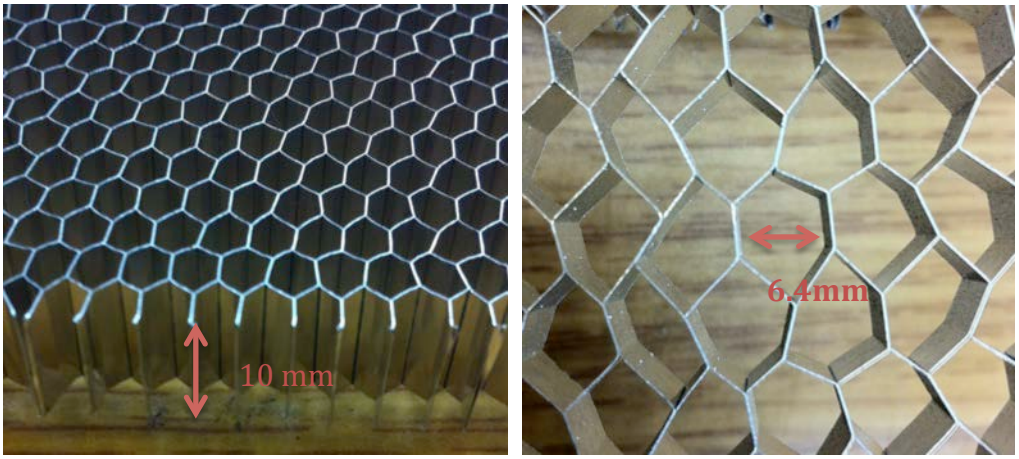


**Figure 3.8 structure of honeycomb showing thickness 10 mm and 6.4 mm cell size**

The hexagons of the honeycomb structure have an average width of 6.4mm as provided by the supplier and the thickness of the cell walls are 0.2mm as shown in figure 3.8. Figure 3.9 shows the honeycomb and mesh unit held in place by the wooden frame that was used in section 3.1. The opening of the wooden frame is 120x120 mm, and was made to match the internal width and height of the air duct used in the experiment.

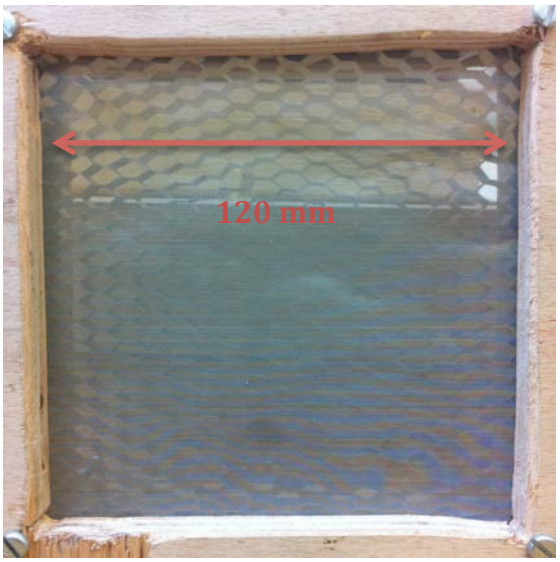


**Figure 3.9 internal width of wooden frame**

The honeycomb test section was fitted in the air flow duct used in testing the mesh sheets as described in section 3.2. The single sheet of mesh has been replaced by the honeycomb sandwiched between the mesh sheets. The distance of the tappings (3, 5.5 and 8.5 cm upstream and downstream) is taken from the sides of the honeycomb structure so now A, B and C are 3, 5.5 and 8.5 cm from the first mesh facing the air flow and X, Y and Z are 3, 5.5 and 8.5 cm from the second mesh, where flow exits the honeycomb structure as shown in figure 3.10. First, experiment with the honeycomb empty and not packed with granules was carried out. The airflow in the duct was varied at steps and the corresponding pressure readings for the 6 tappings (A, B, C, X, Y and Z) and the Pitot - static tube were recorded and the pressure drop for the particular velocity was determined.

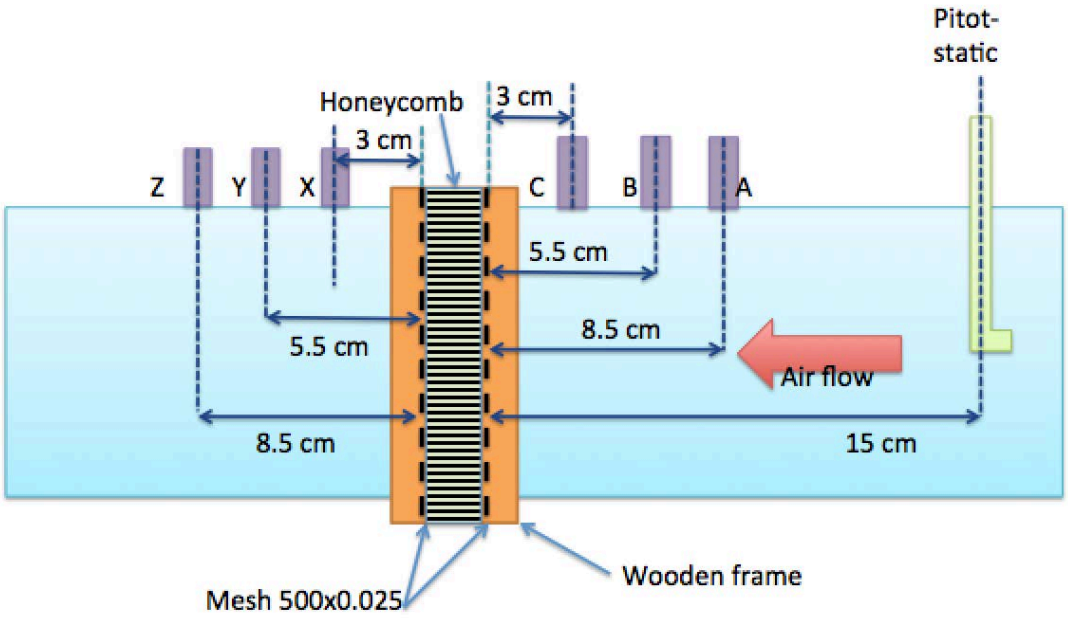


**Figure 3.10 Schematic of Perspex air duct with honeycomb and mesh assembly.**

### *3.5 Honeycomb filled with granules*

In this section, the experimental test facility of the honeycomb sandwiched between the two mesh sheets and the honeycomb packed with spherical granules of adsorbent material of diameters 1.6-2.4 mm is presented.

First the honeycomb sheet was fitted with one mesh sheet to form a base for holding the adsorbent material. The granules of the adsorbent materials was

then packed inside the cells of the honeycomb structure. A second mesh sheet was then stuck to the honeycomb structure packed with the adsorbent material. To ensure that the mesh sheet hold the granular adsorbent material inside the cells, they were glued to the edges of the honeycomb cells. Two different types of mesh sheets were used in the testing of the honeycomb structure filled with the adsorbent granules, namely mesh 150x0.047 (opening 105 microns) and mesh 500x0.025 (opening 27 microns). The honeycomb structure packed with adsorbent material granules and bound by two mesh sheets test section was fitted between two wooden frames and mounted in the air flow test facility as shown in figure 3.11

**Figure 3.11 Honeycomb with granules held in place by mesh**

Figure 3.12 shows the honeycomb test section packed with spherical granules of adsorbent material of diameters 1.6-2.4 mm. This adsorbent material was selected for testing as the granules have relatively large diameter which can be modelled and tested with relative ease and low computational time demand. Yet, it is representative of granular adsorbent material.

**Figure 3.12 Honeycomb with granules held in place by mesh (left) and granules (right)**

### *3.6 Summary*

An existing test facility were adapted to study the pressure drop characteristics of air flow through mesh sheets and a section of adsorber bed comprising of honeycomb structure packed with granular adsorbent material. Four mesh sheets with mesh size ranging from 120 to 500 wires per inch and two honeycomb structure fitted with two different mesh types were prepared for testing. The two honeycomb sections were tested both empty and packed with adsorbent material granules. The test facility was instrumented with Pitot-static tube to measure the air velocity before the test sections and pressure tappings to measure the static pressure downstream and upstream of the test pieces.

# *Chapter 4* Computational Fluid Dynamics (CFD) analyses

This chapter describes the modelling work done using Computational Fluid Dynamics (CFD) simulation of air flow through metal woven mesh sheets and a honeycomb containing adsorbent granules. Section 4.1 describes CFD simulations of air flow across single mesh sheets of various sizes. Section 4.2 is the CFD modelling for adsorbent material. Section 4.3 describes CFD simulations of a honeycomb structure integrated with mesh then section 4.4 decribes modelling of the honeycomb structure is packed with granular adsorbent material. Section 4.5 will summarise the findings and conclude the chapter

## *4.1 Two-dimensional Computational fluid dynamics modelling of air flow in mesh*

The CFD simulations were conducted using COMSOL Multiphysics package versions 4.3b and 4.4. The geometry was made using the dimensions of the experimental rig described in chapter 3. The simulations were conducted in 2D. The vertical height of the model geometry is 6cm with a symmetry set at the horizontal, due to the airduct internal width and height being 12 cm. The geometry (Figure 4.1) was halved and symmetry was used to simplify the model and shorten the computing time. The distance between the inlet and the mesh is 2m and between the mesh and the outlet is 0.5 m. The pressure value monitoring points were set to correspond to the locations of the tappings on the experimental air-duct.


**Figure 4.1 showing two-dimensional geometry set-up for CFD analysis of flow**

For a steady state study of velocity, *u*, the boundary conditions are described in Table 4.1.

**Table 4.1 showing boundary conditions and initial condition values for CFD model**

| Geometry | Boundary condition | Value |
|---|---|---|
| Inlet | Pressure, no viscous stress | $p_o$=0[Pa]<br>$p_{ref}$=1[atm] |
| | Reference velocity scale | $u_{ref}$=*u* [m/s] |
| Outlet | Velocity, normal outflow | $u_0$=*u*[m/s] |
| Wall | Wall function, no slip | |

The material for the entire domain is *air* which is available in the material library of the CFD package. The temperature of air for each case file is set to the temperature of air at the time when the experiment is conducted. For each of the varying velocity input values, a separate steady state study is conducted and one solution of pressure drop is obtained.

The physics module used in the studies are of turbulent incompressible flow. Turbulent flow module is chosen over laminar because airflow and pressure

simulations can be solved for higher values, as opposed to laminar where the solution does not converge for high values of velocity.

For a steady state study of velocity, *u*, the governing equations are:

$$\rho(u.\nabla)u = \nabla\left[-pl + (\mu + \mu_T)((\nabla u + (\nabla u)^T) - \frac{2}{3}\rho kl\right] + F \quad \text{(Eq. 4)}$$

$$\nabla.(\rho u) = 0 \quad \text{(Eq. 5)}$$

$$\rho(u.\nabla)\mathrm{k} = \nabla.\left[\left(\mu + \frac{\mu_T}{\sigma_k}\right)\nabla k\right] + P_k - \rho\epsilon \quad \text{(Eq. 6)}$$

$$\rho(u.\nabla)\epsilon = \nabla.\left[\left(\mu + \frac{\mu_T}{\sigma_\epsilon}\right)\nabla\epsilon\right] + C_{\epsilon 1}\frac{\epsilon}{k}P_k - C_{\epsilon 2}\rho\frac{\epsilon^2}{k}, \quad \epsilon = ep \quad \text{(Eq. 7)}$$

$$\mu_T = \rho C_\mu \frac{k^2}{\epsilon} \quad \text{(Eq. 8)}$$

$$P_k = \mu_T[\nabla u : (\nabla u + (\nabla u)^T)] \quad \text{(Eq. 9)}$$

(Inlet)

$$p = p_0, \left[(\mu + \mu_T)(\nabla u + (\nabla u)^T) - \frac{2}{3}\rho kl\right]n = 0 \quad \text{(Eq. 10)}$$

$$k = \frac{3}{2}(U_{ref} I_T)^2, \quad \epsilon = C_\mu^{3/4}\frac{k^{3/2}}{L_T} \quad \text{(Eq. 11, 12)}$$

(Outlet)

$$u = U_0 n \quad \text{(Eq. 13)}$$

$$\nabla k.n = 0, \quad \nabla\epsilon.n = 0 \quad \text{(Eq. 14)}$$

(Wall)

$$u.n = 0 \quad \text{(Eq. 15)}$$

$$\left[(\mu + \mu_T)((\nabla u + (\nabla u)^T) - \frac{2}{3}\rho kl\right]n = -\rho\frac{u_\tau}{\delta_w^+}u_{tang} \quad \text{(Eq. 16)}$$

$$u_{tang} = u - (u.n)n \quad \text{(Eq. 17)}$$

$$\nabla k.n = 0, \ \epsilon = \rho\frac{C_\mu k^2}{k_v \delta_w^+ \mu} \quad \text{(Eq. 18, 19)}$$

### *4.1.1 Mesh sensitivity*

A CFD analysis was conducted using geometries of meshes 200x0.04 and 500x0.025 to study the effect of mesh quality on the pressure loss values. The two geometries were simulated under conditions of air velocity of 5m/s to compare the pressure drop when using computational mesh 'Free Tetrahedral' of different mesh qualities. The five computational mesh qualities are listed in Table 4.2 as well as the minimum and maximum element sizes.

**Table 4.2 showing results of mesh sensitivity trials using CFD**

| Computational mesh quality | Minimum element size (mm) | Maximum element size (mm) | Pressure drop for 200x0.039 (Pa) | Pressure drop for 500x0.025 (Pa) |
|---|---|---|---|---|
| **Normal** | 0.12 | 2.7 | 392.37 | 843.18 |
| **Fine** | 0.06 | 2.1 | 387.29 | 776.22 |
| **Finer** | 0.024 | 1.68 | 349.47 | n/a (error) |
| **Extra Fine** | 0.009 | 0.78 | 349.60 | 948.05 |
| **Extremely Fine** | 0.0012 | 0.402 | n/a (error) | 945.87 |

From Table 4.2, it can be seen that using mesh of normal and fine quality gave values that were significantly different from the other mesh qualities used. For geometry 200x0.039, the values when using 'finer' and 'extra fine' mesh are only 0.2 Pa different. For geometry 500x0.025, the difference between values when using 'extremely fine' and 'extra fine' mesh is 2.18 Pa, the smallest difference compared to the other values.

Simulation of the geometries of mesh sheets 200x0.039 and 500x0.025 produced error during simulation using certain mesh qualities. At mesh quality 'extremely fine', the 200x0.039 geometry simulation returned with an error message concerning the divergence of the linear iterations and the returned solution is not converged. This error also occured when the geometry for 500x0.025 was simulated with a 'finer' mesh quality.

### *4.1.2 CFD results for pressure drop across the four mesh sheets*

CFD simulation was carried out for the four mesh pieces tested. All the simulations used mesh quality of 'extra fine' (Figure 4.2) that produced stable results.

As the modeling was in 2 dimensions, the mesh sheet was modeled as circular cross-sections lined up in a vertical array and spaced depending on the mesh sheet opening sizes (Figure 4.3). For all the mesh sizes tested, the diameter of the circles correspond to the wire diameter.

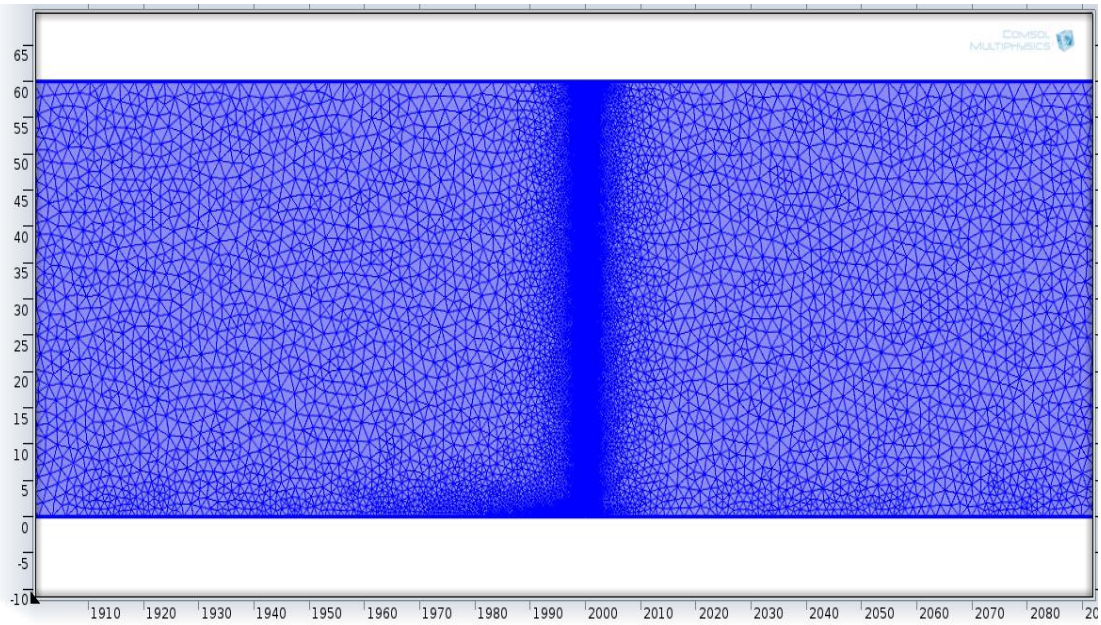


**Figure 4.2 computational mesh for CFD model of air duct, with mesh quality setting 'extra fine**

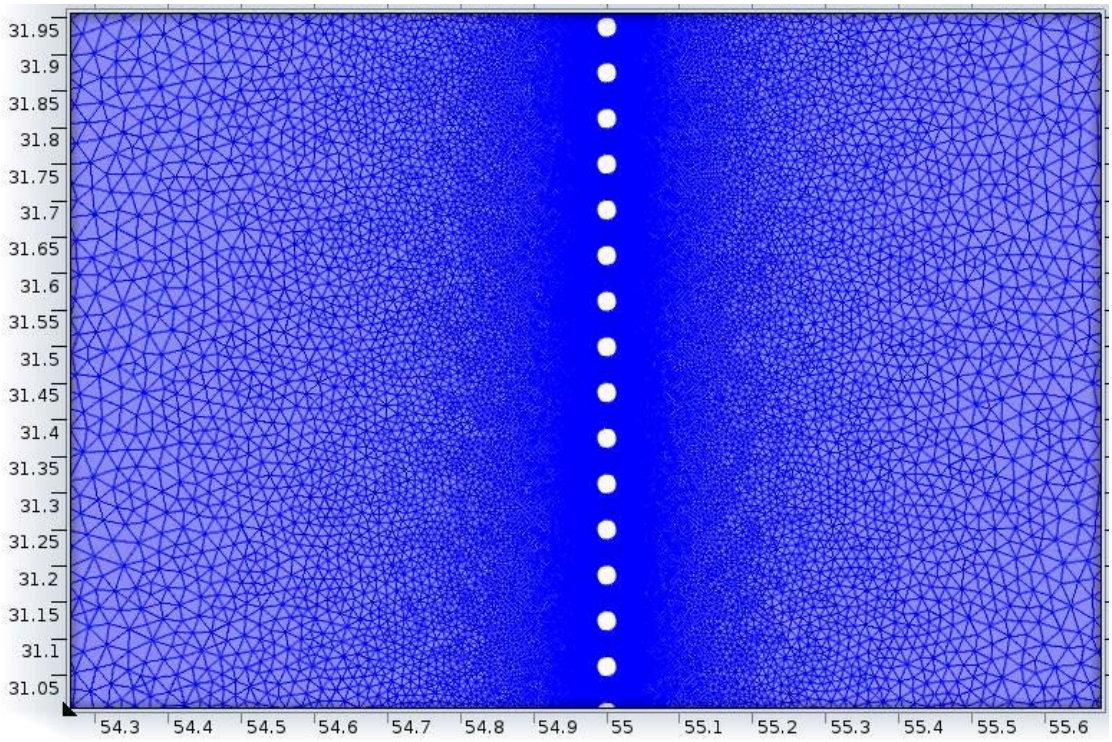


**Figure 4.3 CFD mesh showing circular cross section modeling of wires of the mesh sheet (mesh size 500x0.25)**

The pressure drop is affected by the following variables: air flow velocity and the geometric parameters of the mesh like effective pore diameter (opening size), the number of wires per inch and the wire diameter. These geometric parameters are related in a parameter $\beta$ known as the free hole area and can be calculated using a formula proposed by Ower and Pankhurst (1977) [66]:

$$\beta = \left(\frac{\frac{1}{n} - d}{1/n}\right)^2 = (1 - nd)^2 \qquad \text{(Equation 20)}$$

where $\beta$ is the free hole area with $n$ wires per unit length, and $d$ is wire diameter. $\beta$ is a function of the wire diameter and the wire density which means it also takes into account the effective pore diameter, and this free hole area $\beta$ is also known as the void fraction or porosity $\epsilon$, and is inversely related to the pressure drop. Table 4.3 shows the calculated $\beta$ values for the four meshes used in the CFD and experimental study.

**Table 4.3 showing the fours mesh sizes and calculated beta values**

| Mesh size | Opening size (mm) | Free hole area, β |
|---|---|---|
| 120x0.090 | 0.135 | 0.330 |
| 150x0.047 | 0.105 | 0.474 |
| 200x0.039 | 0.085 | 0.469 |
| 500x0.025 | 0.027 | 0.258 |

Figure 4.4 shows the variation of the CFD predicted pressure drop with velocity for the various mesh pieces modeled. It can be seen that for fixed velocity, the pressure drop increases with the decrease in the mesh free hole area parameter $\beta$. The highest pressure drop was caused by mesh 500x0.25 (opening 27 microns) which has the lowest $\beta$ value and the lowest pressure drop caused by the highest $\beta$ value. Figure 4.4 shows that the pressure drop gradient, that is the slope of the lines increases with the decrease in $\beta$ value.

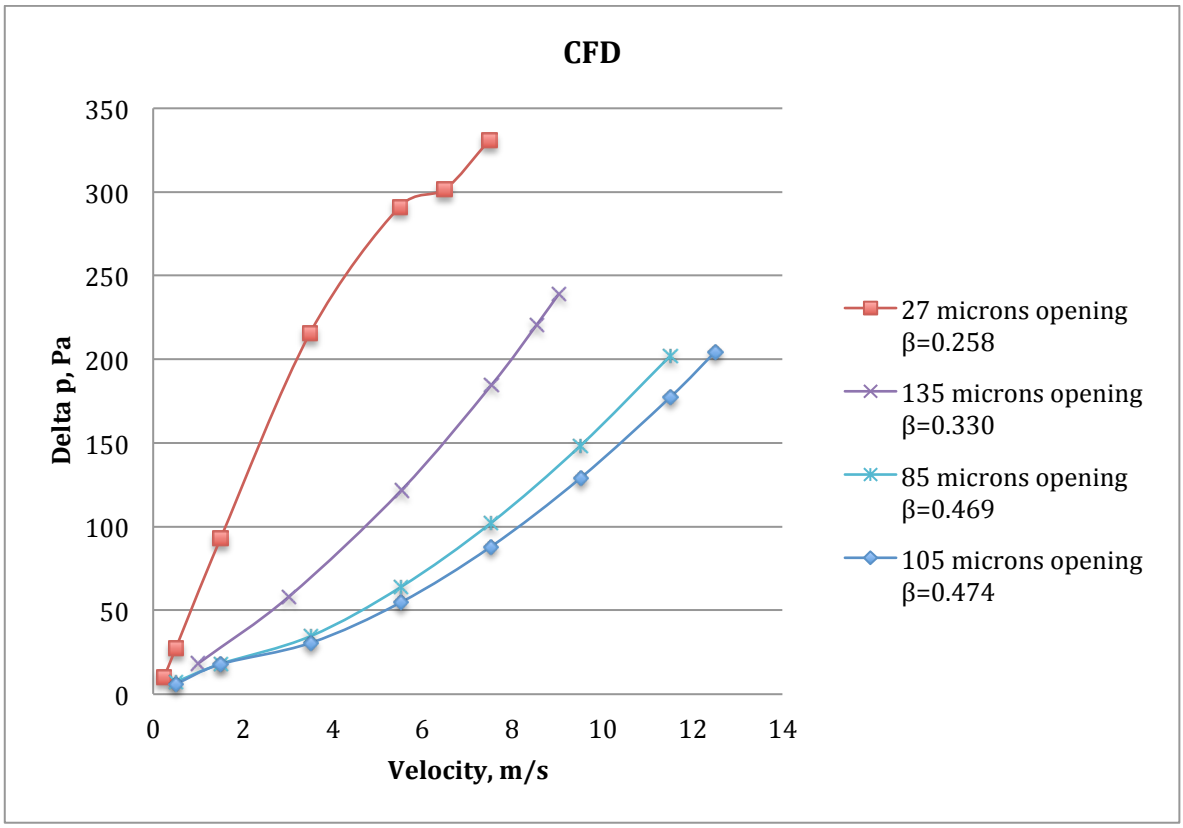


**Figure 4.4 Graph showing results of pressured drop from CFD simulation for the four mesh sizes**

### *4.1.3 Comparison of pressure profiles and characteristics of airflow across air duct through fine mesh sheet*

Figures 4.5 and 4.6 present pressure gradient lines on 2-dimensional air flow simulation for meshes 150 and 500 at a range of velocity. In Figures 4.5-4.8, air flow is from left to right and the air duct length is 2m upstream and 50 cm downstream. Each of the lines shows pressure difference of 0.01 Pa. The meshes 150x0.047 (opening 105 microns) and 500x0.25 (opening 27 microns) have been selected to be observed closely as they are the cases where the pressure drop gradients are lowest and highest. Figures 4.5 and 4.6 show a general trend of increased pressure with the increase in airflow velocity. This can be seen as the change in colour from blue (atmospheric pressure) to green, to yellow then orange and red, showing pressure higher than 1 atm. Also, as the velocity increases, with the pore size kept constant, there is higher pressure gradient, shown by the increase in the number of gradient lines across the duct, as velocity increases (Figure 4.6).

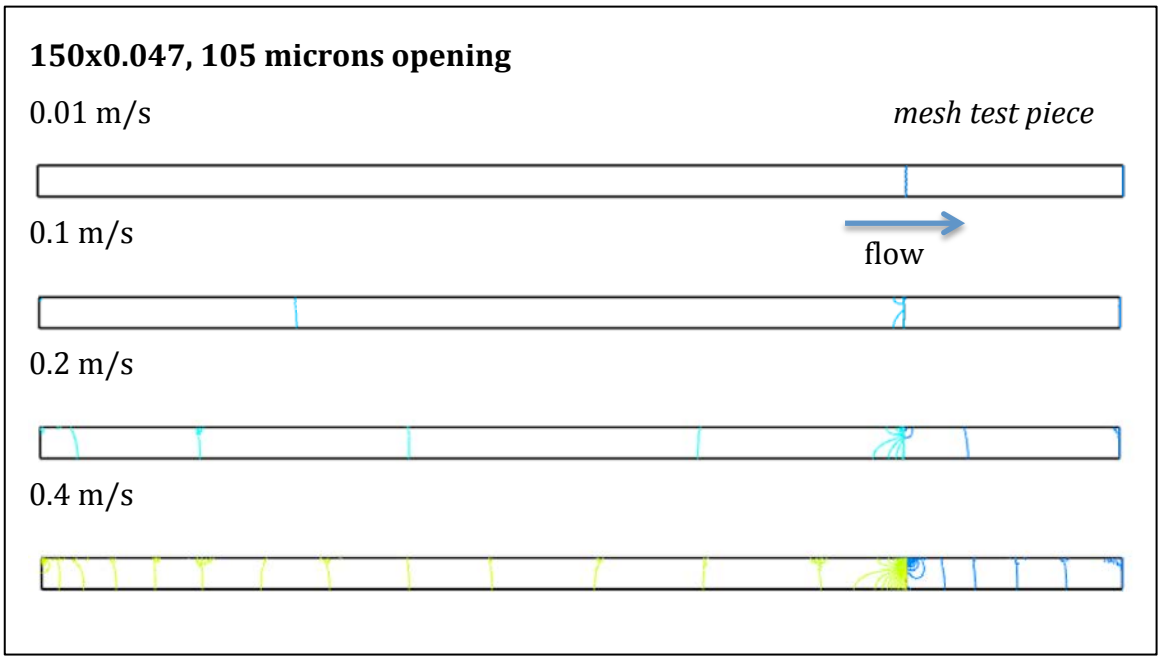


**Figure 4.5 Pressure gradients across air duct for 150x0.047 mesh**

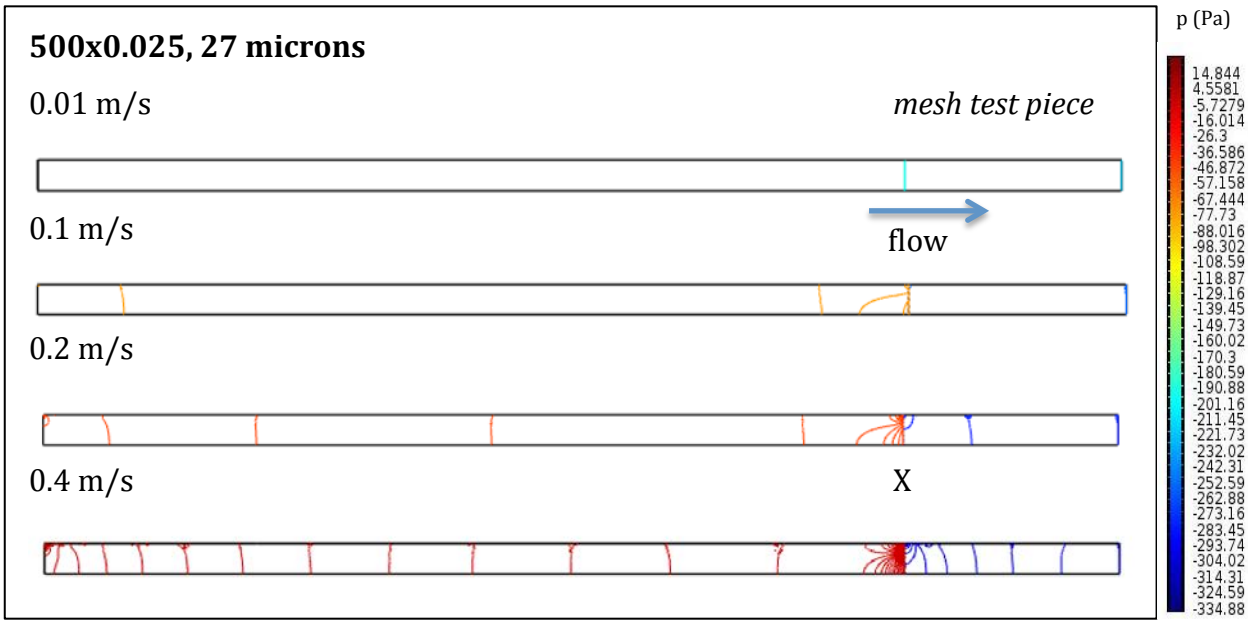


**Figure 4.6 Pressure gradients across air duct for 500x0.025 mesh**

In Figure 4.6, moving down the set, the trend in increase in number of lines is similar to that shown in Figure 4.5. This means that, if the velocity and length of the duct are kept constant, the pressure gradient and the way that the pressure varies upstream of the mesh are similar for the different pore sizes. X marks the region of most pressure change, containing a high density of pressure gradient lines, that occur immediately after the mesh test piece.

Even though the trend of the line spacing is similar between the meshes, it can be seen that the magnitude of pressure difference increases as the pore size gets smaller, the lines upstream get redder. Figure 4.7 is a comparison of the pressure magnitude for the four different mesh sizes simulated with flow velocity of 0.4 m/s.

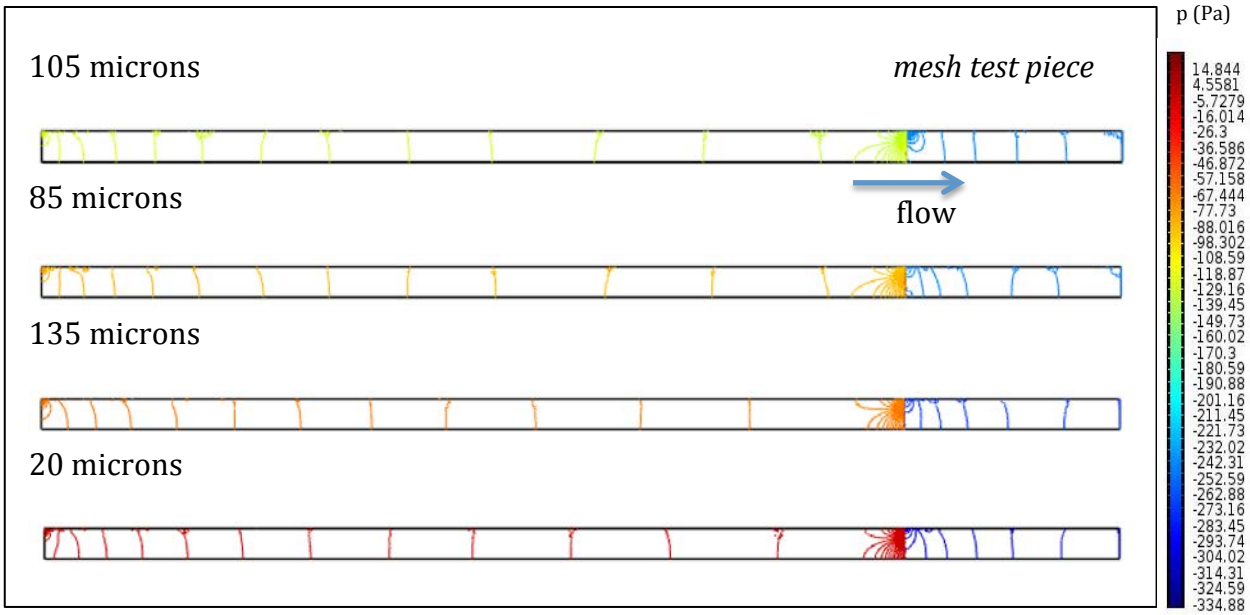


**Figure 4.7 Pressure gradients across air ducts comparing the four mesh sizes under 0.4 m/s flow**

It can be seen that for the 150x0.047, 105 microns opening mesh, the pressure rise at velocity of 0.4 m/s is small. However, as the pore size gets smaller, there can be seen more contrast in colour between upstream and downstream of the mesh.

This trend of increasing contrast (showing bigger difference in upstream and downstream pressures) is continued when the velocity is increased to 5 m/s for the four meshes. The different meshes were compared at a high velocity condition (5m/s), and the CFD pressure contours are shown in Figure 4.8, with gradient 0.01 Pa between lines. The airflow is from left to right.

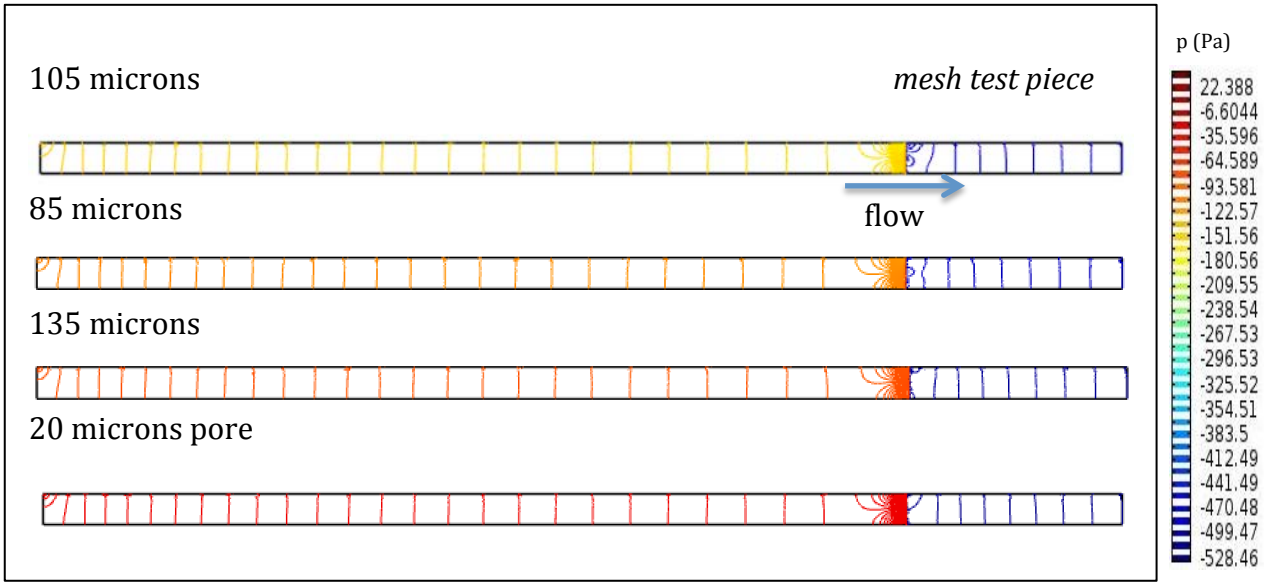


**Figure 4.8 Pressure gradients across air ducts comparing the four mesh sizes under 5 m/s**

The pressure gradient lines are closer together compared to 0.4 m/s velocity (laminar) showing more pressure change across the 2m upstream, even though the intervals are just 0.01 Pa, which can be considered very small. The region where the pressure contours are most dense is nearest to the mesh sheet location and it is where the majority of pressure drop can be said to occur at the mesh instead of throughout the air duct.

Figures 4.9-4.16 are from the CFD model for the smallest mesh opening (27 microns, size 500x0.025) at 7.5 m/s. Flow is from left to right.

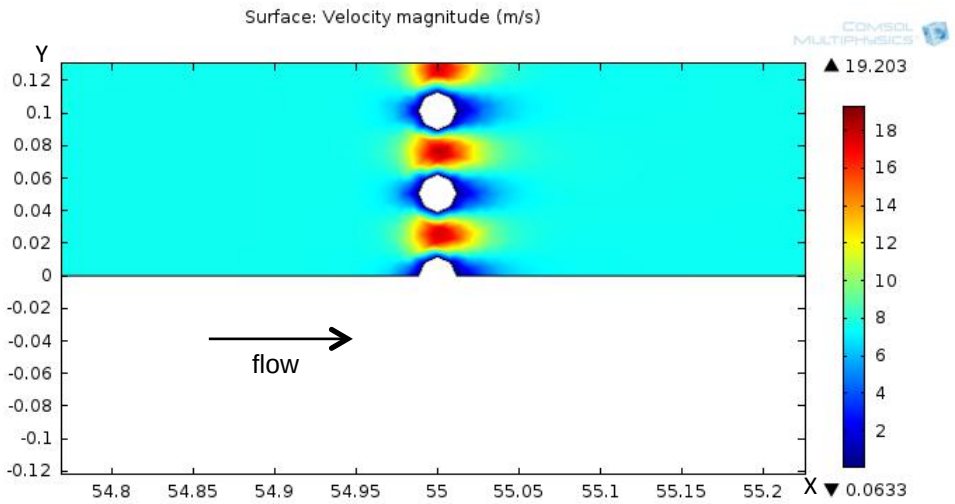


**Figure 4.9 velocity slice across CFD air duct at 7.5 m/s**

Velocity slice in Figure 4.9 shows region of highest velocity is in between wires and the lowest velocity is right before and after the wires (dark blue region). This can be explained by flow being concentrated in the narrow regions between the circular wire cross-sections as shown in the streamlines shown in Figure 4.10.

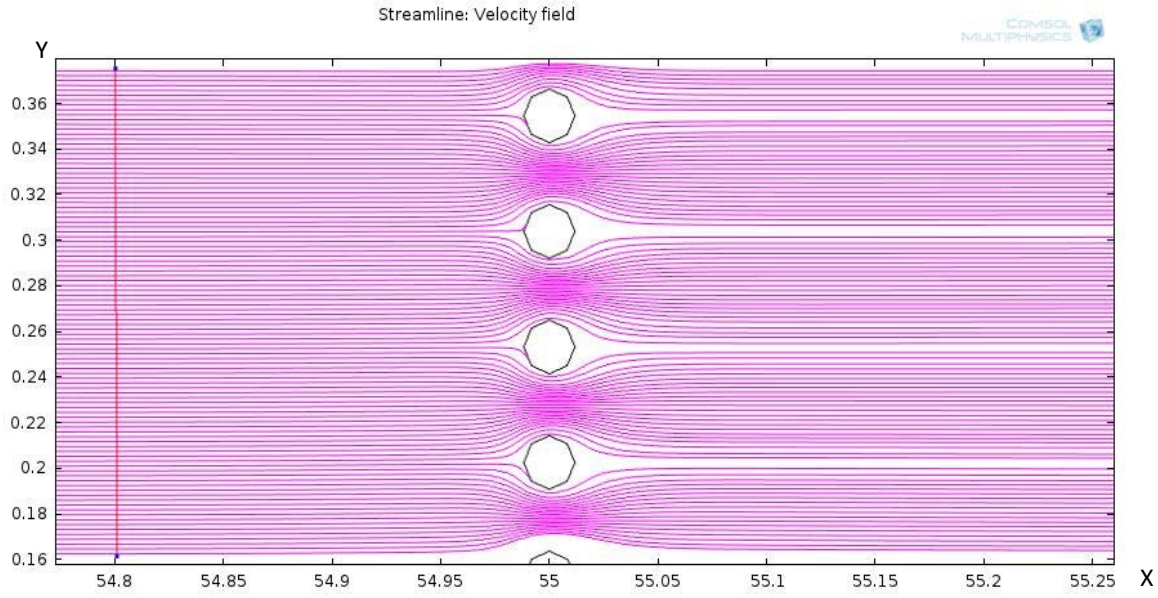


**Figure 4.10 streamlines across 500x0.025 at 7.5 m/s**

Pressure contours (Figure 4.11) show region of highest pressure before wires. Pressure changes the most across the wire within 1mm. There is a region of low pressure behind the wires (dark blue region)

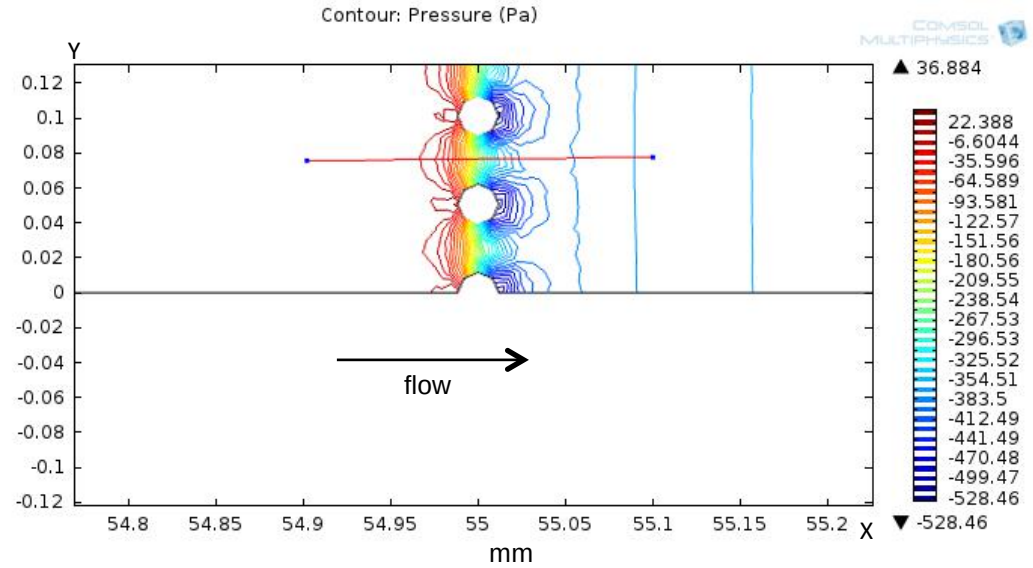


**Figure 4.11 zoomed in pressure contours with cut line in red between the mesh wires**

The velocity (Figure 4.12) and pressure (Figure 4.13) graphs are taken along the red line in figure 4.11 in between wires and the below graphs show values 1mm before and after the wire mesh location.

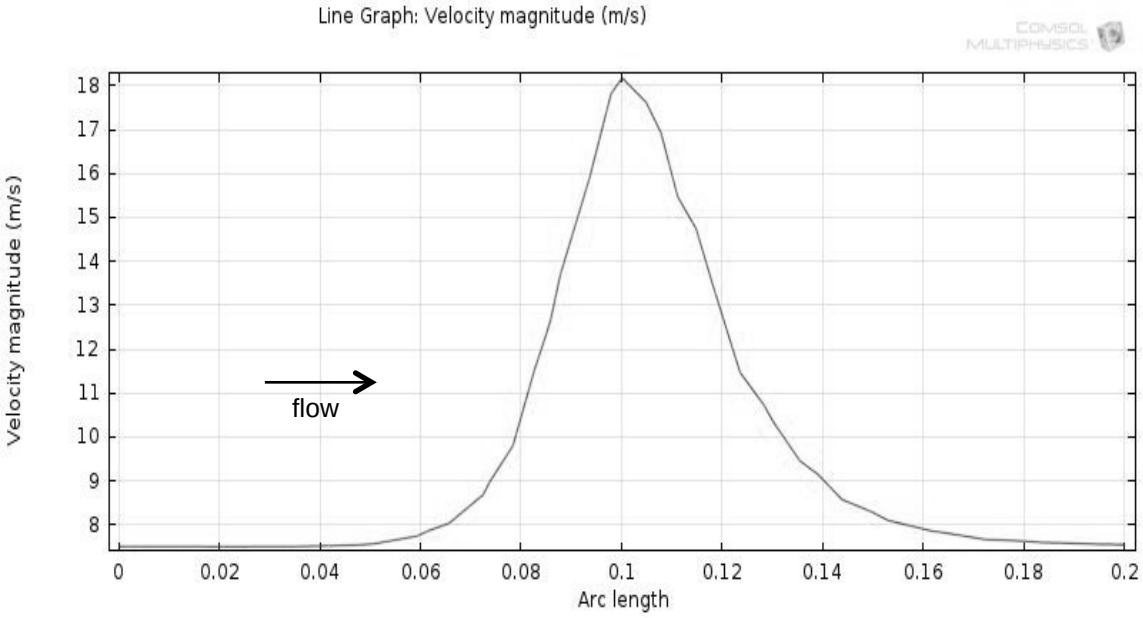


**Figure 4.12 velocity change characteristic between mesh wires**

The velocity reaches a peak of 18 m/s at the narrowest region between the wires. The velocity returns to the inlet velocity of 7.5 m/s when it is past the

wires and the upstream and downstream velocity is equal beyond 1mm either side of the wire mesh sheet. For the pressure drop, most of the pressure drop also occurs within a very narrow region 1mm before and after the mesh/circular wire cross-sections and beyond the mesh, the pressure stabilizes very quickly. The pressure drop reaches -400 Pa in this case.

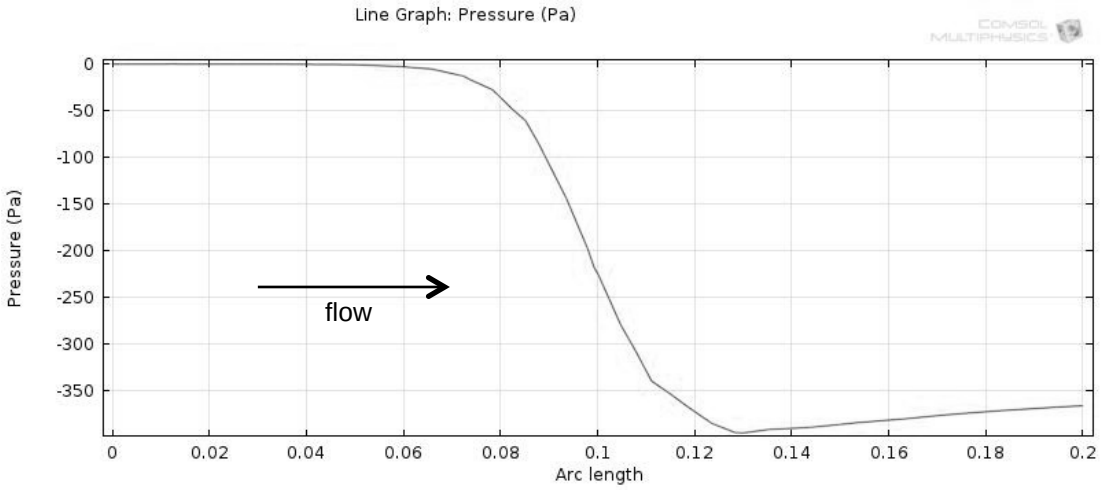


**Figure 4.13 pressure change characteristic between the mesh wires**

Contours shown in Figure 4.15 and 4.16 are for the line cut across the wire, which is the red line in Figure 4.14.

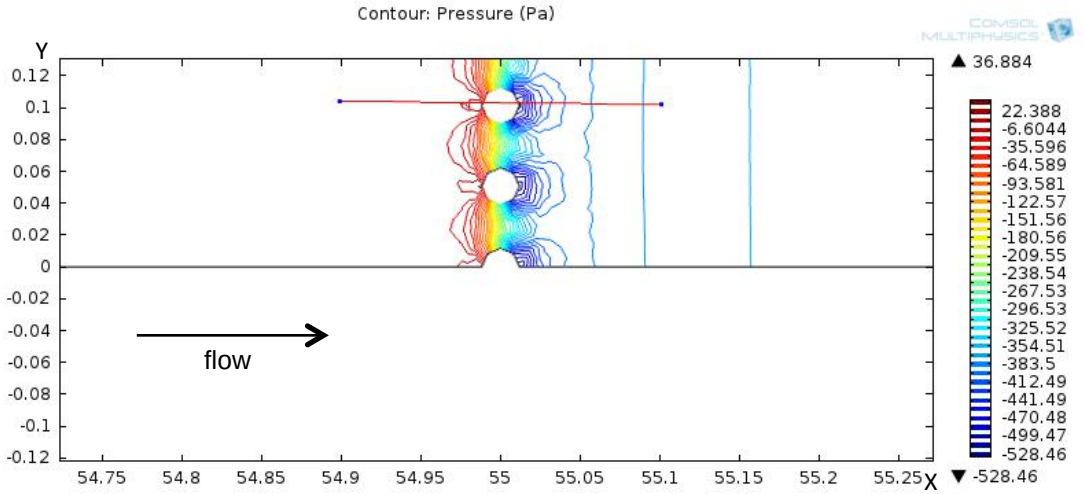


**Figure 4.14 Cut line in red going across one of the wires**

In Figure 4.15, instead of the velocity peaking when approaching the wire, the velocity dips to zero when getting nearer to the wire, which acts as an

obstruction to flow. However, downstream of the wire, the velocity recovers within a very short distance and returns back to 7.5 m/s.

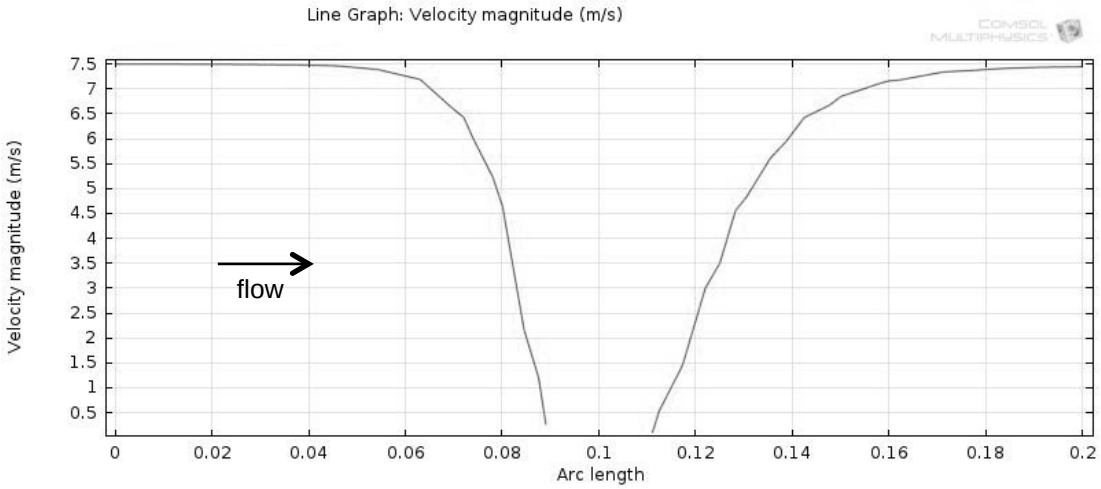


**Figure 4.15 velocity change along cut line going through wire**

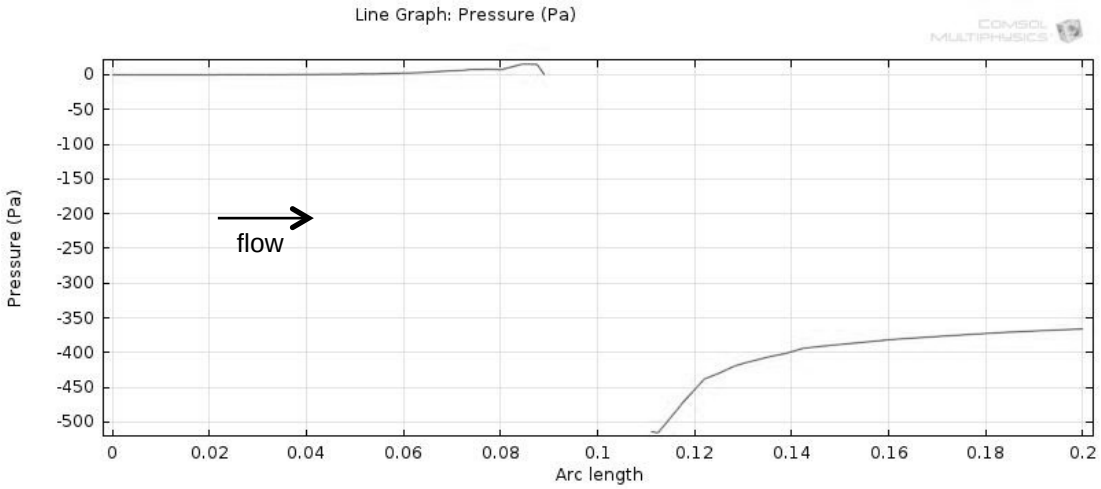


**Figure 4.16 pressure change along cut line going through wire**

The pressure graph (Figure 4.16) shows a very slight increase directly ahead of the wire obstruction. Right after the wire, there is a very low pressure region and this even reaches pressure of -500 Pa compared to the lowest pressure in between the wires which is -400 Pa.

### *4.2 Adsorbent material modelling*

This section describes the CFD parametric analyses as well as modeling of the adsorbent granules in CFD with cylindrical, spherical and capsular geometries. This step in modeling is the first stage of CFD simulation of honeycomb structure integrated with mesh sheets, filled with adsorbent material and empty. Three-dimensional simulation was carried out to enable investigating the flow in representative cross-section of a new adsorbent bed structure shown in figure 4.17. Due to the complexity of the overall geometry and in order to reduce the computational time, the simulation was carried out in stages. First, the modeling of adsorbent granules was carried out and described in section 4.2. Second, the modeling of honeycomb cells integrated with mesh pieces was carried out as explained in section 4.3. Third, the honeycomb cells integrated with the mesh and filled with the adsorbent granules was simulated and described in section 4.4. Section 4.5 provides a summary of the main outcomes of this CFD simulation work.

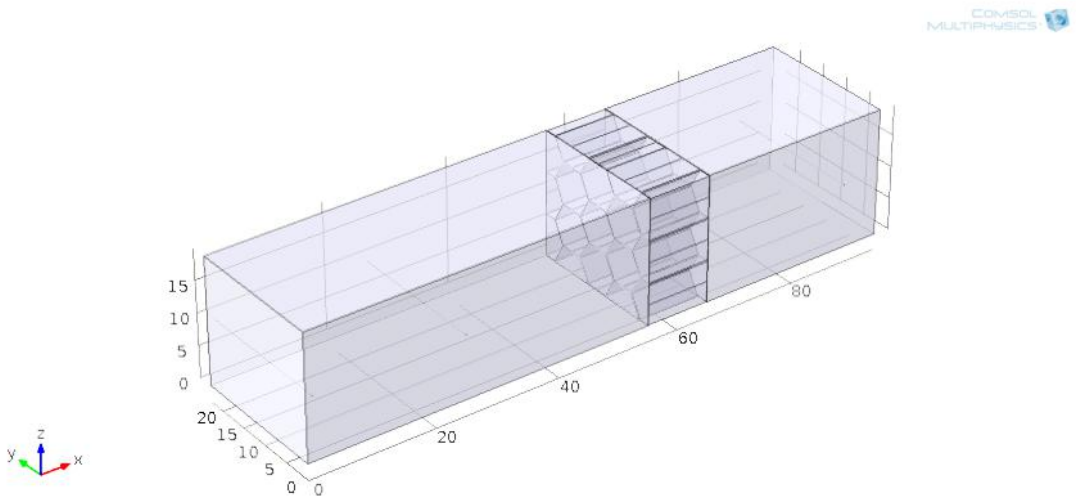


**Figure 4.17 CFD model geometry of representative bed.**

The flow in porous medium can be modelled using the physics module “Free and Porous Media Flow” available in the COMSOL package. This model uses Darcy’s Law to model flows in porous media using user-defined values of permeability and porosity of a certain material. Permeability is a value that measures the

degree of ability of a porous material to allow fluids to pass through. From Darcy's Law, permeability can be calculated using the formula

$$u = \frac{K}{\mu}\frac{\Delta p}{\Delta x} \quad \text{(Eq. 21)}$$

$$K = \mu . u \frac{\Delta x}{\Delta p} \quad \text{(Eq. 22)}$$

Where $K$ is the permeability coefficient ($m^2$), $u$ is air flow velocity ($m/s$), $\Delta p$ is pressure drop or difference (Pa), $\Delta x$ is the flow length or thickness of test sample (m) and $\mu$ is the fluid viscosity (Pa.s), which in this case is for air at viscosity of 0.0000181 Pa.s. The $\beta$ value and permeability parameter can be obtained from either experimental testing or from detailed computational modeling.

In this section, detailed CFD simulation was used to determine the $\beta$ value and permeability values for adsorbent material packed in hexagonal honeycomb cells.

### *4.2.1 CFD modeling of porous media in hexagonal cells*

Figure 4.18 shows the geometry setup of a single hexagonal cross-section duct to simulate air flow through hexagonal honeycomb cells filled with adsorbent granules. The granules were simulated as cylindrically and spherically shaped particles as shown in figure 4.19. Figure 4.20 shows a cross-section of the test cell where the size of the hexagon and the number of the granules packed were varied. The granules were modelled as cylinders with 1mm diameter and 1mm length.

The cylindrical and spherical geometry arrangement does not necessarily replicate the actual random packing arrangement. However, geometry showing true to form random packing arrangement would require a high amount of computing power and time to produce and solve for pressure drop in CFD softwares.

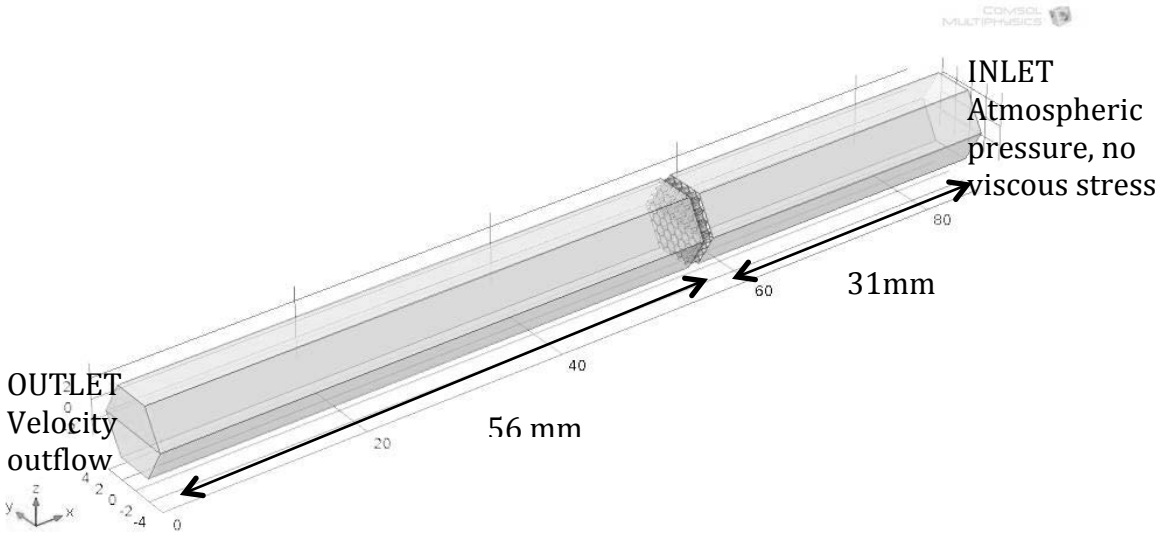


**Figure 4.18 Geometry of air duct for hexagon section**

The inlet and outlet in the model has the boundary conditions set like the previous two-dimensional CFD simulations of the mesh sheets carried out in section 4.1. The inlet was set as 'Pressure, no viscous stress' with inlet pressure=$p_o + p_{ref}$, $p_o = 0$ and $p_{ref} = 1$ atmosphere. The outlet was set as 'normal velocity outflow' and for one steady state study, one value of velocity, *u,* is set. The velocity and pressure from the CFD solutions are taken at 30mm upstream of the obstruction and 30mm and 55mm downstream of the obstruction as a surface.

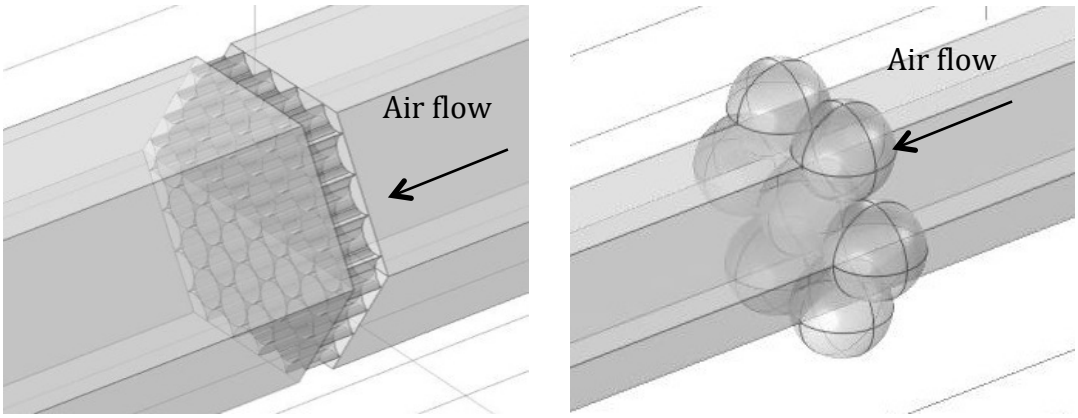


**Figure 4.19 CFD geometry showing granules simulated as cylinders (left) and spheres (right) in hexagonal arrangement**

The boundary conditions at the sides of the hexagons is set as symmetry on all 6 sides of the three geometries shown in figure 4.20 as the cell represent one of too

many cells in the adsorber bed. Different outflow velocities namely $u$=0.05, 0.1, 0.5, 1.0, 1.5, 3.5, 5.5 m/s were used in the simulation of the geometries.

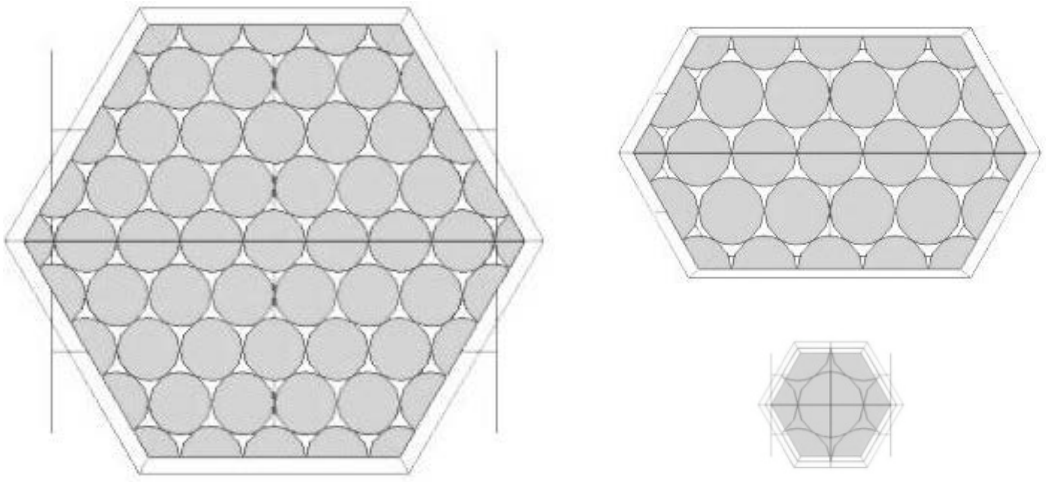

**Figure 4.20 Various sizes of hexagon cells: Large hexagon (left), medium hexagon (top right) and small hexagon (bottom right)**

The physics module used in the simulations is incompressible flow. For a steady state study at a velocity $u$ (set at outlet), the governing equations are the same as the ones used in incompressible flow for the previous CFD analyses of single mesh sheets, which are equations 4-19.

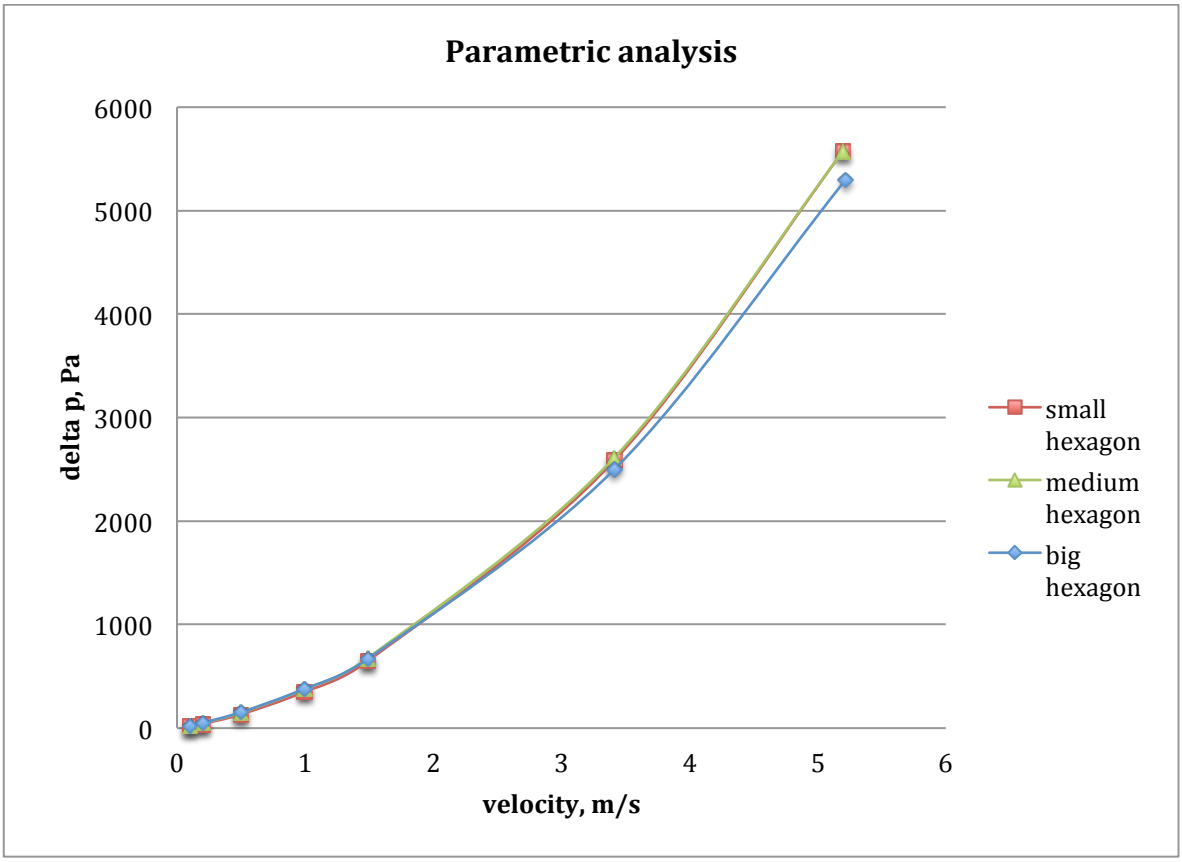


**Figure 4.21 pressure drop vs. velocity obtained from parametric analysis**

Figure 4.21 compares the pressure drop versus velocity of the three geometries. It can be concluded that the small, medium and big hexagon configurations gave very similar pressure drop against velocity graphs. Therefore it can be concluded that using the small cell configuration will produce accurate pressure drop values.

To investigate the effect of particle shape and length, Figures 4.22-4.25 shows the geometry setup of cylindrical particles with 1mm and 5 mm lengths, one row of spherical particles with 1 mm diameter and 5 rows of spherical particles with 1 mm diameters.

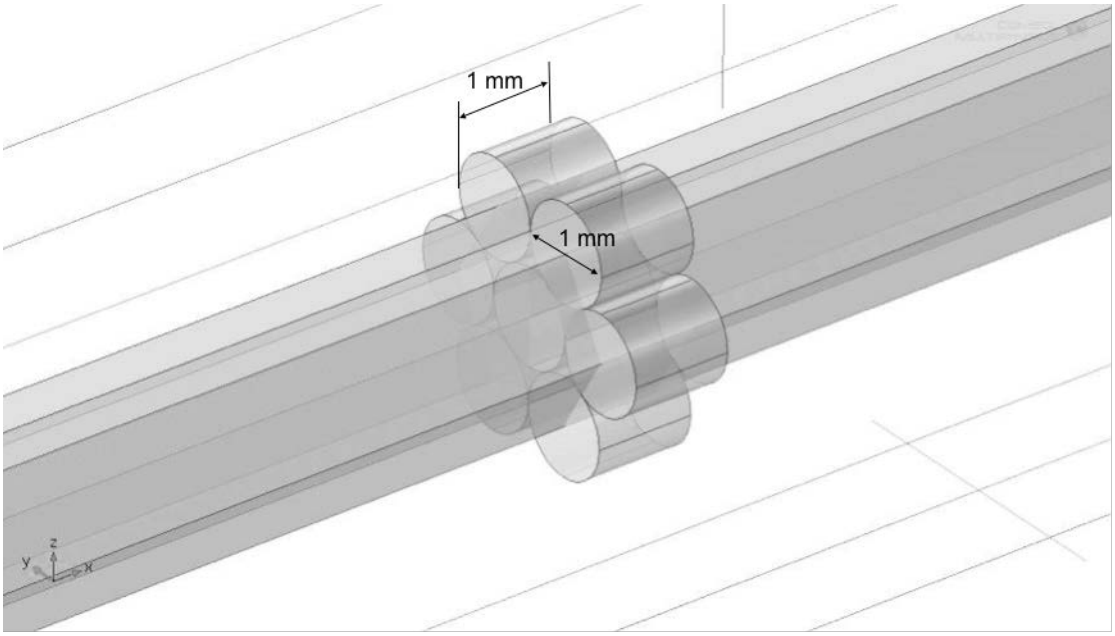


**Figure 4.22 Geometry for flow across cylinders of thickness 1mm**

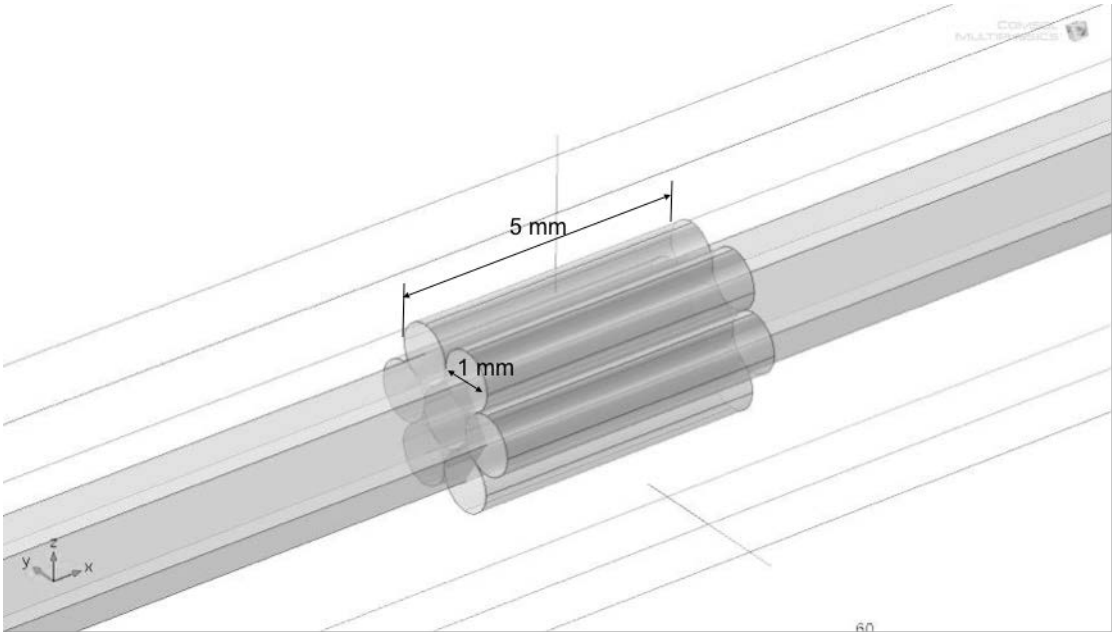


**Figure 4.23 Geometry for flow across cylinders of thickness 5mm**

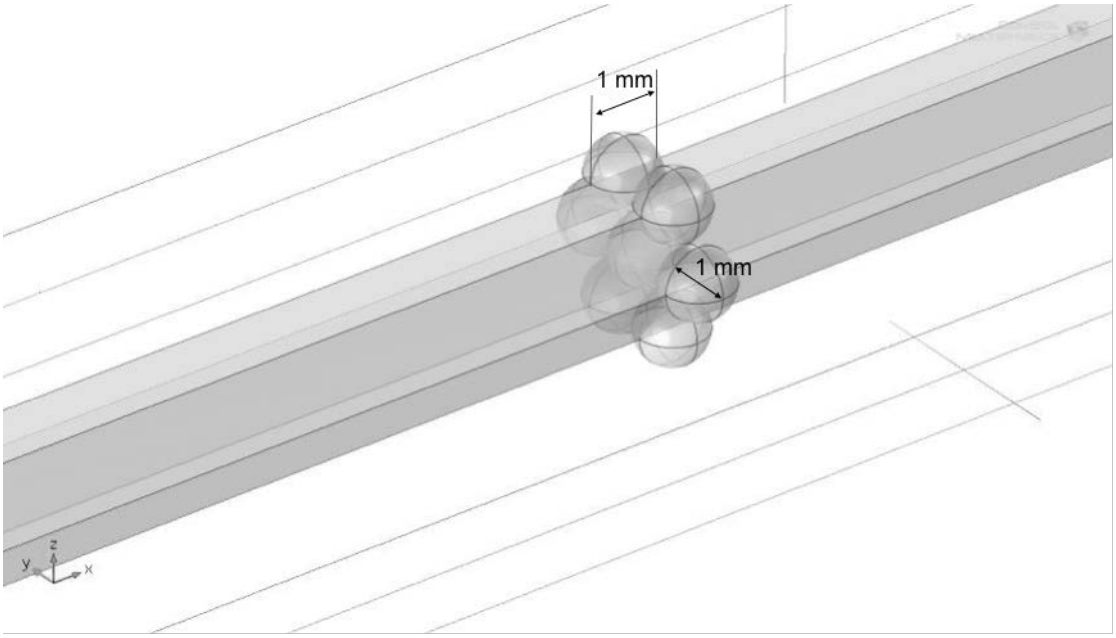


**Figure 4.24 Geometry for flow across one layer of arranged spheres**

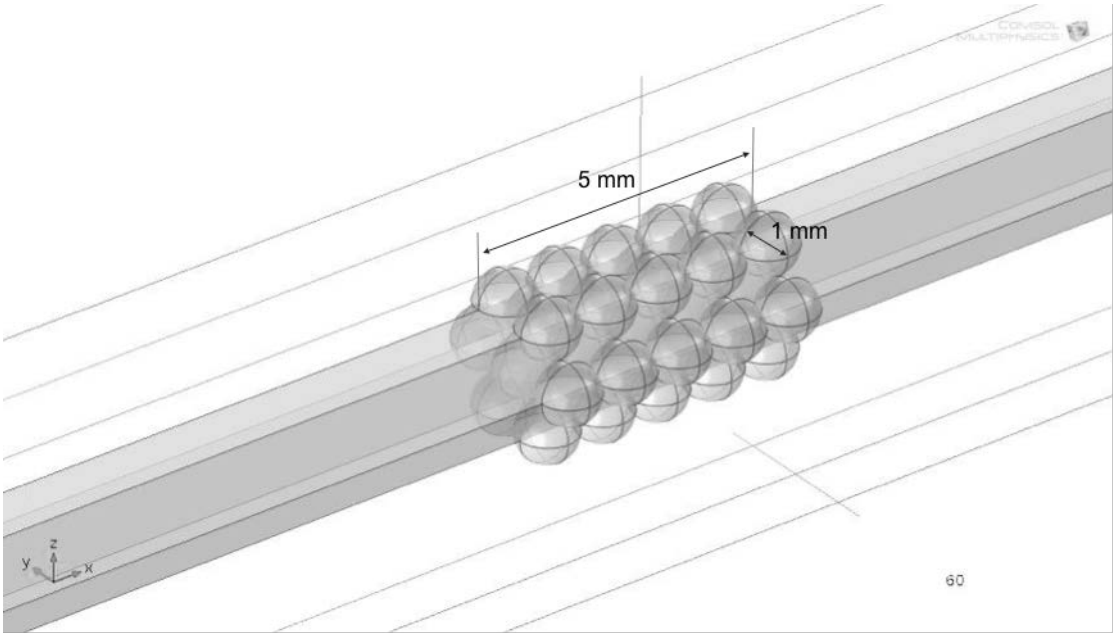


**Figure 4.25 Geometry for flow across five layers of arranged spheres**

Figure 4.26 compares the CFD-predicted pressure drop for the four cases modelled. It was observed that the 1 row of 1 mm spherical granules gave significantly lower pressure drop with velocity compared to the 1 mm long cylindrical structures. This might be due to the sharp edges on the ends of the cylinders as well as the circular face of the cylinder being perpendicular to the air flow thus causing high resistance to air flow. As the thickness increases pressure losses due to friction increased for both geometries. However the difference between the cylindrical and spherical granules was reduced as shown specifically in the low velocity region depicted in figure 4.27.

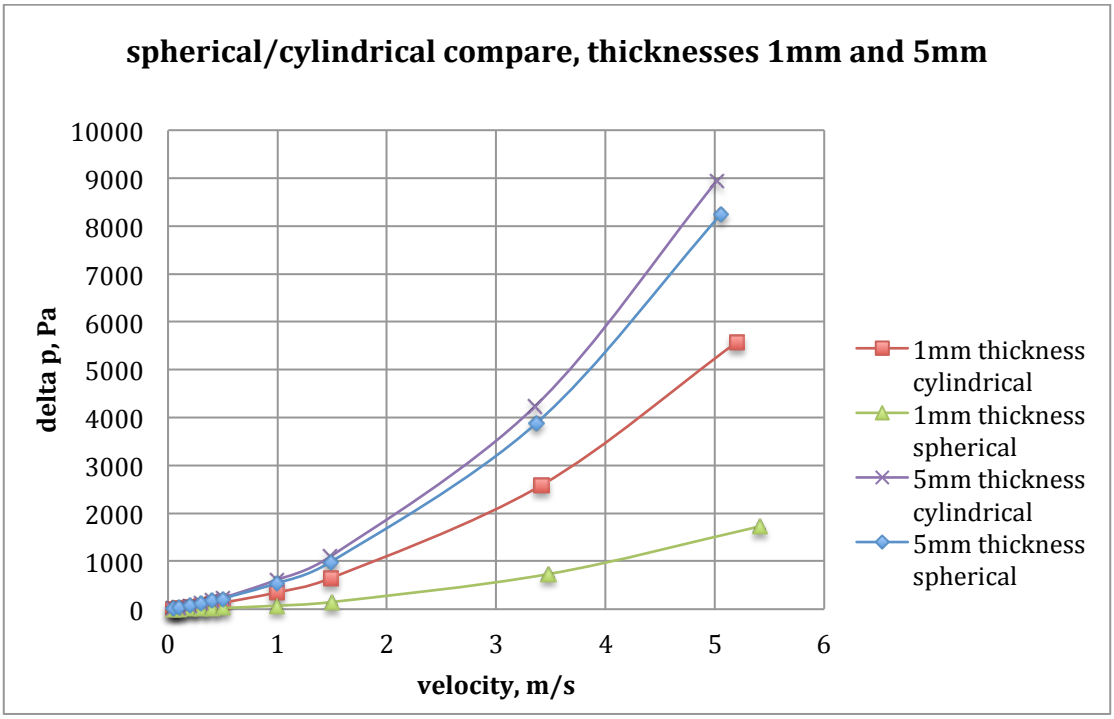


**Figure 4.26 pressure drop vs. velocity graphs for cylindrical and spherical geometry**

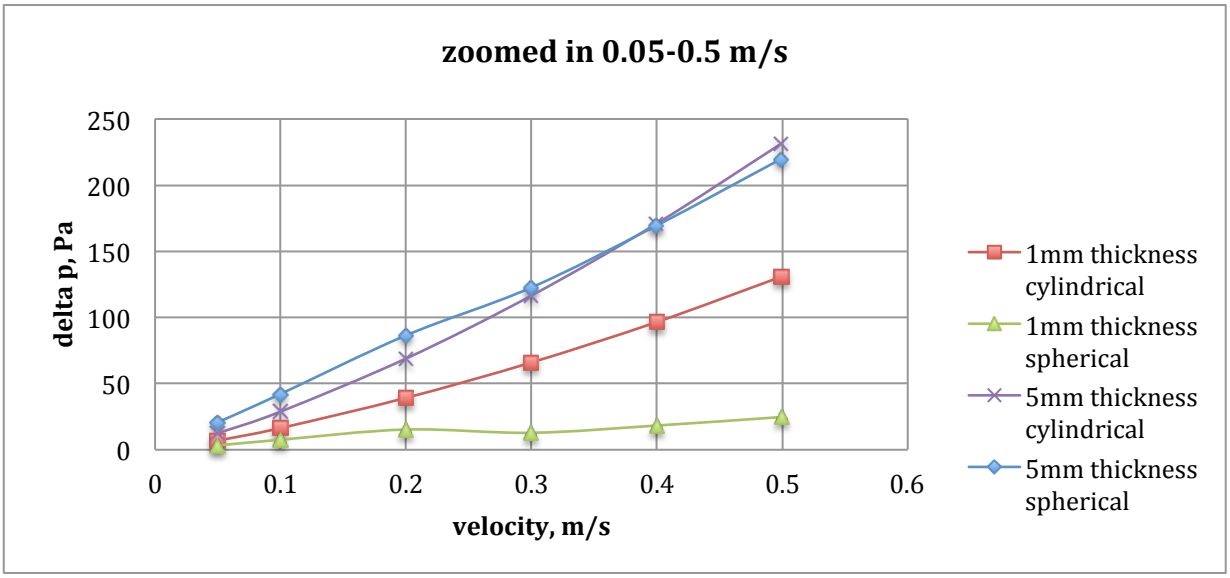


**Figure 4.27 pressure drop simulation results at low velocities for spherical and cylindrical geometries**

Figure 4.28 shows the velocity contour for airflow velocity of 0.5 m/s. It can be seen that the highest velocity occurs in the narrow regions between the spheres and the downstream velocity returns to the upstream velocity almost immediately after passing by the spherical obstructions.

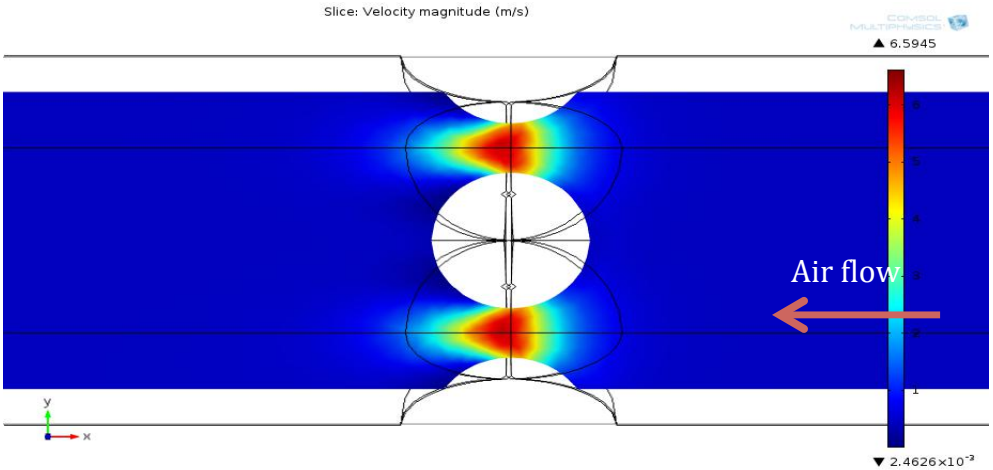


**Figure 4.28 velocity slice across granules model as a sphere**

Figures 4.29 and 4.30 show the streamlines for 1 layer and 5 layers of spheres, indicating that at 0.5 m/s the airflow remains laminar. As the velocity increases from 1.5 m/s, the flow becomes increasingly turbulent, and from 3.5 m/s the size of the wake caused by the spherical particles increase

| 0.5 m/s | 1.5 m/s |
|---|---|
| 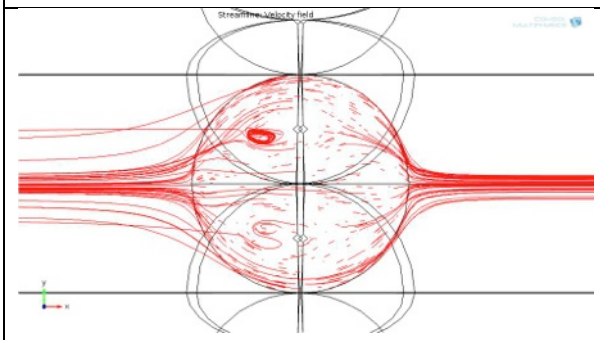 | 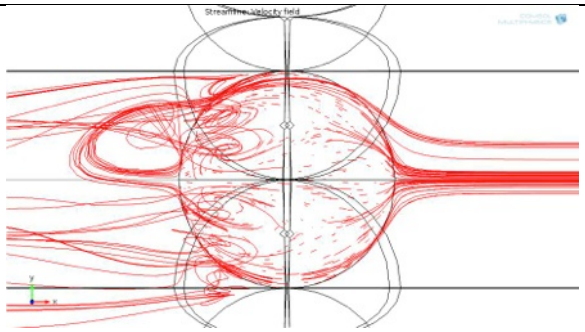 |
| 3.5 m/s | 5.5 m/s |
| 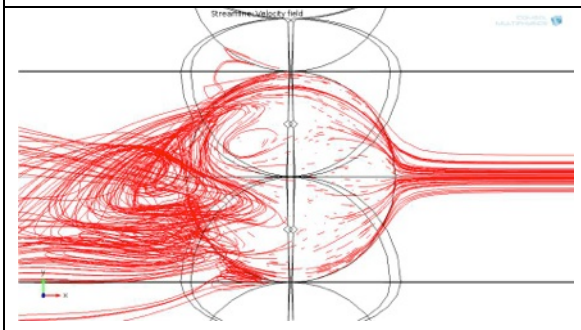 | 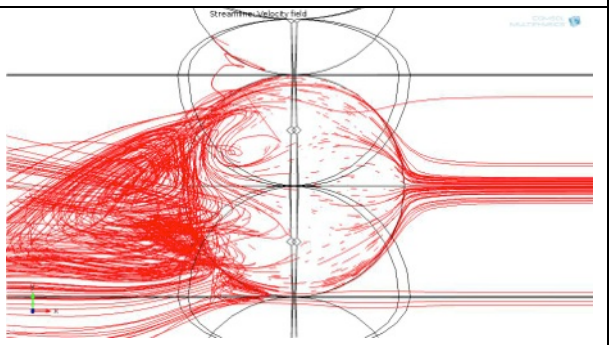 |

**Figure 4.29 streamlines at increasing velocity around one sphere**

| Velocity (m/s) | Stream lines |
|---|---|
| 0.5 | 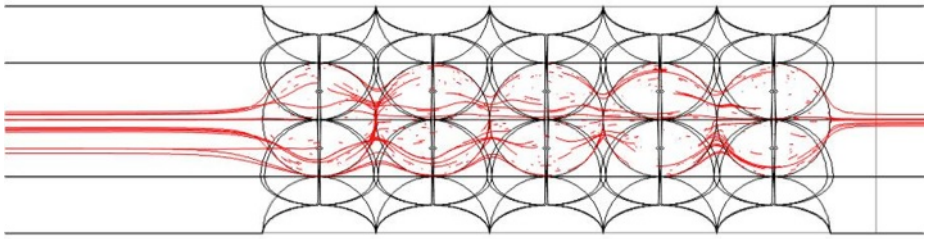 |
| 1.5 | 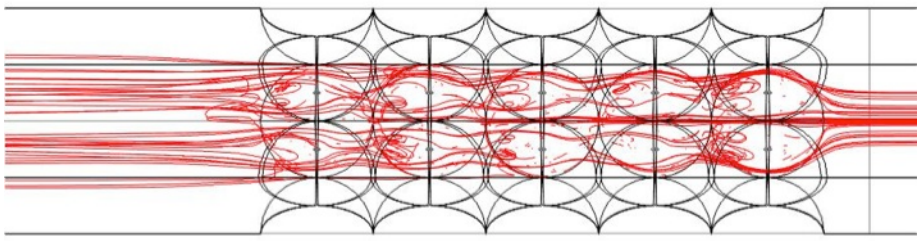 |
| 3.5 | 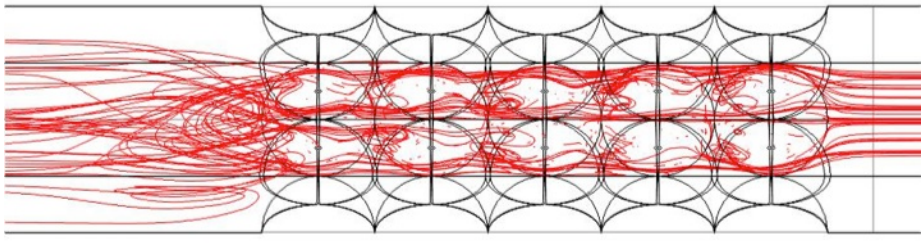 |

**Figure 4.30 streamlines at increasing velocity through 5 sphere**

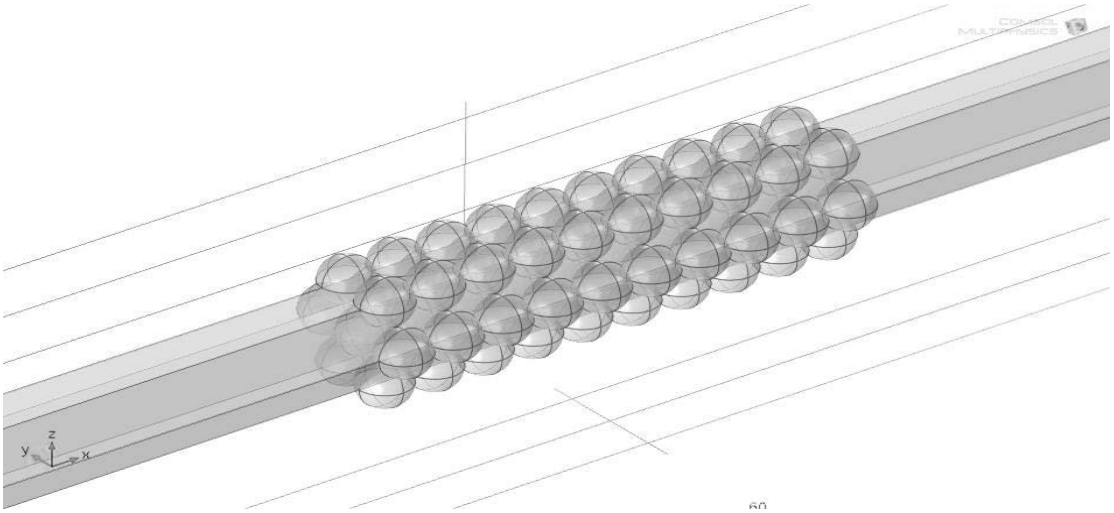

**Figure 4.31 10mm thickness spherical, d=1mm**

The predicted pressure drop values shown in figures 4.26 and 4.27 were used to determine the permeability values for the various cases simulated, along with the case of 10 rows of spherical granules shown in figure 4.31, using Darcy's Law (Equations 21 and 22). As the velocity in adsorption beds is low, only data for velocity below 2 m/s were used in deriving the permeability values as shown in table 3.4 and figure 4.32.

Figure 4.32 shows the permeability of 1 row, 5 rows and 10 rows of spherical particles, and the 5 mm long cylindrical particles while table 4.4 lists the permeability values for the 5 and 10 rows of spherical particles. Figure 4.32 shows that the permeability K value of the 5 rows and 10 rows of spherical particles are in agreement and ranges from $1.00\times10^{-11}$ at low velocity to $8.5\times10^{-12}$ at high velocity.

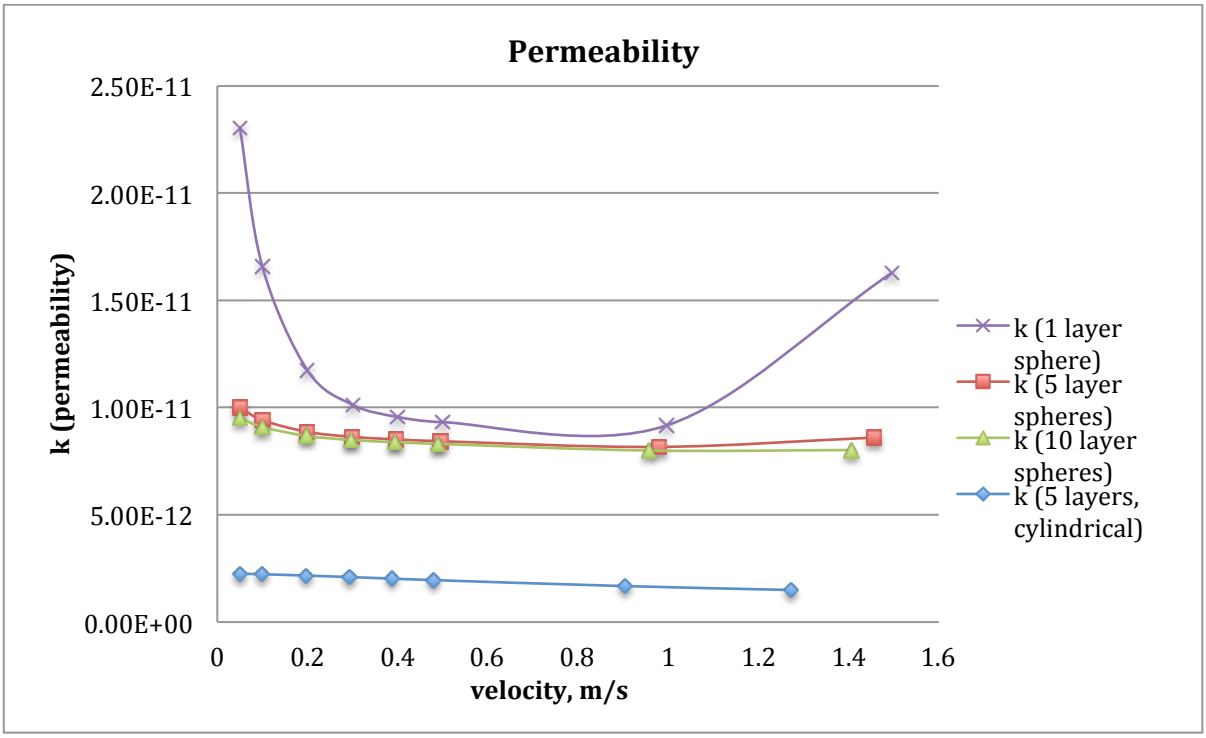


**Figure 4.32 permeability values across 0-1.5 m/s for varied thickness of spheres**

**Table 4.4 showing variation of K values for 5 and 10 spheres**

| u | K (5 layer spheres) | | u | K (10 layer spheres) |
|---|---|---|---|---|
| 0.0499 | 1.001 E-11 | | 0.0499 | 9.520 E-12 |
| 0.0998 | 9.414 E-12 | | 0.0996 | 9.093 E-12 |
| 0.1991 | 8.865 E-12 | | 0.1983 | 8.676 E-12 |
| 0.2980 | 8.634 E-12 | | 0.2961 | 8.488 E-12 |
| 0.3965 | 8.512 E-12 | | 0.3931 | 8.385 E-12 |
| 0.4946 | 8.430 E-12 | | 0.4892 | 8.305 E-12 |
| 0.9781 | 8.163 E-12 | | 0.9567 | 7.993 E-12 |
| 1.4546 | 8.596 E-12 | | 1.4060 | 8.017 E-12 |
| AVE | 8.829 E-12 | | AVE | 8.560 E-12 |

CFD simulation was also conducted using 5 rows of 2 mm diameter granules and capsular cylinders to obstruct the air flow and pressure drop was calculated. The capsule shape is shown in figure 4.33. The capsules are 10 mm long (height of honeycomb) and have diameter of 2 mm (average size of particles).

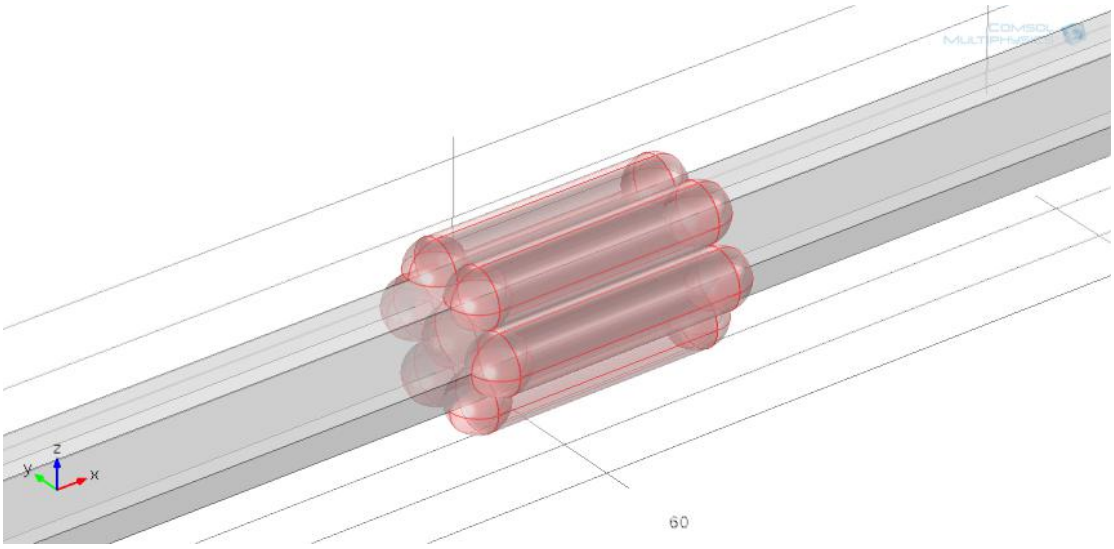

**Figure 4.33 granules modeled with capsule-shaped geometry**

Figure 3.34 compares the pressure drop variation with velocity for the 5 rows of 2mm spherical granules and the capsules with 2mm diameter. It can be seen that the capsular geometry produce lower pressure drop values compared to the 5 rows of spherical granules.

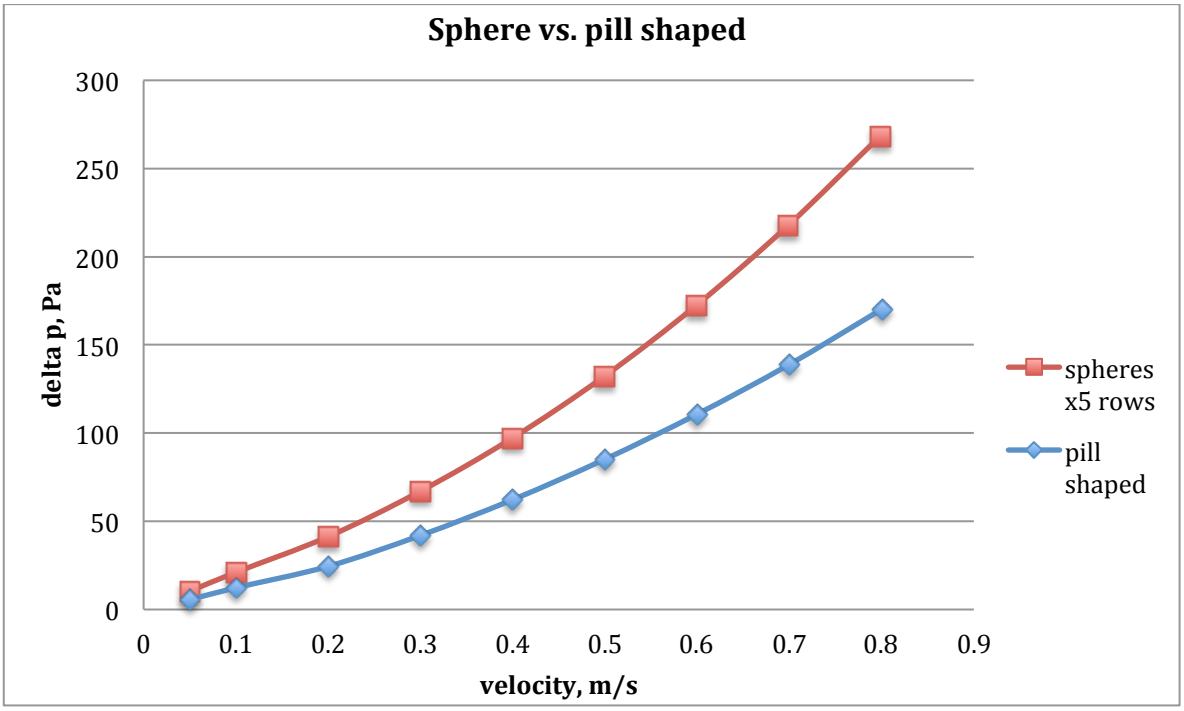


**Figure 4.34 comparison of pressure drop caused by spherical and capsular obstruction**

The K values were calculated at low velocity from the CFD results and the average value was K=1.20971E-9 for capsules. The K values for the spherical granules were calculated and averaged to be around 6.895E-10. The K values were then used in the honeycomb and mesh geometry to fill the honeycomb cells as porous material in the next section of research.

For the granules, the volume of the honeycomb cells can be filled with a porous material that has a porosity of 0.41 [64, 65]. This value is the void fraction for modeling loose random packing of spherical particles, which can be used to describe spherical particles packed by hand or spheres dropped into a bed. In the experiment, the spherical granules were packed by hand. The various materials modeled as porous media are summarized in table 4.5.

**Table 4.5 Materials modelled as porous media**

| Material modeled as porous media | Porosity, $\epsilon$ , or $\beta$ value | Permeability K |
|---|---|---|
| **Mesh (150x0.047)** | 0.474 | 1.160E-10 |
| **Mesh (500x0.025)** | 0.258 | 1.692e-10 |
| **Granules (spherical)** | 0.410 | 6.895E-10 |
| **Granules (capsular)** | 0.410 | 1.2097E-9 |

### *4.3 Honeycomb structure integrated with mesh*

Figure 4.35 shows the setup of the honeycomb test section modelled in 3D using COMSOL Multiphysics software. The inlet is placed 31 mm from the obstruction which in this case is the honeycomb structure, and the outlet is 56 mm downstream from the tested sample as used in the simulations carried out in the previous section 4.2.

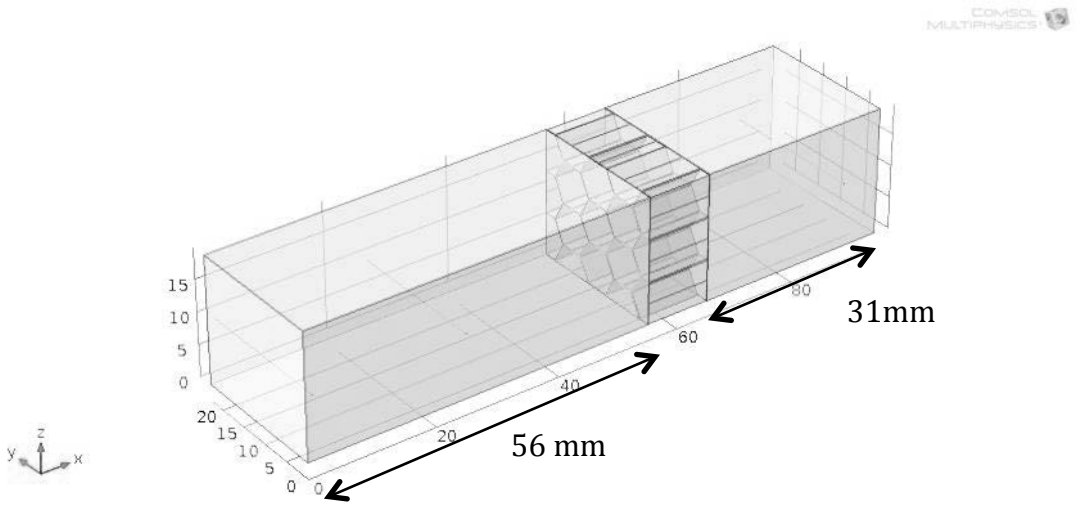


**Figure 4.35 CFD model geometry**

Figure 4.36 shows the boundary conditions implemented in the modeling where pressure, no viscous stress was applied at inlet and velocity, normal outflow was applied at outlet.

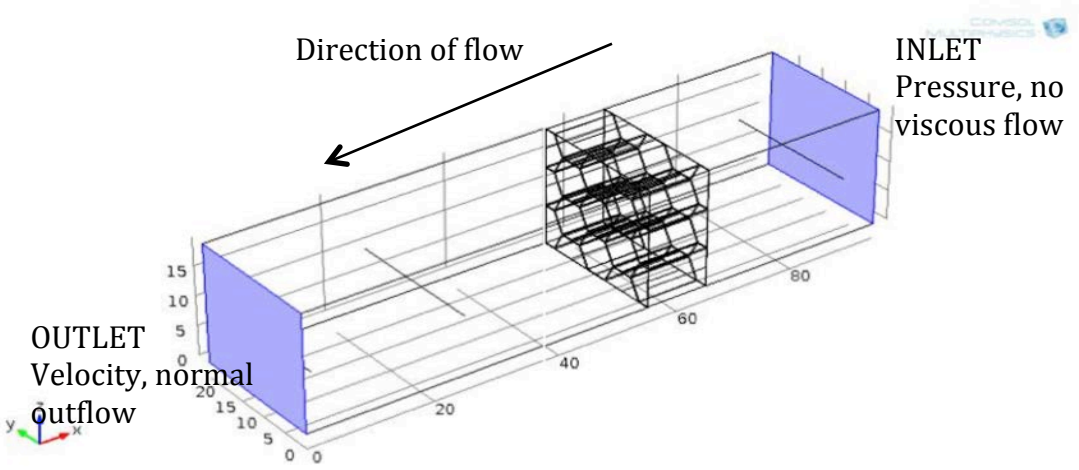


**Figure 4.36 Boundary conditions: inlet and outlet**

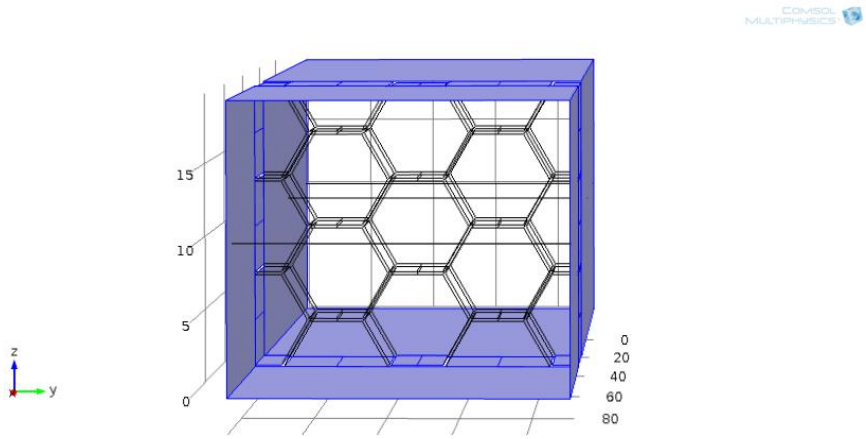

**Figure 4.37 Boundary condition: symmetry (in blue) on four sides**

The CFD air duct cross sectional area is 22.9×19.8 mm and contains seven complete cells of honeycomb and 10 half cells as shown in Figure 4.37. Each cell of the honeycomb has a height of 6.4 mm and the cell wall thickness is 0.2 mm as modeled according to the honeycomb used in the experiment. Around the four sides of the whole unit the boundary conditions have been set as symmetry so that the simulation can be performed for repeating units of the honeycomb section above.

CFD runs were carried out for the geometry without the mesh sheets sandwiching the honeycomb to observe the range of pressure drop caused by the honeycomb itself. From the results it was seen that for a range of velocity 0.05 to

5.5 m/s, the maximum pressure drop across the honeycomb was only 18 Pa at 5.5 m/s as shown in Figure 4.38.

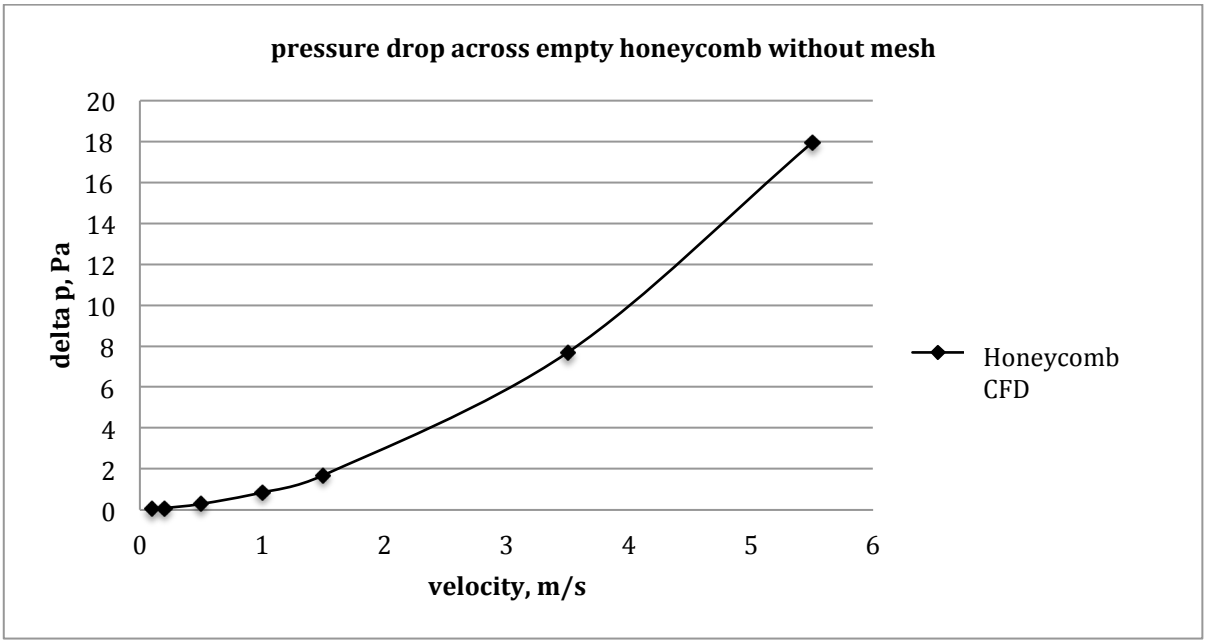


**Figure 4.38 Pressure drop caused by honeycomb**

Figure 4.39 shows the honeycomb test section integrated with two mesh sheets, one at inlet and another at outlet. The CFD simulation of the 3D geometry of the honeycomb and mesh sheets was carried out with the mesh sheets modelled as porous material. The porous material properties that have to be user defined are the permeability and porosity as explained in section 4.2. Using the formula for permeability, the average value of K for the mesh sheet was obtained using the calculated values of K derived from CFD results described in section 4.1 involving single mesh sheets and the value is K=1.16e-10 for mesh 150x0.047. In this case, the average value of K was calculated from CFD data values of low velocity simulations of less than 2 m/s. This is because within an adsorption cooling system, the air flow is usually below 2 m/s. For the porosity, the formula for finding $\beta$ free volume area can be used as the porosity. For the fine mesh sheet 150x0.047, the value of porosity that was used in the model was 0.474.

The CFD set up was then repeated several times using steady state studies at different velocities corresponding to the velocities that were obtained from the experimental results.

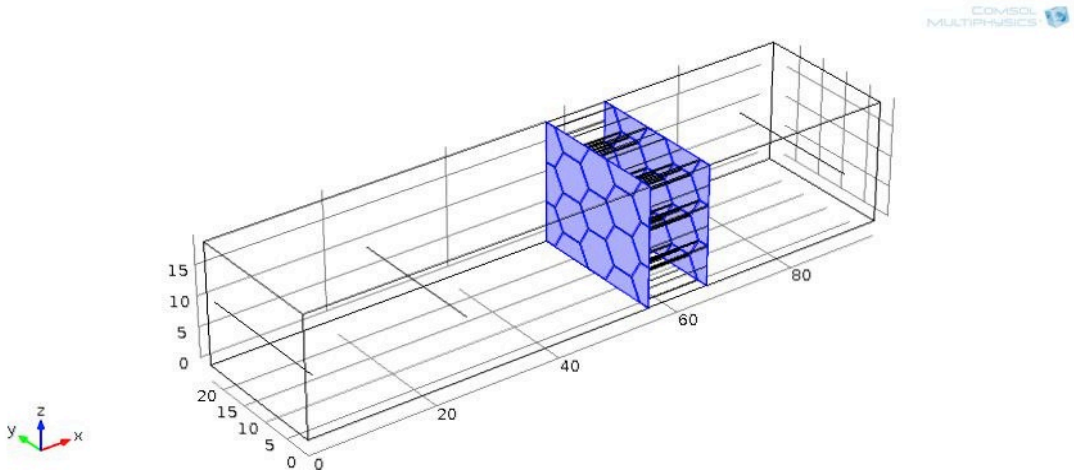


**Figure 4.39 Position of mesh (in blue) modeled as porous material**

For a steady state study of outlet velocity $u$, the governing equations used by the CFD solver for 'free and porous media flow' are

$$\rho(u.\nabla)u = \nabla.[-pl + \mu(\nabla u + (\nabla u)^T)] + F \quad \text{(Eq. 23)}$$

$$\rho\nabla.u = 0 \quad \text{(Eq. 24)}$$

$$\frac{\rho}{\epsilon_p}\left((u.\nabla)\frac{u}{\epsilon_p}\right) = \nabla.\left[-pl + \frac{u}{\epsilon_p}(\nabla u + (\nabla u)^T) - \frac{2\mu}{3\epsilon_p}(u.\nabla)l\right] - \left(\frac{\mu}{K_{br}} + \beta_F|u| + \frac{Q_{br}}{\epsilon_p^2}\right) + F \quad \text{(Eq. 25)}$$

$$\rho\nabla.u = Q_{br} \quad \text{(Eq. 26)}$$

The other equations used by the solver for the inlet, outlet and wall boundary conditions are

Inlet:

$$p = p_0\,,\ [\mu(\nabla u + (\nabla u)^T)]n = 0 \quad \text{(Eq. 27)}$$

Outlet:

$$u = U_0 n \quad \text{(Eq. 28)}$$

Wall:

$$u.n = 0 \quad \text{(Eq. 29)}$$

$$\left[(\mu + \mu_T)((\nabla u + (\nabla u)^T) - \frac{2}{3}(\mu + \mu_T)(\nabla.u)l - \frac{2}{3}\rho kl\right]n = -\rho\frac{u_\tau}{\delta_w^+}u_{tang} \quad \text{(Eq. 30)}$$

$$u_{tang} = u - (u.n)n \quad \text{(Eq. 31)}$$

$$\nabla k.n = 0,\ \epsilon = \rho\frac{C_\mu k^2}{k_v\delta_w^+\mu} \quad \text{(Eq. 32, 33)}$$

Figure 4.40 show the velocity at different parts of the air duct at velocities 1.84 m/s and 5.66 m/s. It can be seen that directly downstream of the honeycomb and mesh unit, the velocity is highest at air flow through the centre of honeycomb cells and the lowest velocities (blue regions) are caused by the cell walls.

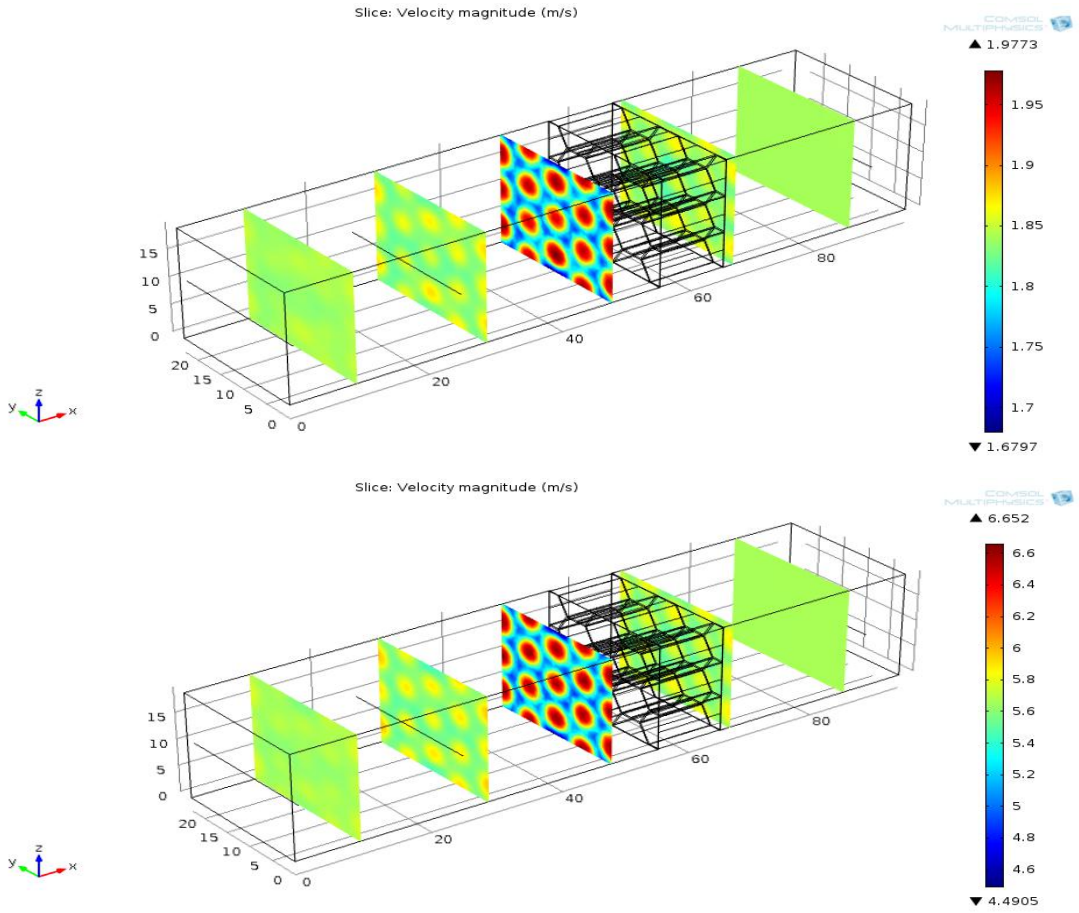


**Figure 4.40 velocity slices along air duct for 1.84 m/s (top) and 5.66 m/s (bottom)**

Further observation into the air velocity behavior is done by making a 3D cut line through the midpoint of the central honeycomb cell of the honeycomb assembly geometry, shown in the Figure 4.41 as the red line going through the whole length of the geometry. Using this line, the changes in velocity and pressure can be plotted to observe their variation as air moves from the inlet, through the first mesh, through the empty honeycomb cell, through the second mesh and to the outlet of the duct.

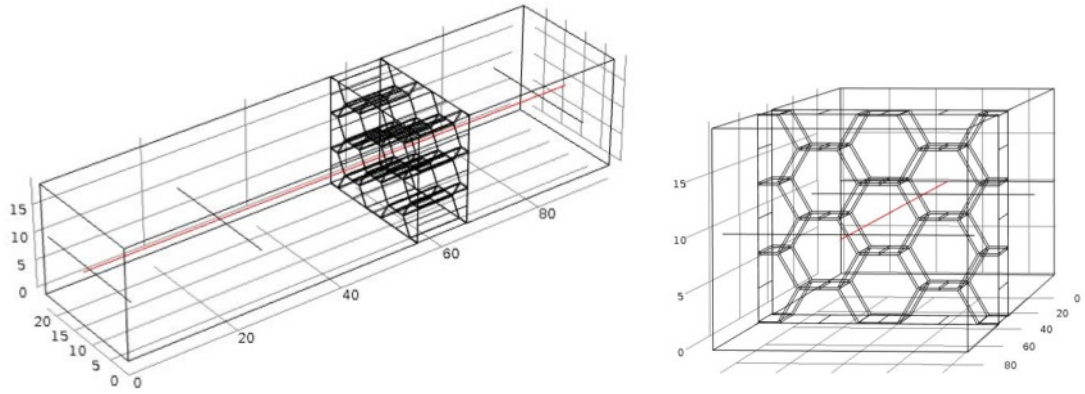

**Figure 4.41 position of cut-line (in red) through centre of honeycomb section**

Figures 4.42 and 4.43 show the velocity change along the cut line (red line in figure 4.41) can be seen below for velocities 1.84m/s and 5.66 m/s. From the figures it can be seen that the biggest difference is that for the lower velocity simulation, the downstream velocity returns to 1.84 m/s more quickly than the high velocity simulation where the velocity returns back to 5.66 m/s downstream more gradually.

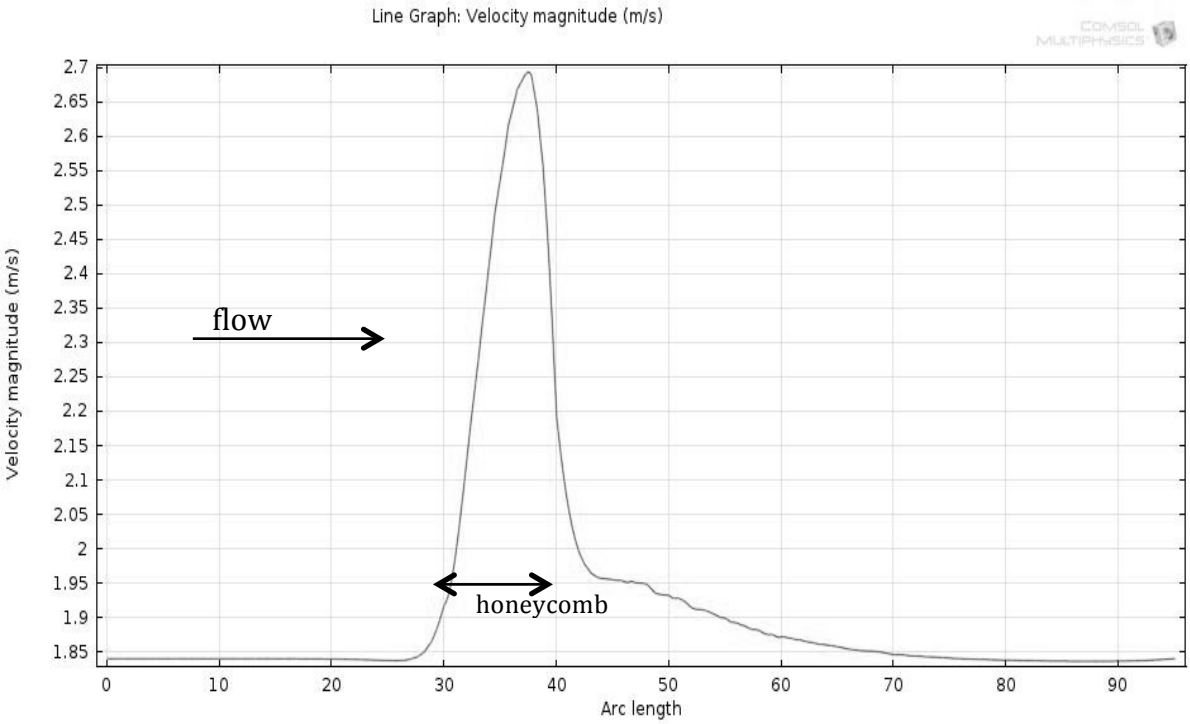


**Figure 4.42 velocity variation along cut line for air duct under 1.84 m/s flow**

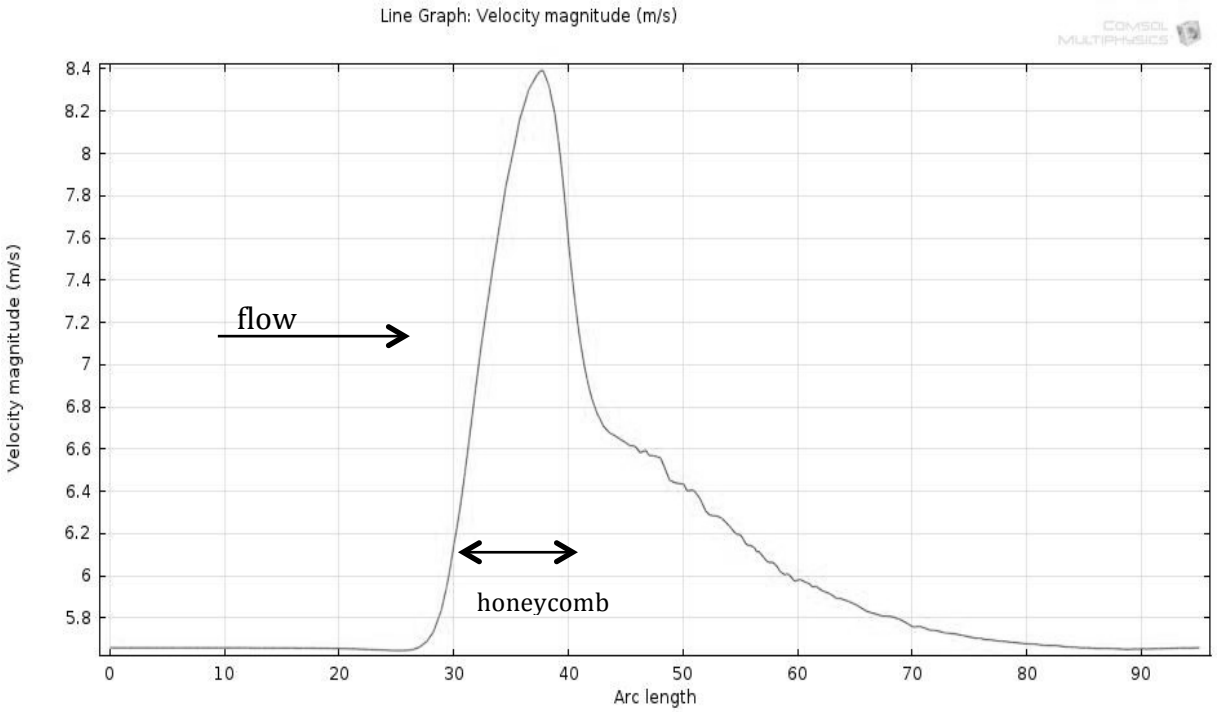


**Figure 4.43 velocity variation through honeycomb for air duct under 5.66 m/s flow**

For the 1.84 m/s flow, the honeycomb only achieved an increase of 0.86 m/s up to the maximum point whereas in the case of the 5.66 m/s flow increased as much as 2.74 m/s to reach a maximum of 8.4 m/s. The gradual decrease of velocity in the above graph can be explained by figures 4.44 and 4.45 where the regions of high velocity downstream are in deeper red. For the 5.66 m/s flow, the high velocity region tails down past the honeycomb for longer than the 1.84 m/s flow. The velocity increase caused by the honeycomb cells is retained for longer.

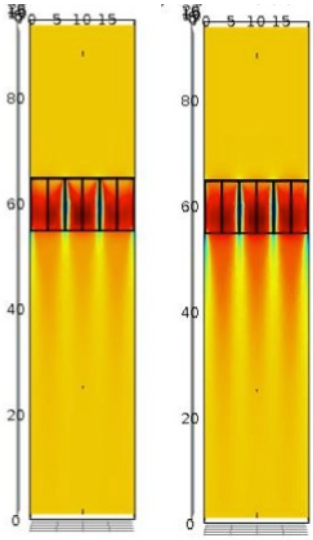


**Figure 4.44 velocity slices for 1.84 m/s (Left) and 5.66 m/s (Right)**

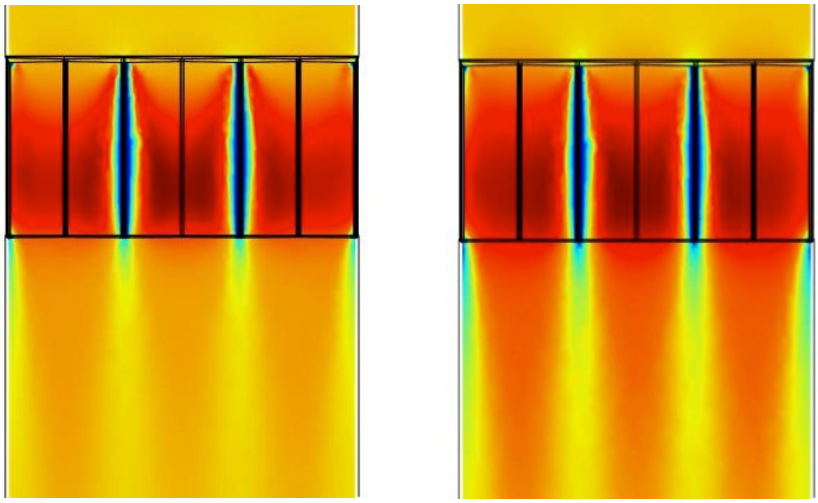

**Figure 4.45 velocity slices showing the regions of high velocity in dark red for ducts with velocity 1.84 m/s (left) and 5.66 m/s (right)**

Figures 4.46 and 4.47 show the variation of pressure along the line going through the centre of the hexagonal honeycomb cell for the velocities 1.84 m/s and 5.66 m/s, respectively. For both of the pressure graphs, there is a pressure drop happening for the first two thirds of the thickness of the honeycomb and then there is a pressure increase in the last third due to the flow being blocked by the second mesh. It must be noted that the scales of the graphs are different where in the first graph it shows overall pressure drop of 32 Pa whereas in the second graph it shows an overall pressure drop of 115 Pa. Also the pressure drop between p1 and q1 which is the overall pressure drop caused by the honeycomb

is only 1 Pa whereas for p2-q2, the pressure drop is larger around 10 Pa. For both of these velocities, it can be concluded that the mesh sheets cause the majority of the pressure drop and the pressure drop caused by the honeycomb is very small therefore would only have a small effect on pressure drop if the honeycomb was packed with adsorbent granules to be modelled as a representative bed.

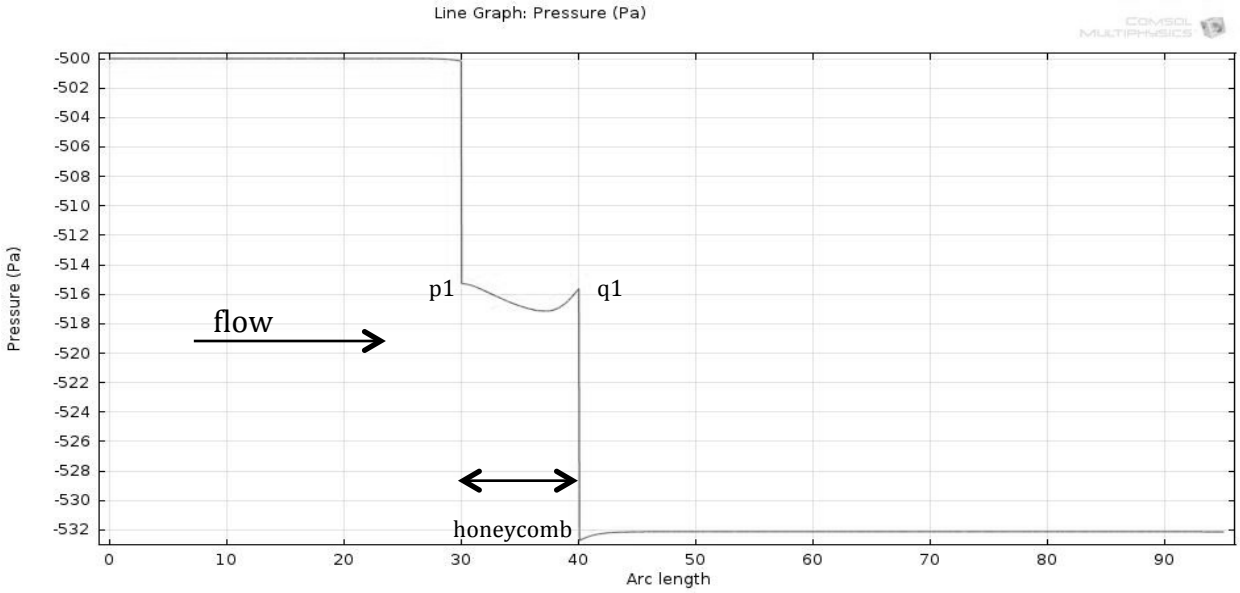


**Figure 4.46 pressure variation along the air duct passing through honeycomb and mesh structure caused by flow 1.84 m/s**

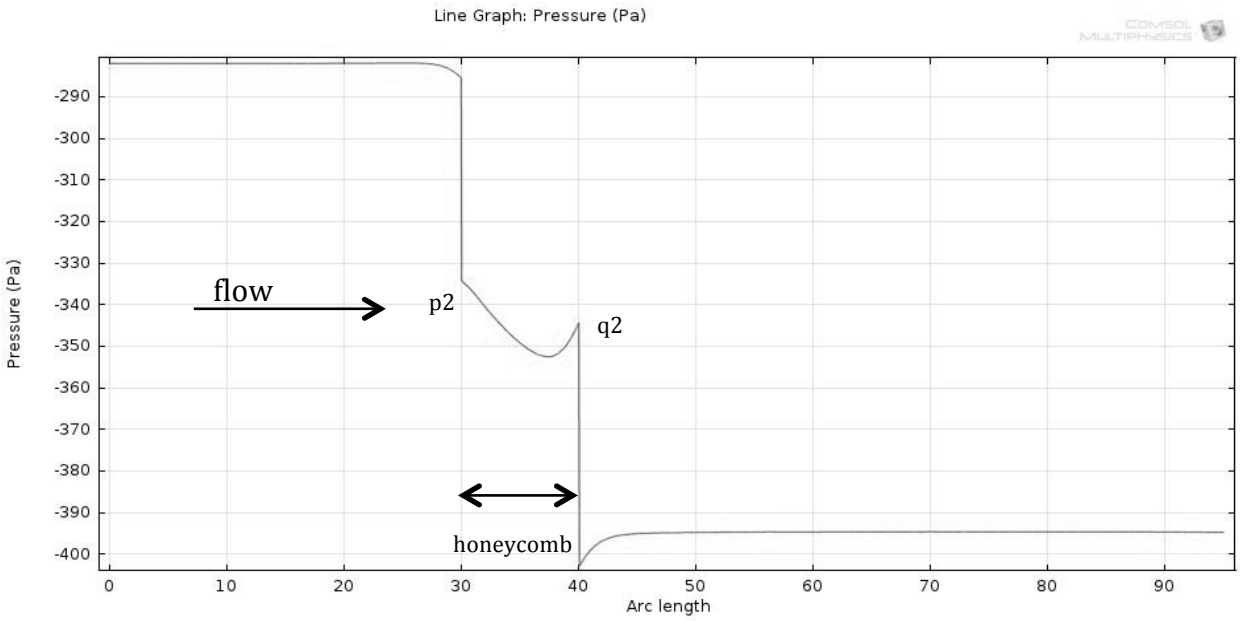


**Figure 4.47 pressure variaton along the air duct passing through honeycomb and mesh structure caused by flow 5.66 m/s**

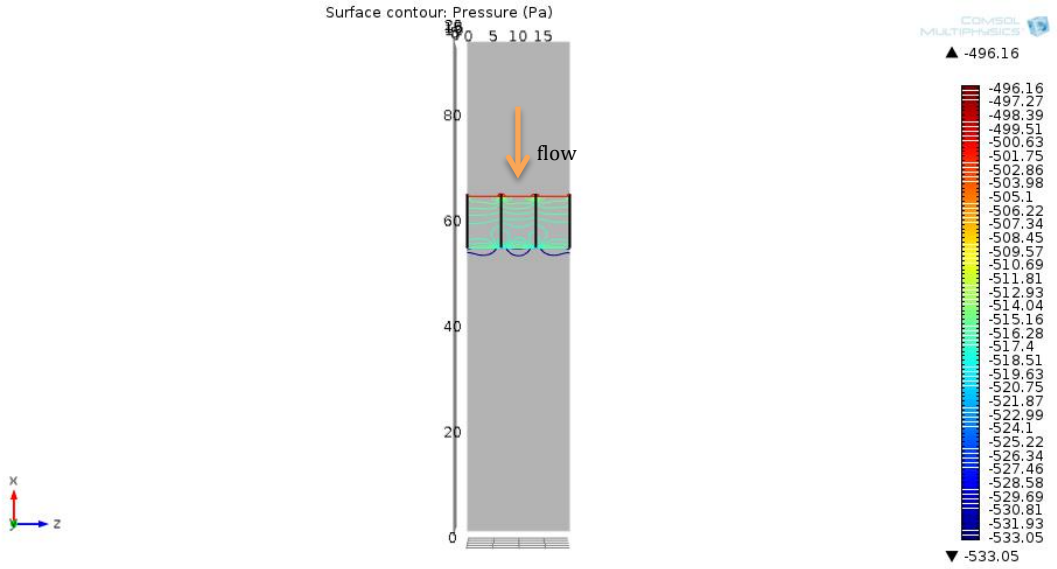


**Figure 4.48 Pressure gradient lines in air duct solution showing all pressure change occurring near and within honeycomb (velocity 1.84 m/s)**

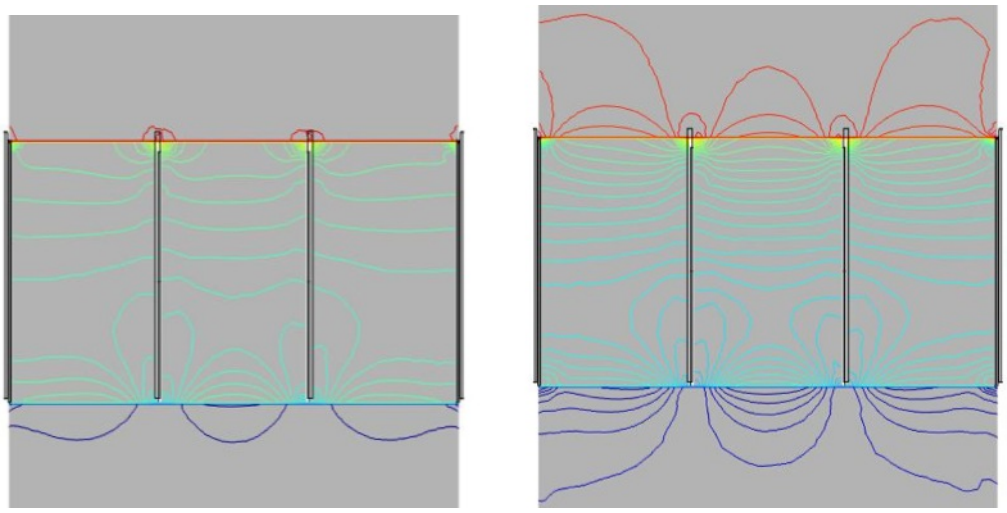

**Figure 4.49 showing pressure gradient pattern for velocity 1.84 m/s (left) and 5.66 m/s (right)**

From Figures 4.48 and 4.49, it can also be seen that all of the pressure drop occurs within the honeycomb and the region directly before and after it. It can be seen from the pressure contours of velocity 5.66 m/s, there are more pressure lines within the honeycomb structure, especially built up front of the second mesh. The pressure drop across the mesh sheets cannot be properly observed because the mesh sheets are very thin but from the pressure contours it can be observed that the most contrasting colour changes occur at the mesh sheets. As

the contour lines (in both figures) reach the first mesh sheets, the colour drastically changes from red to light green and does not show the normal gradient-type colour change. Similarly the light green lines rapidly change to dark blue lines at the second mesh sheet location. Also observed is pressure increase that is built up in front of the honeycomb cell walls where small red semi-circular lines can be observed at the end of the cell wall. There are also areas of low pressure caused at the tail end of the cell walls due to the wake caused by these solid structures.

For the CFD simulation of honeycomb integrated with 500x0.025 mesh, the thickness of the mesh sheet geometry was changed from 0.047 (mesh size 150 geometry) to 0.025, which is the thickness of the size 500 mesh. Due to this very thin section, the geometry of the model needed to be meshed in two stages with different mesh qualities. For the main domain of the geometry excluding the mesh sheets geometry, the mesh chosen was free tetrahedral fluid dynamics with pre-defined 'fine' mesh quality and for the thin blue parts highlighted in figure 4.39 the 'extra fine' pre-defined quality was used. This is because for the 'fine' and 'extra fine' computational mesh qualities, the region (0.025 mm thickness) was too narrow for the minimum element size, as described in table 4.5.

**Table 4.6 showing element size settings for different pre-defined compuational mesh qualities**

| Predefined mesh quality | Normal | Fine | Finer | Extra fine | Extremely fine |
|---|---|---|---|---|---|
| **Max. element size (mm)** | 0.398 | 0.315 | 0.22 | 0.137 | 0.0772 |
| **Min. element size (mm)** | 0.119 | 0.0594 | 0.0238 | 0.00891 | 0.00119 |
| **Max. element growth rate** | 1.15 | 1.13 | 1.1 | 1.08 | 1.05 |
| **Resolution of curvature** | 0.6 | 0.5 | 0.4 | 0.3 | 0.2 |
| **Resolution of narrow regions** | 0.7 | 0.8 | 0.9 | 0.95 | 1 |

Similar to the previous CFD for 150 size mesh sheet and honeycomb, the main physics module used in this simulation is the 'Free and Porous Media Flow' and the values for void fraction ($\epsilon$) and permeability (K) for the mesh sheets need to be user-defined. For the new mesh size 500x0.025, K=1.692e-10 and $\epsilon$=0.2579. The value of K for the new mesh seems very low but this is due to the very fine wire diameter for this particular mesh that is 0.025 mm compared to the 0.047 mm of the one previously tested and modeled.

### *4.4 CFD modeling of honeycomb structure packed with granular adsorbent material*

The CFD model of the packed honeycomb was carried out to simulate the airflow and predict the pressure drop across the unit. Here, the modelling of the packed honeycomb test section with the mesh at both sides utilized the modeling results of the mesh carried out in section 4.1 and the modeling of the porous material carried out in section 4.2.

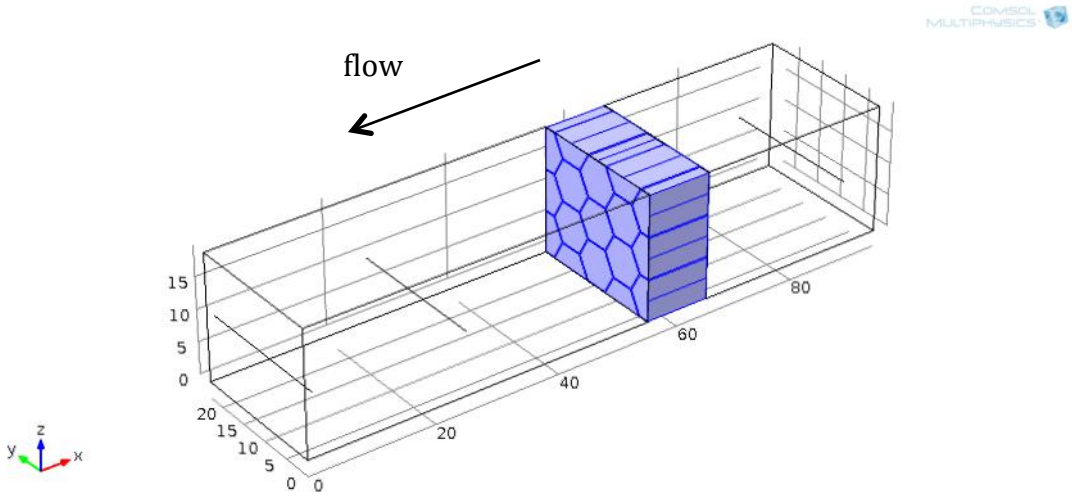


**Figure 4.50 showing domain set as porous material to model granules**

For the two mesh sheets covering the honeycomb, the void fraction and the permeability stays the same as the empty honeycomb CFD, which are 0.474 and 1.16e-10 respectively. From section 4.2, two values of K were obtained using spherical and capsular granule models. The values were 6.895e-10 and 1.2097e-9. For the granule domain filling the honeycomb cells, the values stay the same, K=1.2097e-9 and $\epsilon$= 0.41 for both tests with 150x0.047 and 500x0.025 meshes.

These values were then used in CFD modeling as the value of K for the user defined permeability value for porous material used for filling the honeycomb cells (blue section in figure 4.50). Other than setting the porous material to fill the honeycomb cell instead of just having air, this run of the CFD has the same boundary conditions, physics module, mesh settings and steady state simulation was carried out at increasing velocity steps. The porosity also known as the void fraction of the porous material that represents the granules were set to a value of

0.41 which is the void fraction of spherical granules packed into a bed by hand, which is what has been done in the experimental set-up.

Similar to the previous CFD for 150 size mesh sheet and honeycomb, the main physics module used in this simulation is the 'Free and Porous Media Flow' and the values for void fraction ($\epsilon$) and permeability (K) for the granule volume and mesh sheets need to be user-defined. For the granule domain in the honeycomb cells, the values stay the same, K=1.2097e-9 and $\epsilon$= 0.41. For the new mesh size 500x0.025, K=1.692e-10 and $\epsilon$=0.2579. The value of K for the new mesh seems very low but this is due to the very fine wire diameter for this particular mesh that is 0.025 mm compared to the 0.047 mm of the one previously modeled.

Similar to the velocity analysis done in the empty honeycomb CFD set-up, the following velocity and pressure graphs were taken on the line going from the inlet to the outlet of the geometry via the centre of one of the honeycomb cells (red line in figure 4.41). The change in velocity along the line from inlet to outlet is shown in figure 4.51 for velocity of 0.428 m/s and figure 4.52 for velocity of 2.955 m/s.

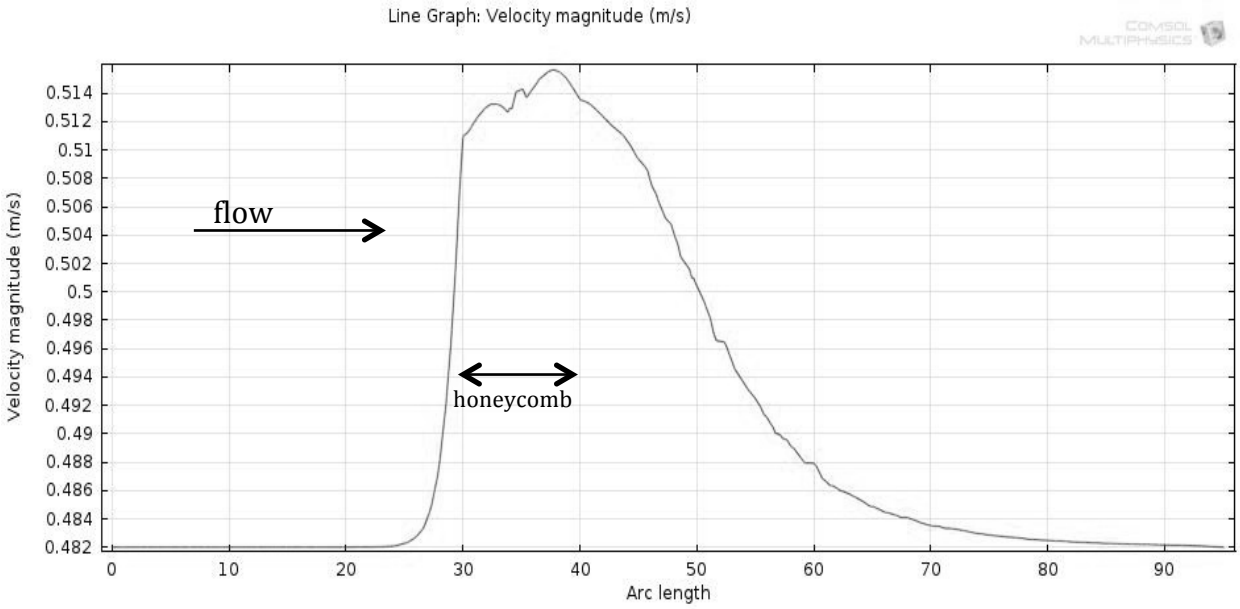


**Figure 4.51 velocity variation along air duct, passing through filled honeycomb, with flow 0.482 m/s**

It can be seen that the velocity curve is not smooth after the first mesh sheet and the increase in velocity with the honeycomb cell filled with granules is unstable and contains a couple of dips in the peak curve. Additionally, the graph has a significantly wider curved shaped compared to when the honeycomb is not filled with granules. For the 2.955 m/s velocity graph in figure 3.52, there is an obvious dip in velocity that occurs within the packed honeycomb structure.

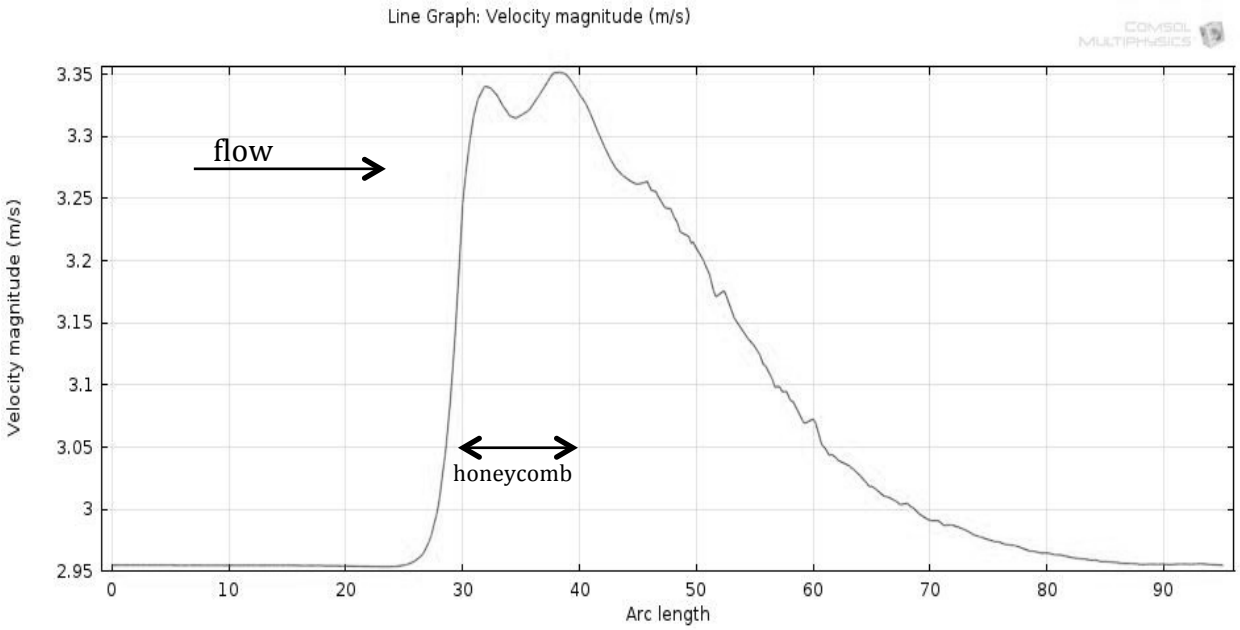


**Figure 4.52 velocity variation along air duct, passing through filled honeycomb, with flow 2.955 m/s**

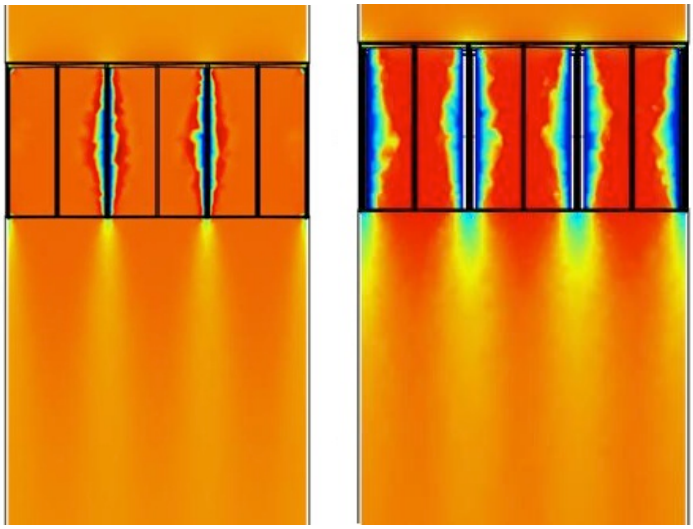

**Figure 4.53 velocity profile 0.482 m/s (left) and 2.955 m/s (right)**

Figure 4.53 shows that there is a bigger blue region on the sides of the honeycomb cell walls under 2.955 m/s flow, compared to the 0.482 m/s flow. The dip in the velocity shown in figure 4.52 may be caused by the thick boundary layer of lower velocity (blue region) near the walls of the honeycomb, potentially caused by the porous material in the honeycomb cells.

Figure 4.54 and 4.55 show the pressure variation along the line passing through the centre of the packed honeycomb test section for flow velocity of 0.482 m/s and 2.955 m/s, respectively. It can be seen that the pressure drop pattern is exactly the same except for the degree of overall pressure drop for the lower velocity is about 90 Pa and for the higher velocity it is from 500 Pa. However, both have the same pressure drop behavior across the honeycomb where the pressure drops at a linear manner across the granule geometry that has been modeled as porous material. Also for both velocities, most of the pressure drop has been caused by the granules filling honeycomb compared to the very small pressure drop caused by the mesh sheets.

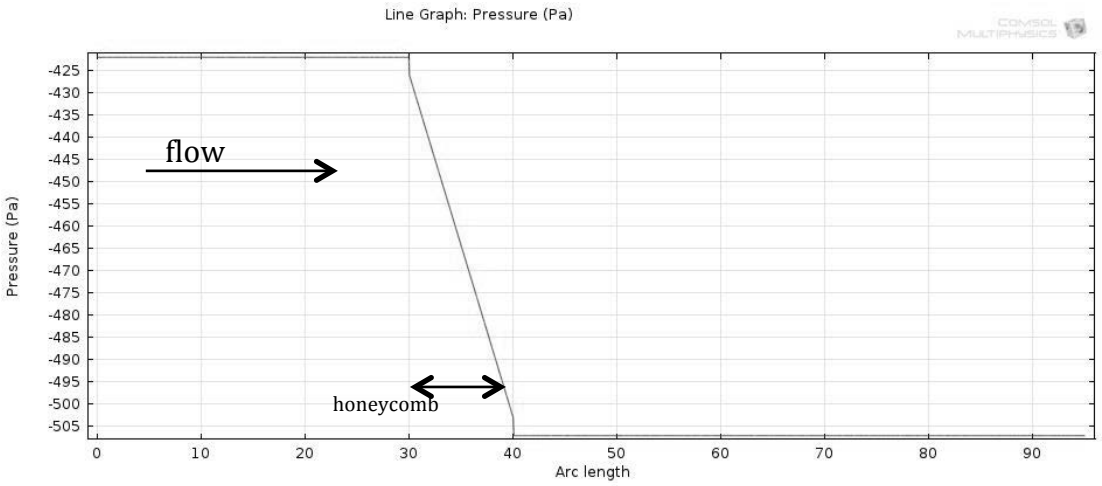


**Figure 4.54 pressure drop variation along air duct geometry with filled honeycomb, flow 0.482 m/s**

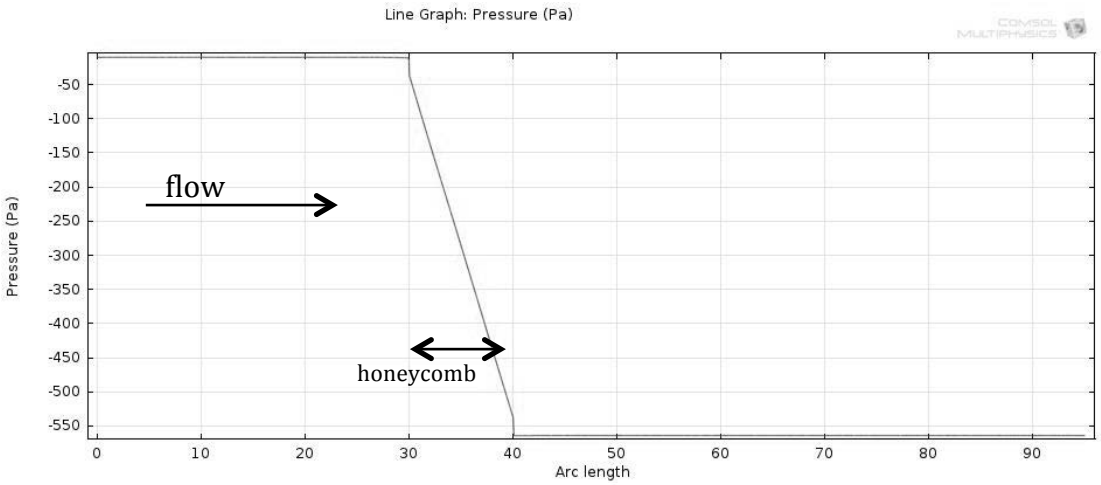


**Figure 4.55 pressure drop variation along air duct geometry with filled honeycomb, flow 2.955 m/s**

In figure 4.56, pressure drop can be seen to occur mainly within the filled honeycomb due to significant colour change from red to blue within the honeycomb geometry thickness.

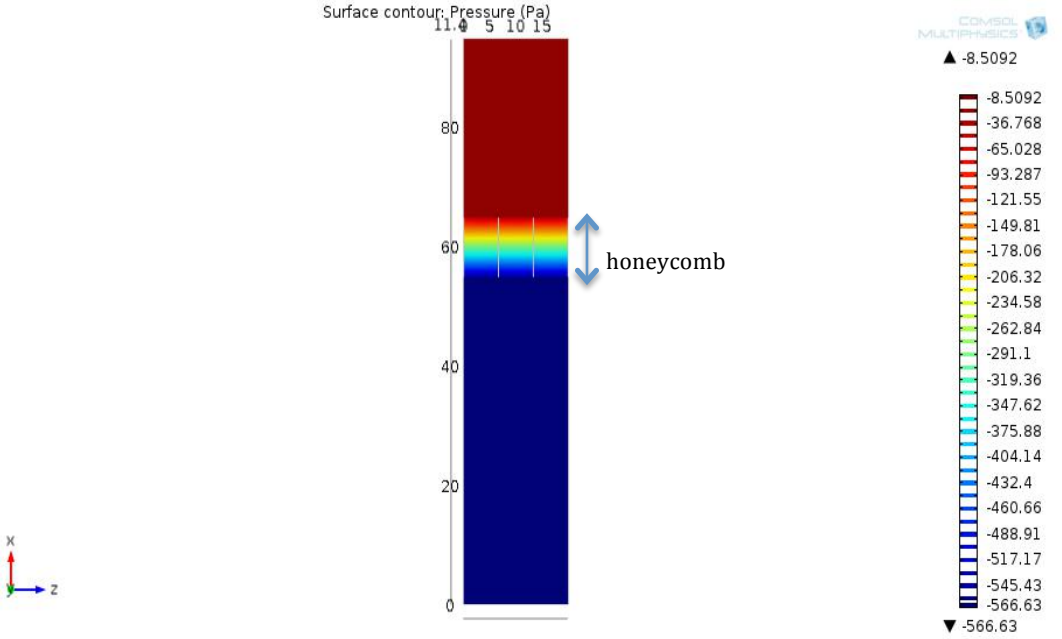


**Figure 4.56 Pressure slice along cross section of air duct**

Figure 4.57 compares the velocity of the empty honeycomb at 3.6 m/s and filled honeycomb at 3.0 m/s. It can be observed that the filled honeycomb, even at a velocity 0.6 m/s lower than the empty honeycomb, caused a more obvious blue region of flow velocity. The red regions have not increased in size so it must mean that the intermediate region between blue and red in the second figure

below must be smaller and the velocity changes from high to low outwards in a narrow region. For the empty honeycomb, there are more intermediate regions (green).

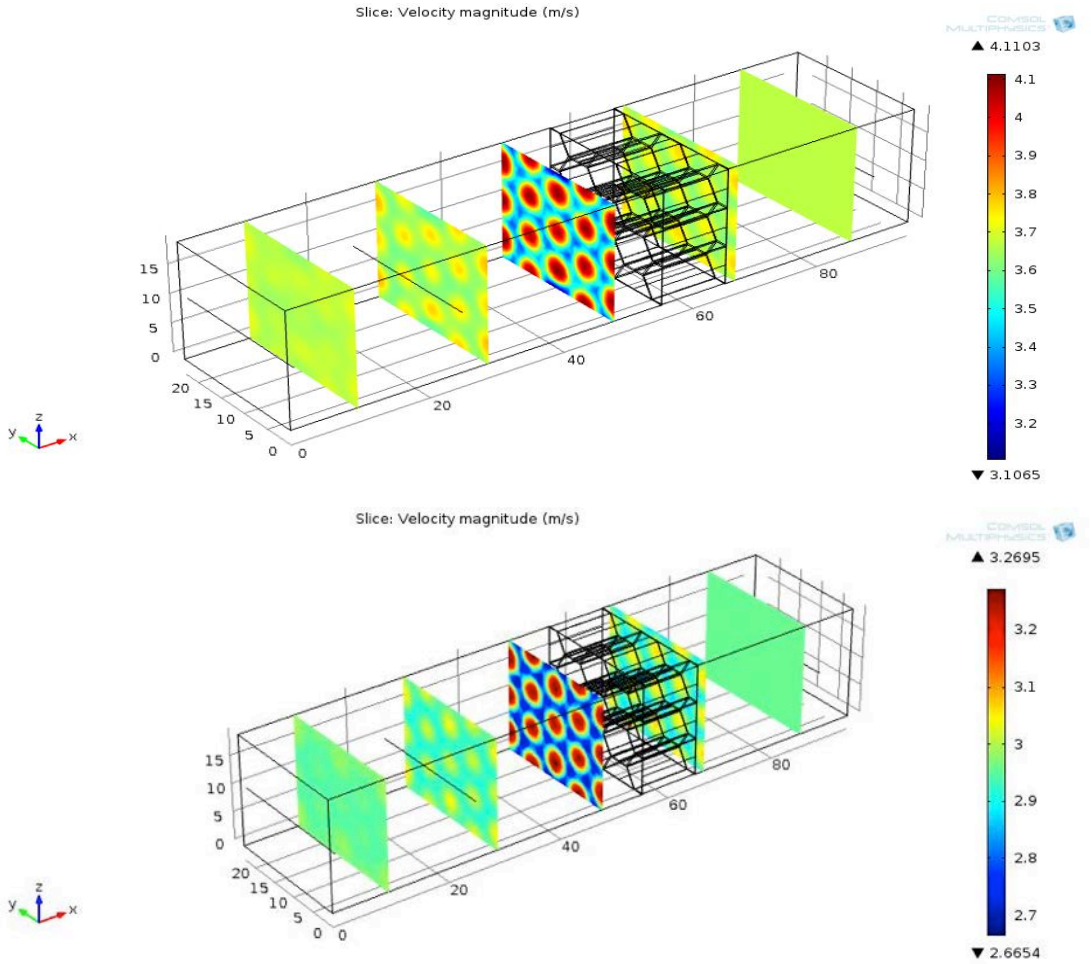


**Figure 4.57 velocity slices of empty honeycomb with flow 3.6 m/s (top) and filled honeycomb with flow 3.0 m/s (bottom)**

### *4.5 Summary*

From the first section of this chapter, it can be seen that pressure drop increases proportional to the air flow velocity. For the different mesh sizes, the difference in upstream and downstream pressure, Δp, is inversely proportional to β, the free hole area ratio which is a function of the mesh sheet wire diameter and number of wires per inch. This parameter β is also known as the void fraction or porosity. The experimental set-up using the mesh sheets can be modelled using

CFD with two-dimensional non-compressible flow and modelling the wires with circular cross-section.

The findings of the CFD analyses show that the using the small hexagonal geometry configuration is sufficient to predict pressure drop behavior. As the geometry increases in cross-sectional area with more repeated pattern of hexagonally arranged granules, the pressure drop characteristics remain the same so a smaller geometry can be used with reasonable confidence in CFD modeling as to save computing power and time.

# *Chapter 5* Experimental results and CFD validation

This chapter presents the experimental results and the CFD simulation comparisons. Section 5.1 presents the results for the air flow analysis through a single sheet of woven metal mesh, as well as the CFD results. Section 5.2 will describe the results for the empty honeycomb integrated with meshes 150x0.047 and 500x0.025 and section 5.3 is for results for the honeycomb when packed with adsorbent granules. Section 5.4 provides a summary of the main conclusion from this chapter.

## *5.1 Experimental results for single mesh sheet experiment and CFD comparison*

Figures 5.1-5.4 show the variation of static pressure downstream and upstream of the mesh test pieces at different air flow velocities.

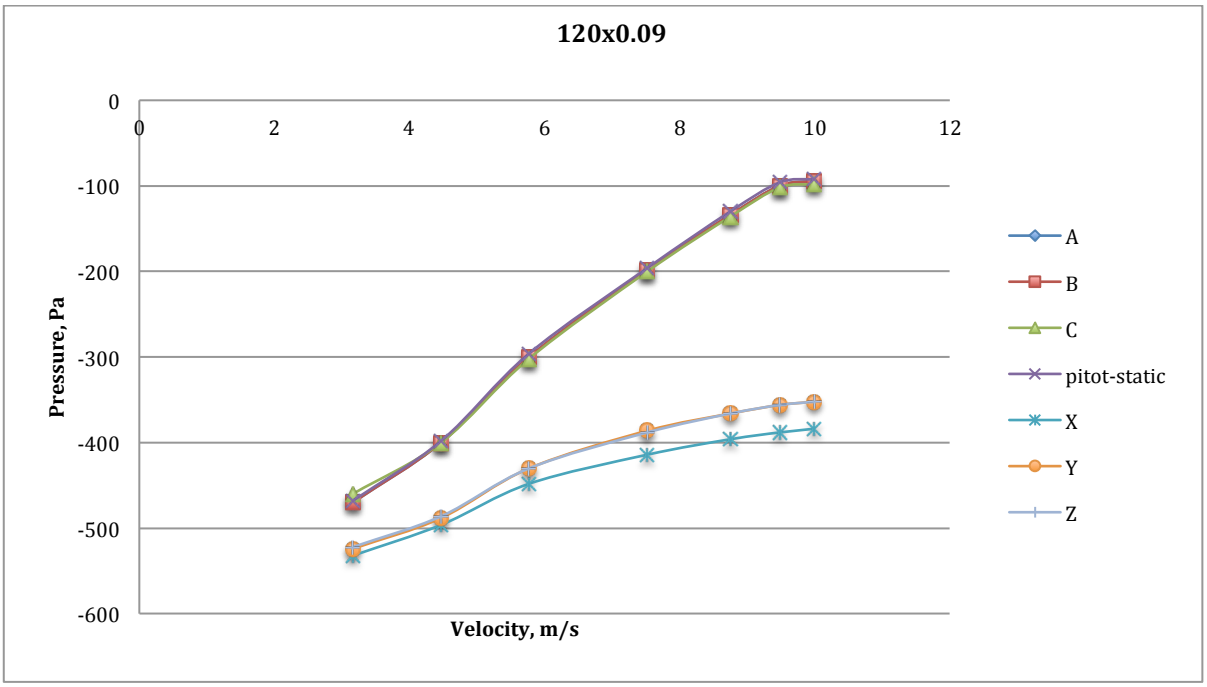


**Figure 5.1 Measured pressure at tappings upstream and downstream of mesh size 120x0.09**

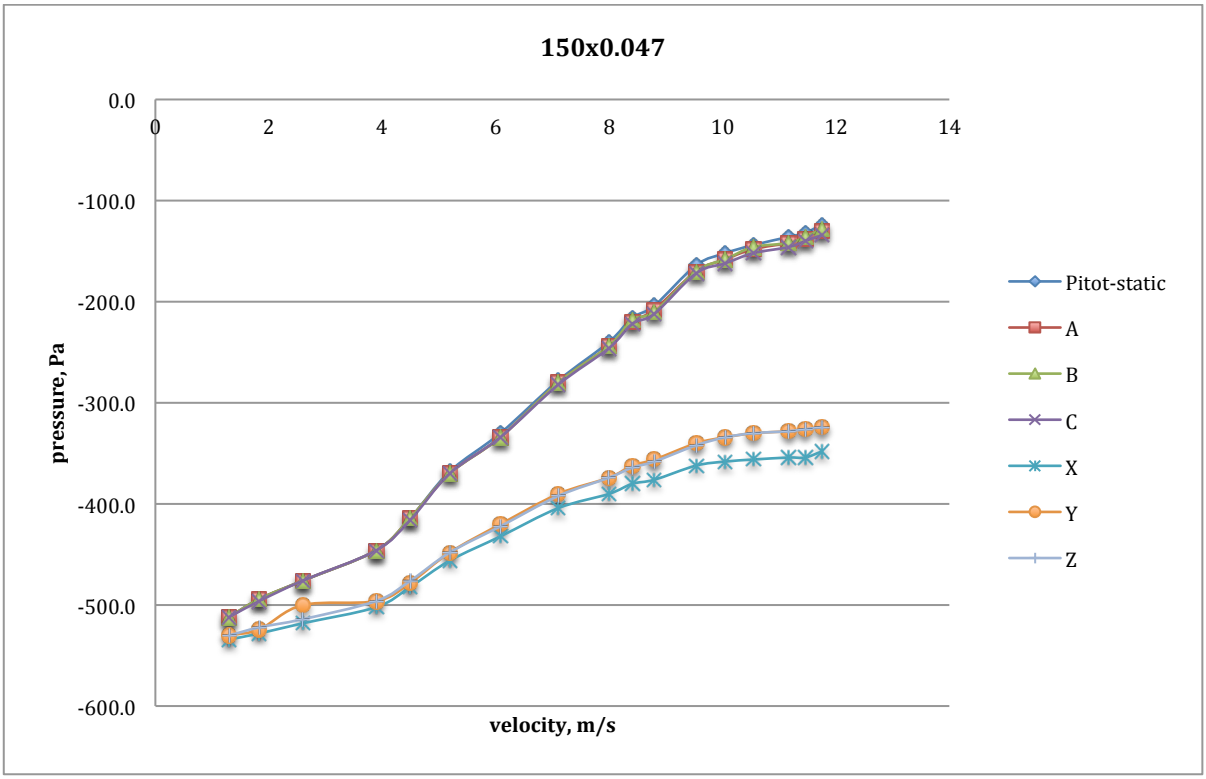


**Figure 5.2 Measured pressure at tappings upstream and downstream of mesh size 150x0.047**

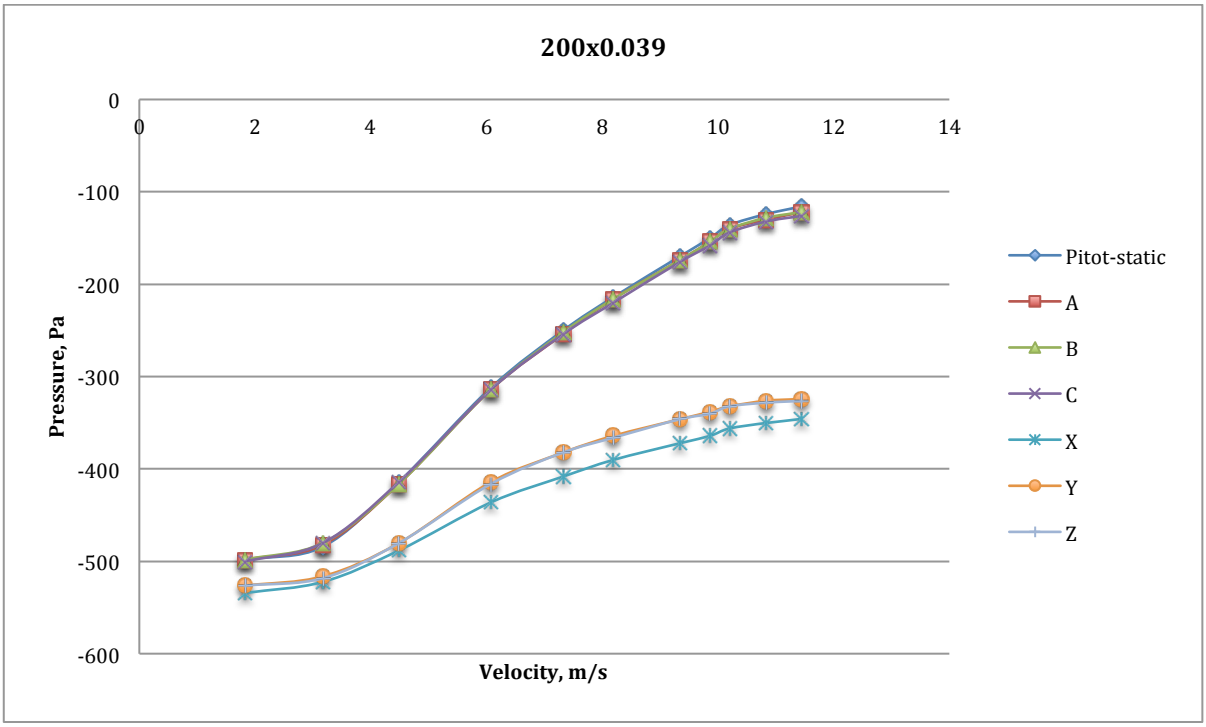


**Figure 5.3 Measured pressure at tappings upstream and downstream of mesh size 200x0.039**

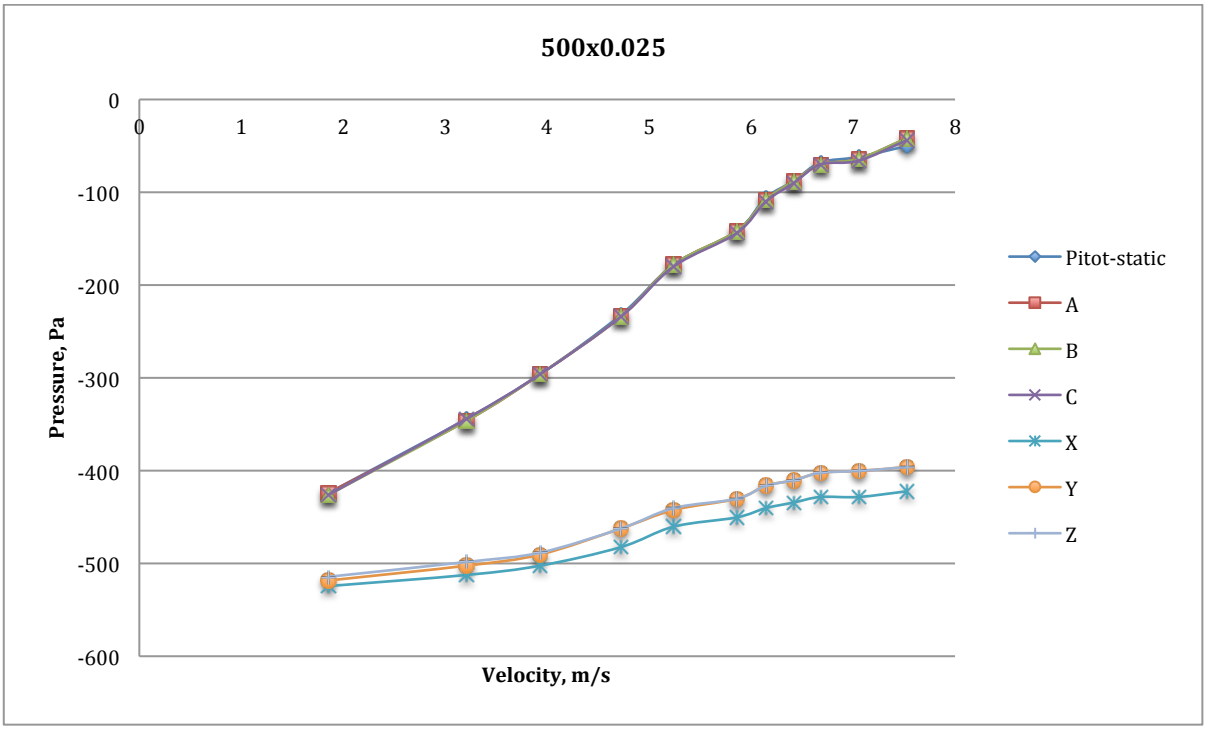


**Figure 5.4 Measured pressure at tappings upstream and downstream of mesh size 500x0.025**

For the four different meshes (Figure 5.1-5.4), values of static pressure upstream of the mesh (pitot-static, A, B and C) overlap meaning that the values are similar. Downstream of the mesh screens, the static pressure values were also similar but for point X that is nearest to the mesh, the pressure values have a higher negative value compared to Y and Z. This indicates that the flow has become fully developed after the mesh at point Y. Therefore, the pressure measurement can be taken between points C and Y with reasonable confidence.

From the results, it was seen that as velocity increases, the pressures upstream and downstream get less negative. Also as velocity increases, the difference between the upstream and downstream pressure values increase showing that the pressure drop increases with velocity for all four meshes. Figure 5.5 shows the pressure drop variation with velocity for all the mesh pieces tested.

As with the CFD simulations involving single mesh sheets, the $\beta$ value of the tested meshes were calculated using equation 18. At the same velocity, the 500x0.025 mesh gave the maximum pressure drop value compared to the other

3. The lowest pressure drop and lowest gradient was for the mesh with highest $\beta$ value with 150x0.047 metal mesh and it was also the metal mesh size that gave the maximum upstream velocity when the inlet of the air-duct is fully open (11.75 m/s). The mesh with the highest pressure change gradient is the 500x0.025 and has the lowest $\beta$ value and this mesh size also gave the lowest upstream velocity value when the inlet of the duct is fully open (7.52 m/s). For a fixed velocity, the pressure drop increases with the decrease in the mesh free hole area, $\beta$. This is in agreement with the trend obtained by the CFD simulation results shown in figure 4.4 in chapter 4.

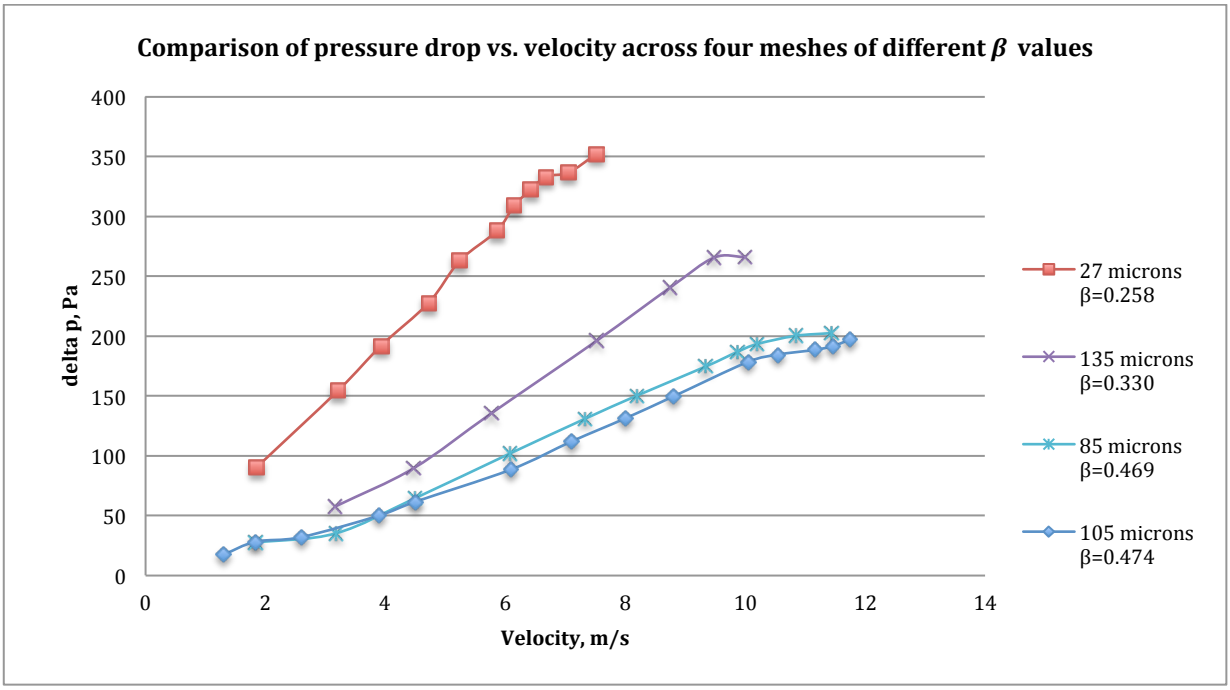


**Figure 5.5 comparing pressure vs. velocity graphs of four mesh sizes with beta values**

Figures 5.6 to 5.9 compare the CFD predicted pressure and experimental values for each of the mesh sheet sizes showing good agreement on both value and trend.

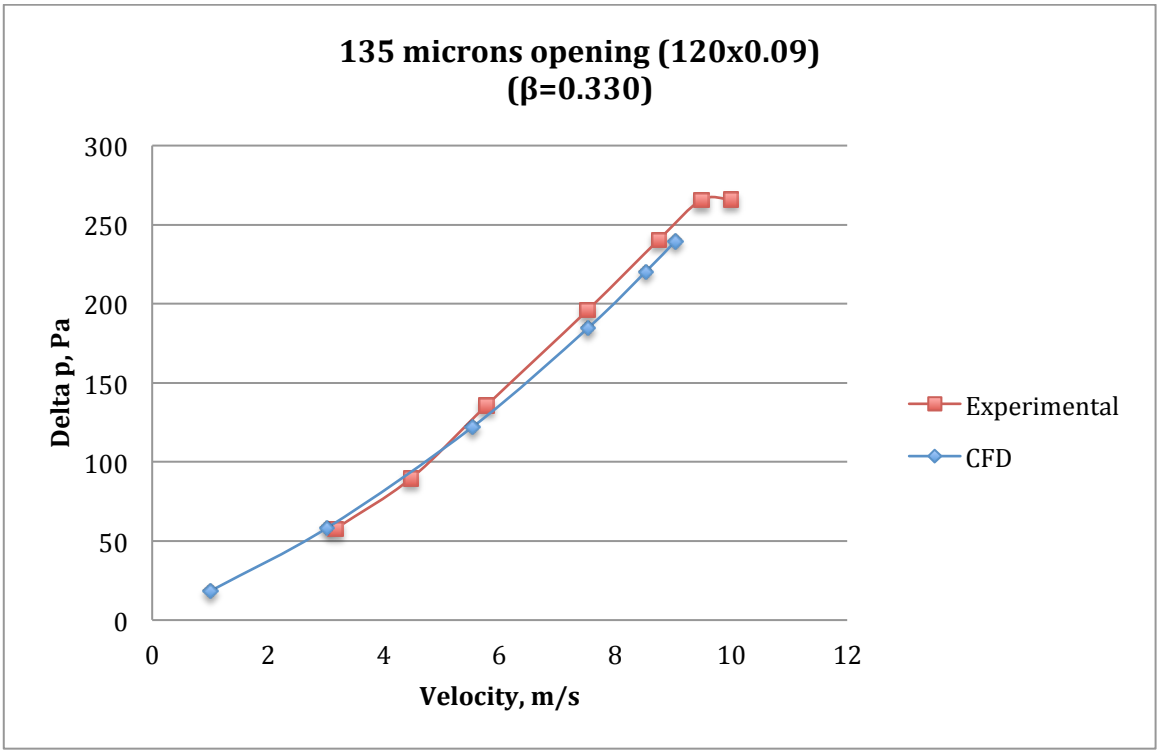


**Figure 5.6 comparison for experimental and CFD pressured drop across mesh 120x0.09**

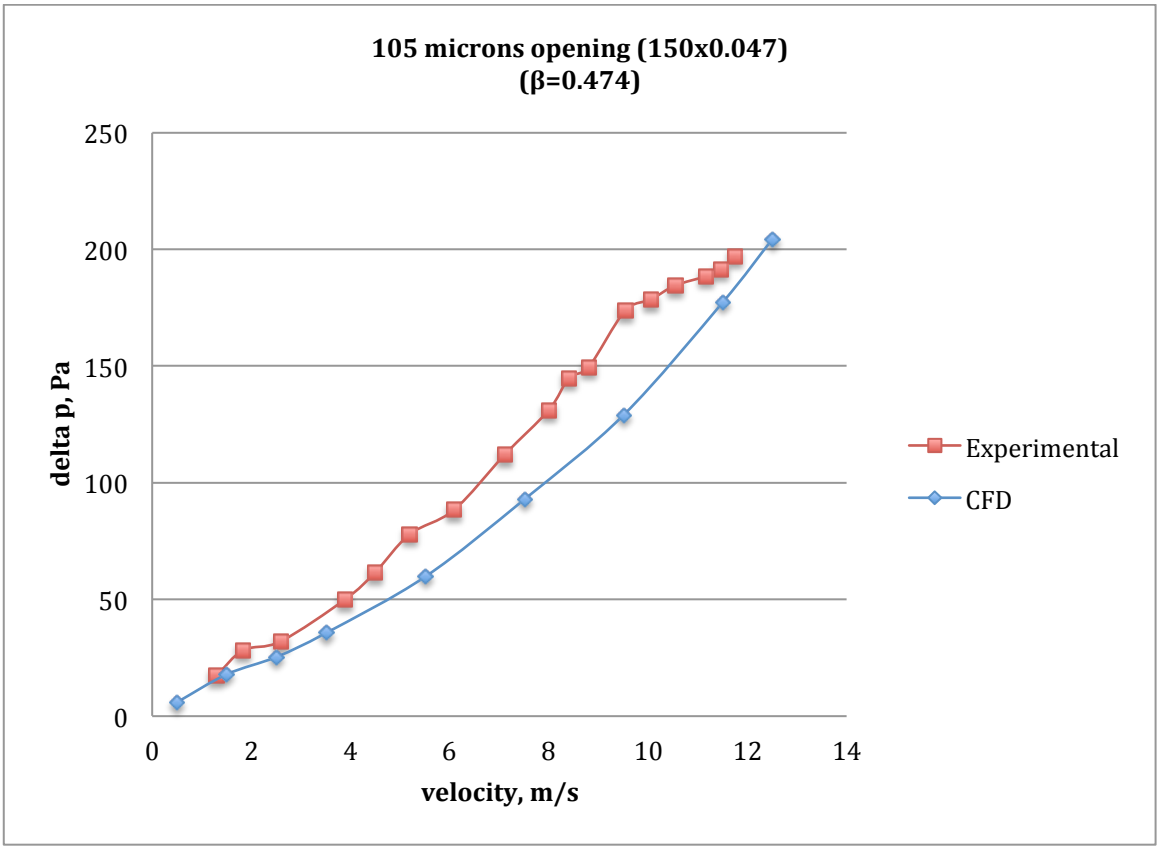


**Figure 5.7 comparison of experimental and CFD pressure drop across mesh 150x0.047**

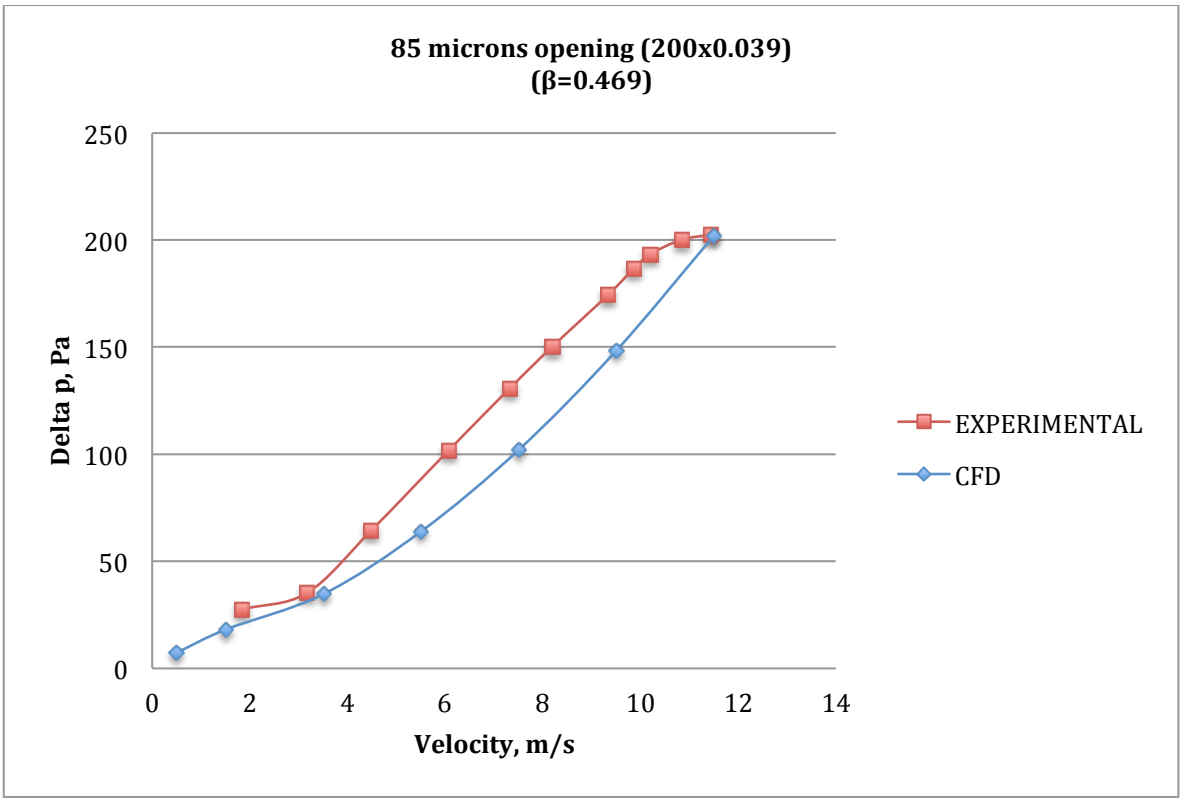


**Figure 5.8 comparison of experimental and CFD pressure drop across mesh 200x0.039**

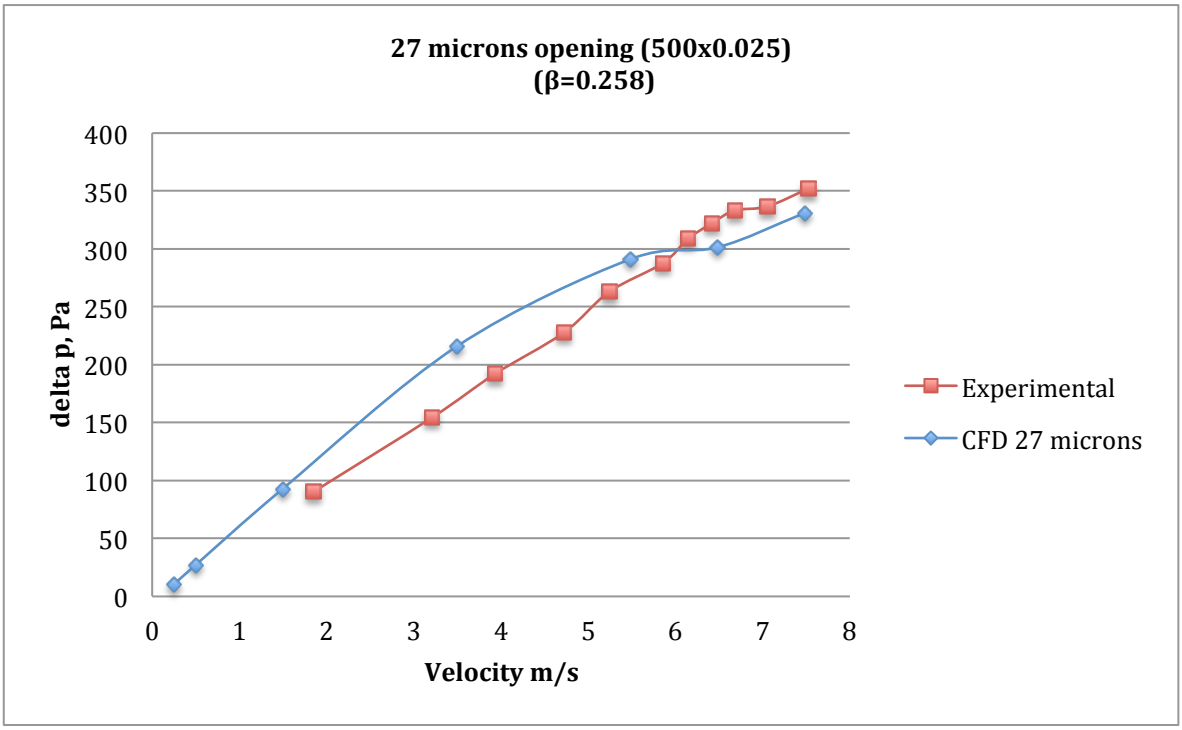


**Figure 5.9 comparison of experimental and CFD pressure drop across mesh 500x0.025**

Figure 5.10 shows the percentage error calculated from the pressure drops obtained from CFD predictions and experimental results. Percentage error was calculated as

$$Percentage\ experimental\ error = \frac{theoretical\ \Delta p - experimental\ \Delta p}{theoretical\ \Delta p} \times 100 \quad \text{(Eq. 34)}$$

where $\Delta p$ is the pressure drop or pressure difference between upstream and downstream. The errors seem to be mostly within $\times 20\%$ and the CFD can be considered to be in good agreement with experimental values.

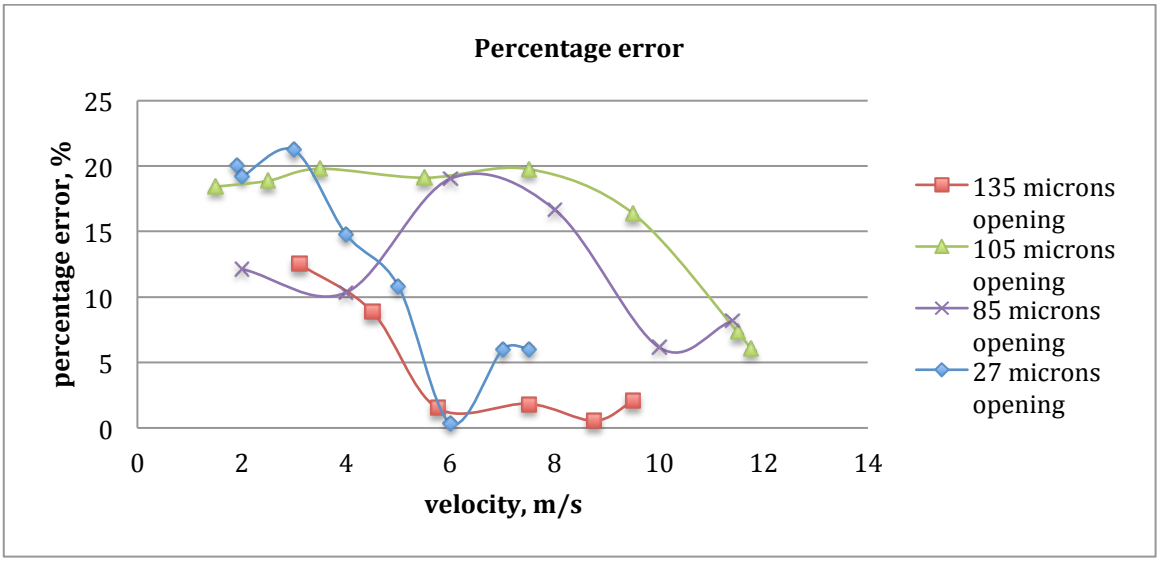


**Figure 5.10 experimental error values against velocity for the four mesh sheet sizes**

### *5.2 Experimental results for empty honeycomb experiment and CFD comparison*

The empty honeycomb test section fitted with mesh 150x0.04 as described in section 3.4 was tested twice where dynamic pressure were measured using an incline differential alcohol manometer and twice using a high accuracy differential pressure transducer. The pressure transducer has a range of ±12.45 Pa, therefore, it only measured a maximum of dynamic pressure of about 12.45 Pa when connected to the Pitot - static tube which corresponds to air velocity of less than 5m/s. The testing of the honeycomb structure packed with adsorbent granules was carried out using the differential alcohol manometer and a pressure transducer to enable measurement at a wide range of velocity. Results shown in figure 5.11 demonstrate the repeatability of the experiment as the lines are very close to each other even when using different measurement devices.

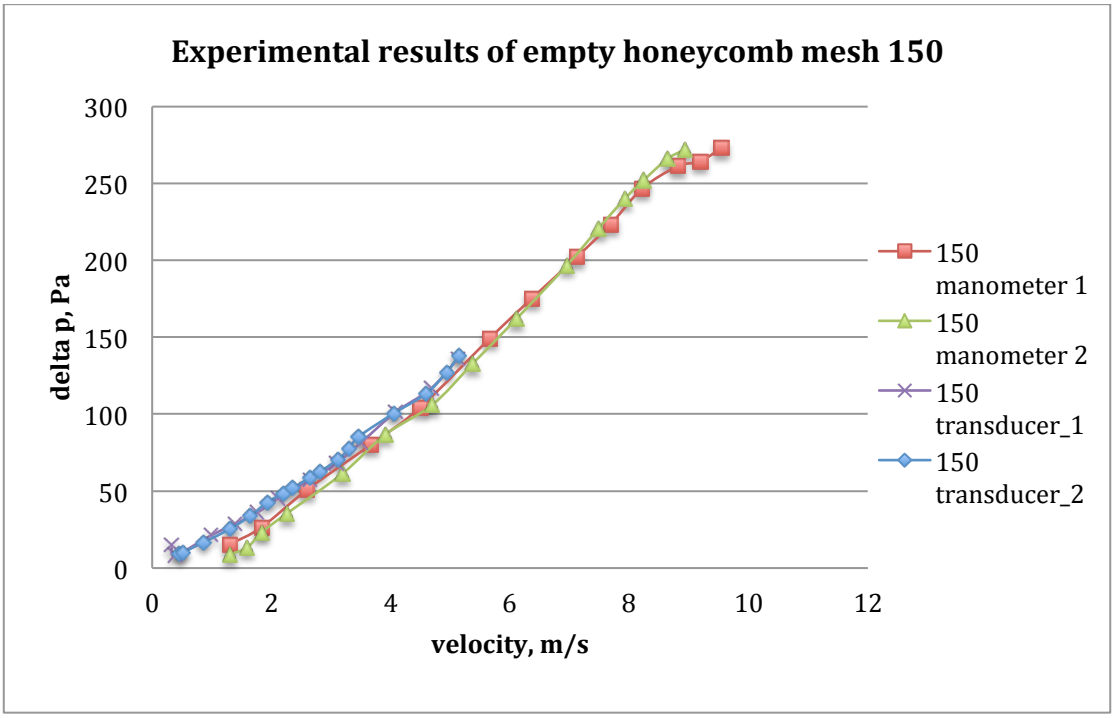


**Figure 5.11 experimental values of pressure drop caused by mesh 150x0.047**

For the empty honeycomb with mesh 500x0.025, figure 5.12 shows that three of the result sets overlapped each other and only the first manometer test gave results that were different to the average. Therefore it can be concluded that this experiment is also repeatable and gave stable results. From figure 5.12, it can seen that for a flow velocity of 5 m/s, a pressure drop of 440 Pa was caused by the two mesh sheets and empty honeycomb. For lower velocities, there is no clear trend for pressure drop as error grows but the average value is about 100 Pa for 1 m/s velocity.

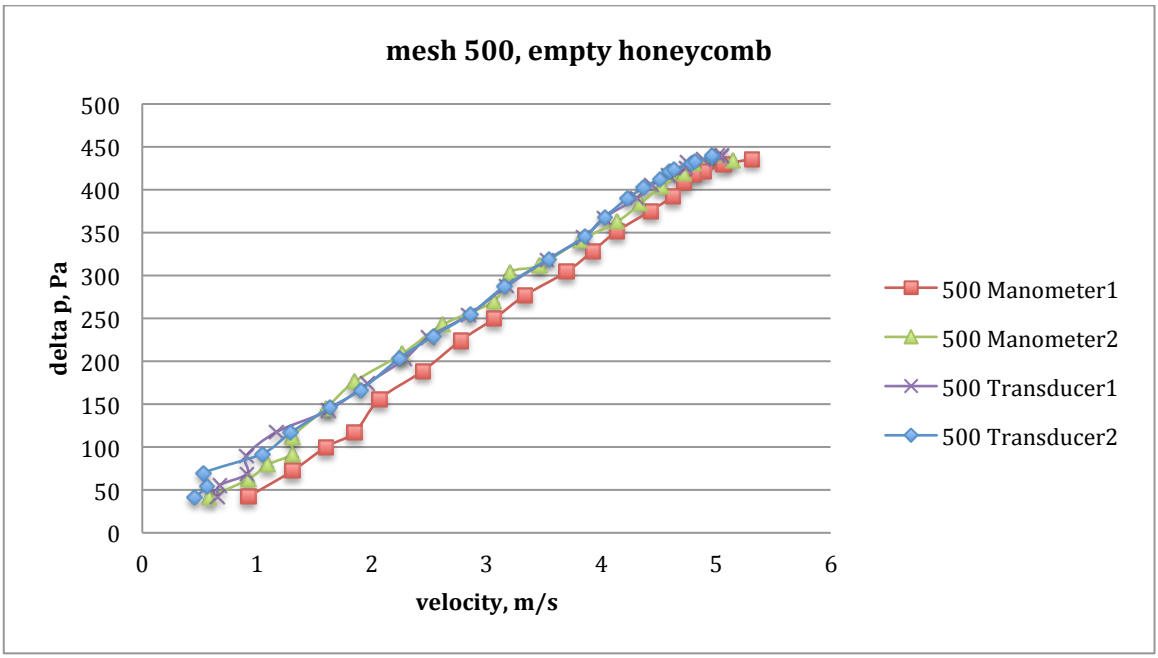


**Figure 5.12 pressure drop for four experimental test sets for empty honeycomb with mesh 500x0.025**

Figure 5.13 compares the experimental results to those predicted by the CFD simulation. It can be seen that the CFD simulation gave a pressure drop ranging from 9 to 112 Pa for the pressure drop caused by the honeycomb sandwiched by two meshes of 150x0.047 with 105 microns opening. The results of the CFD gave a graph line that was very near to the experimental results and error calculations, showed that percentage error was calculated to be within a range of between +5% at lower velocities and -20% at higher velocities as shown in figure 5.14.

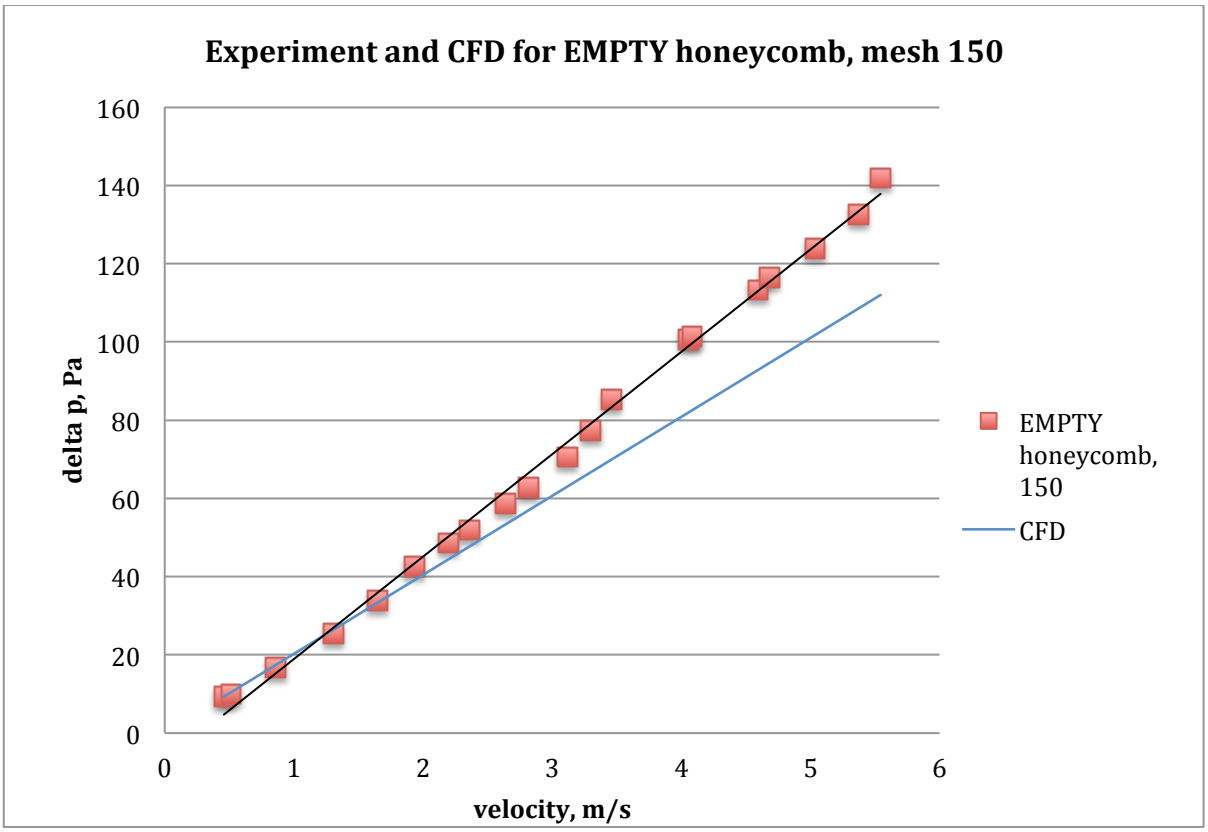


**Figure 5.13 Results for experimental and CFD study on empty honeycomb with mesh 150x0.047**

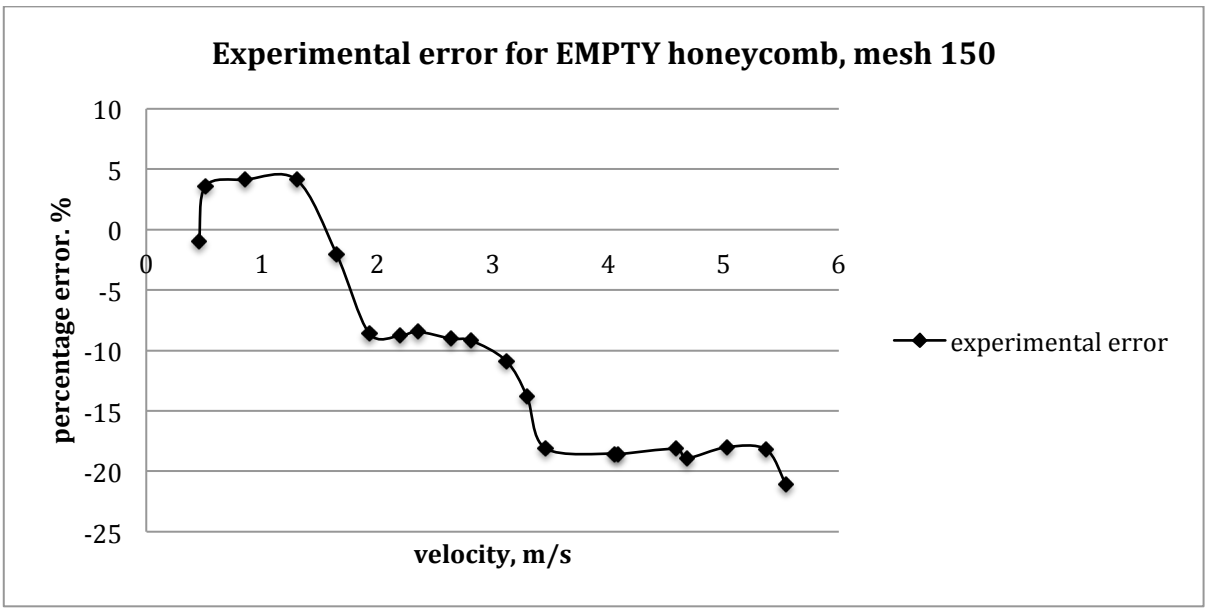


**Figure 5.14 percentage error between experiment and CFD for empty honeycomb fitted with mesh 150x0.047**

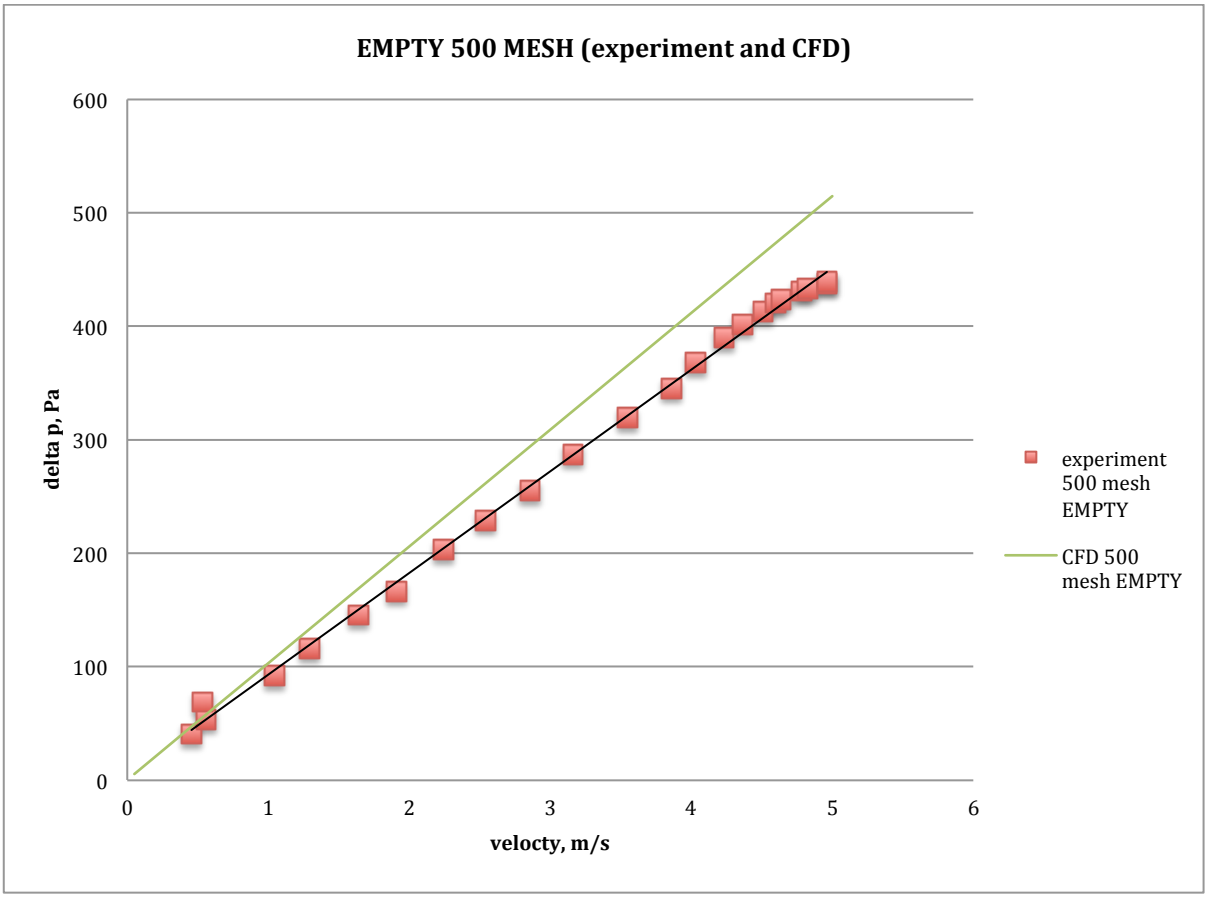


**Figure 5.15 experimental pressure drop with velocity caused by empty honeycomb with mesh 500x0.025 and CFD predicted values**

Figure 5.15 compares the experimental results for outflow velocities of range of 0.05-5m/s for the empty honeycomb with mesh 500 with the CFD predicted results. The best fit line of the CFD results can be seen in figure 5.15 to be quite close to the line of best fit of the experimental results. The CFD result line has slightly higher gradient than the experimental results line of best fit. For the empty honeycomb, the CFD predicted maximum pressure drop is 515 Pa compared to the experiment where the maximum is 438 Pa. Both pressure drops were caused by airflow at velocity of 5 m/s.

The percentage error was calculated from the series of experimental and CFD results and plotted against velocity in figure 5.16. There were anomalous data points that had an error of -20.6% which was caused by the second data point in the experimental result set, seen to be above the CFD results line, as well as the third data point with 6.6%. Other than this particular point, the rest of the

experimental results gave an error of less than 20% with a +17.8% maximum error and reaching down to a minimum of +6.6% error.

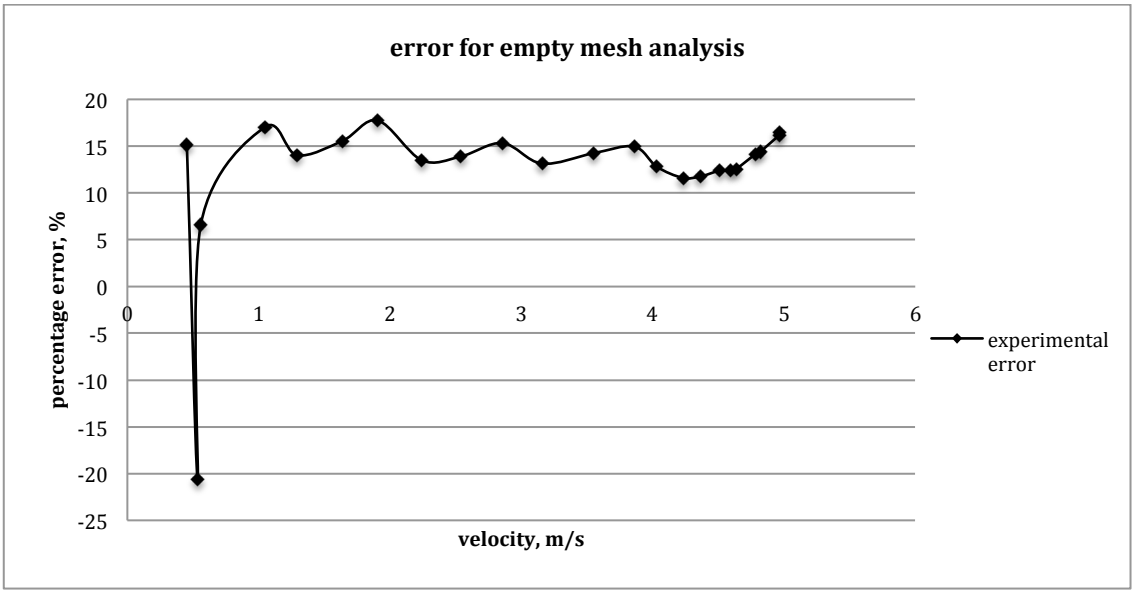


**Figure 5.16 precentage error between experimental and CFD values for empty mesh pressure drops**

### *5.3 Experimental results for filled honeycomb experiment and CFD comparison*

The honeycomb packed with granules was tested twice where pressure readings were taken using the differential pressure transducer. Only the transducer was used in the packed honeycomb because the maximum dynamic pressure that was achieved by the flow in the air duct was very low which was measured by the Pitot-static tube to be 4.48 Pa, indicative of a flow of 2.74 m/s. Therefore very small changes in dynamic pressure need to be detected by the transducer, which cannot be done using the manometer.

Figure 5.17 compares the pressure drop across filled honeycomb with mesh 150, using the inclined alcohol manometer (*filled exp #1*) and pressure transducer (*filled exp #2, filled exp #3*), highlighting the repeatability of measurement. However, the pressure transducer allowed measurement at velocity as low as 0.5 m/s compared to the 1.2 m/s obtained by the manometer.

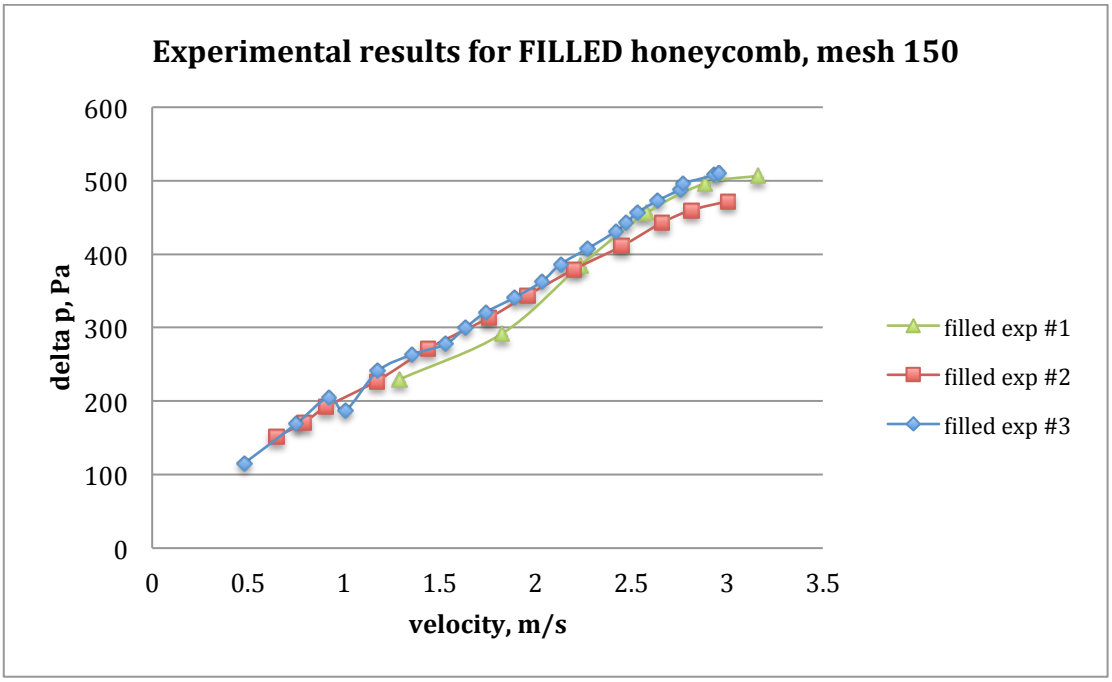


**Figure 5.17 showing three experimental test sets**

As with the empty honeycomb experiment, the CFD model of this set up was also made to simulate of airflow across the honeycomb packed with granules to

predict pressure drop across the unit. The values of K used for porous media were first of the capsular cylinder of diameter 2mm and 10 mm length and then the K value for 5 rows of 2 mm diameter spheres. The results of the CFD modelled from the packed honeycomb show that the CFD simulation that uses the K value of the capsular granules gave results nearer to the experimental value compared to the spherical granule K value as shown in figure 5.18.

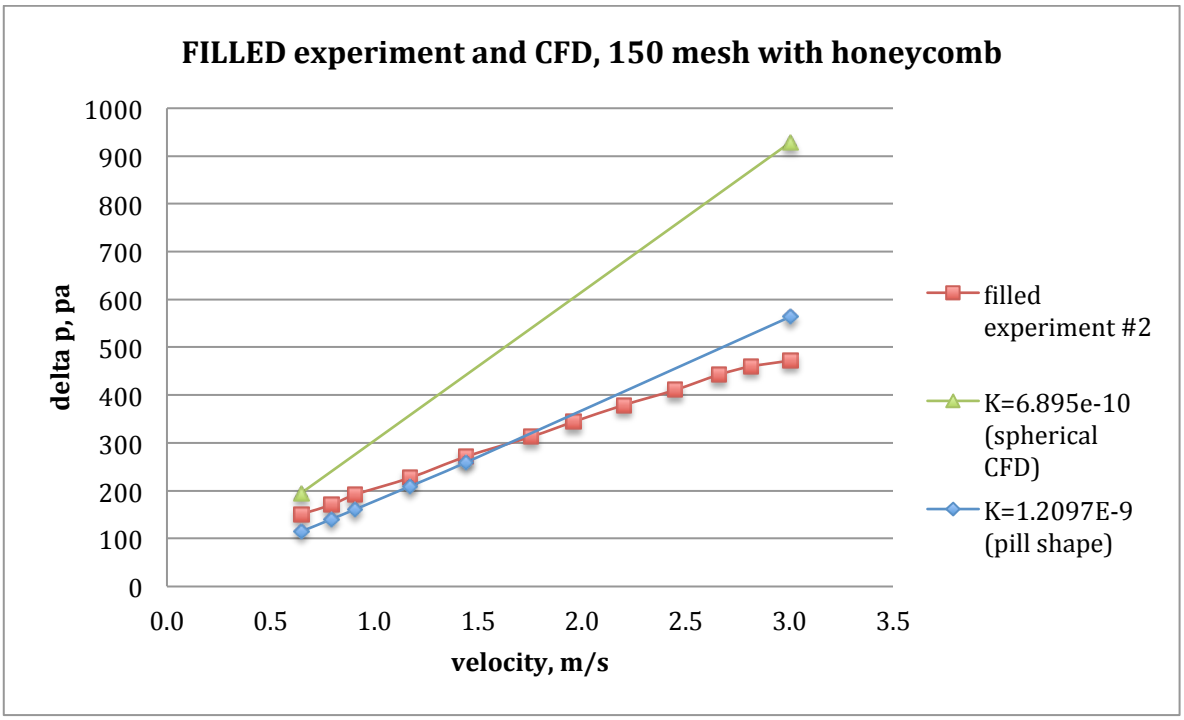


**Figure 5.18 CFD results using different K values of spherical and capsular modelling**

Subsequently, the CFD with capsule K value was used and compared to the experimental result values (Figure 5.19, Figure 5.20), especially experiments using the pressure transducer. The percentage errors were also calculated for the two experiments.

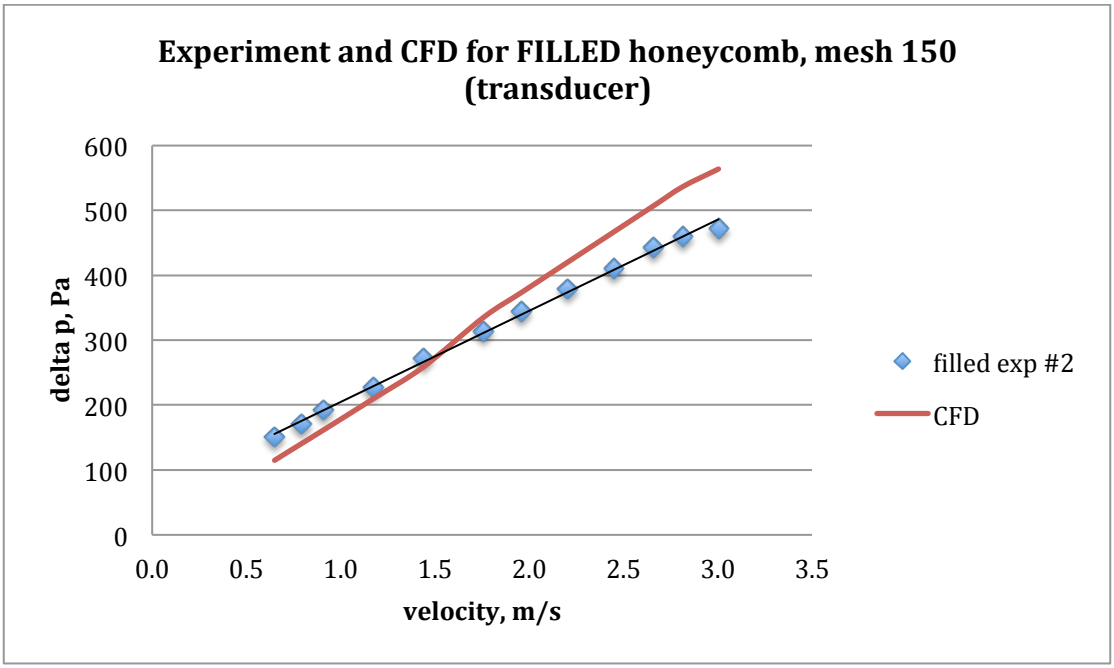


**Figure 5.19 Experimental set #2 and CFD pressure drop values measured with transducer for filled honeycomb**

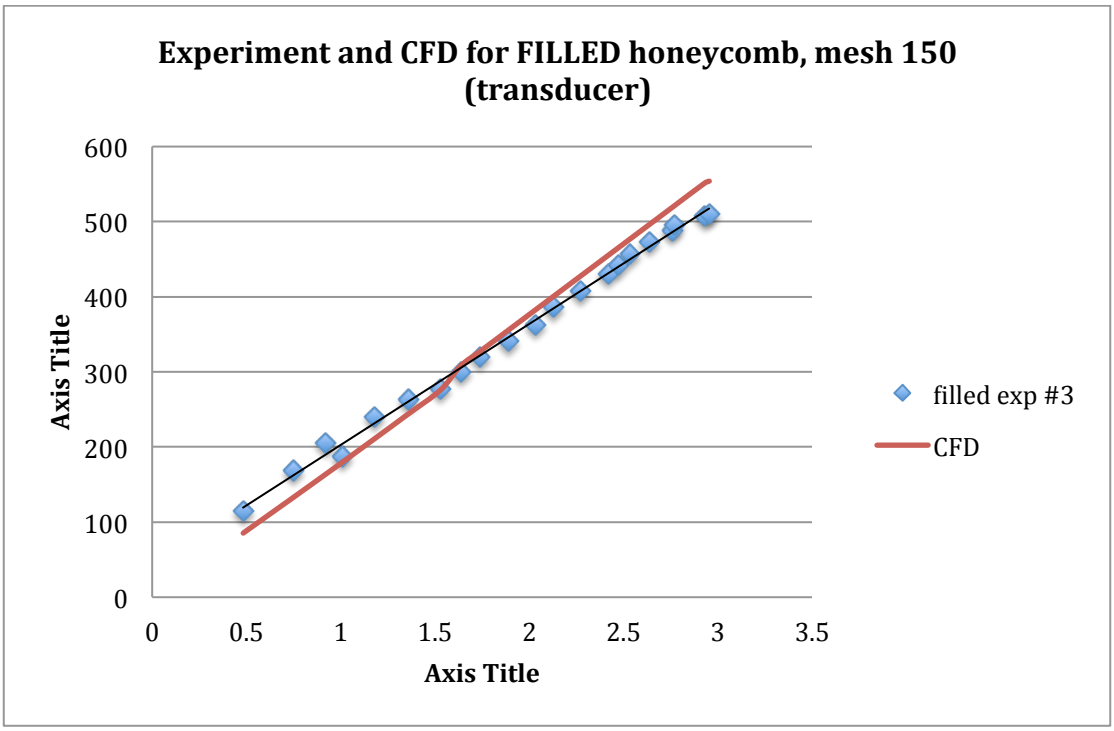


**Figure 5.20 Experimental set #3 and CFD pressuredrop values measured with transducer for filled honeycomb**

Figures 5.21 and 5.22 show the experimental error for both experiments when compared to the CFD with K=1.2097e-9 for the porous material filling the volume of the honeycomb cells. Most of the experimental data points have errors

within $\pm$ 20%, therefore it can be said with reasonable confidence that the CFD method is successful and can be used in modeling air flow in a representative section of adsorber bed comprising honeycomb cells packed with granular adsorbent. The results of the third experiment's error only reached up to +10% at higher velocities.

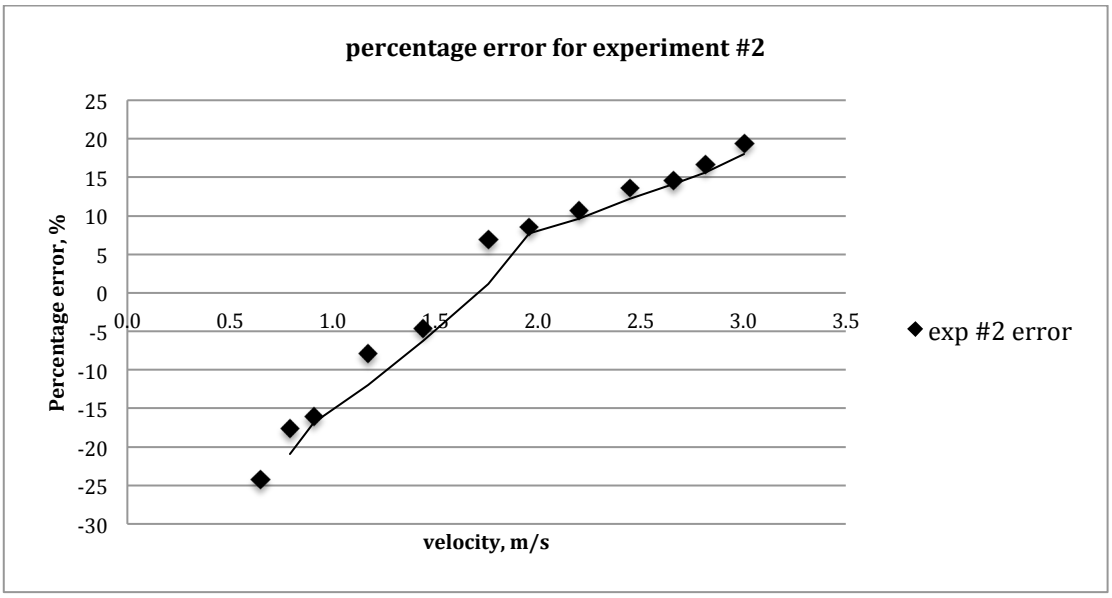


**Figure 5.21 percentage error for filled test set #2 (first transducer measurements)**

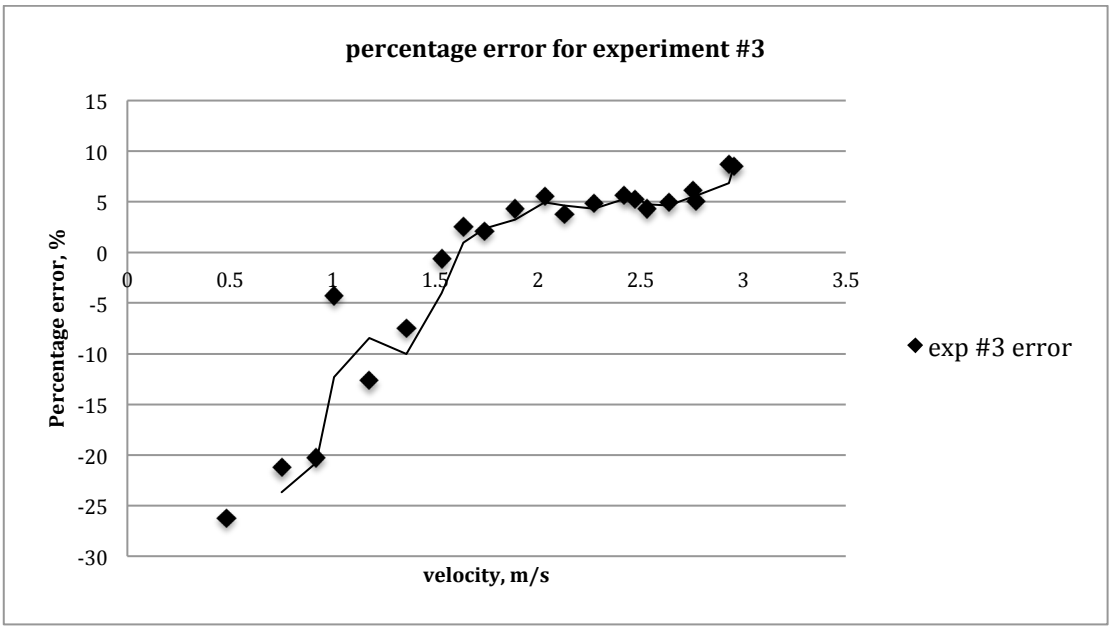


**Figure 5.22 percentage error for filled test set #3 (second transducer measurements)**

Figure 5.23 shows the pressure drop results obtained from two experiments with the honeycomb filled with granules held by mesh 500x0.025. As predicted, the pressure drop caused by the honeycomb packed with granules was much higher than the empty honeycomb, shown in figure 5.24. At about 2.5 m/s, a pressure drop of 500 Pa was produced. The pressure drop gradient for the packed honeycomb was twice that of the gradient for the empty honeycomb.

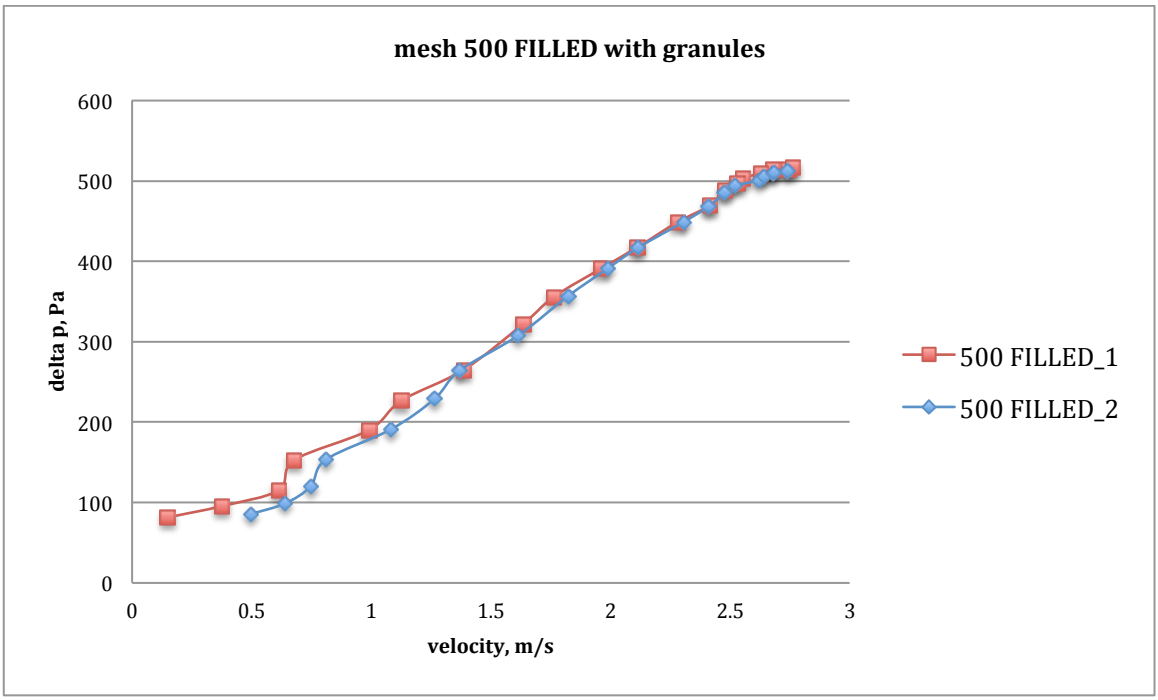


**Figure 5.23 pressure drop for two experimental test sets for filled honeycomb with 500x0.025 mesh**

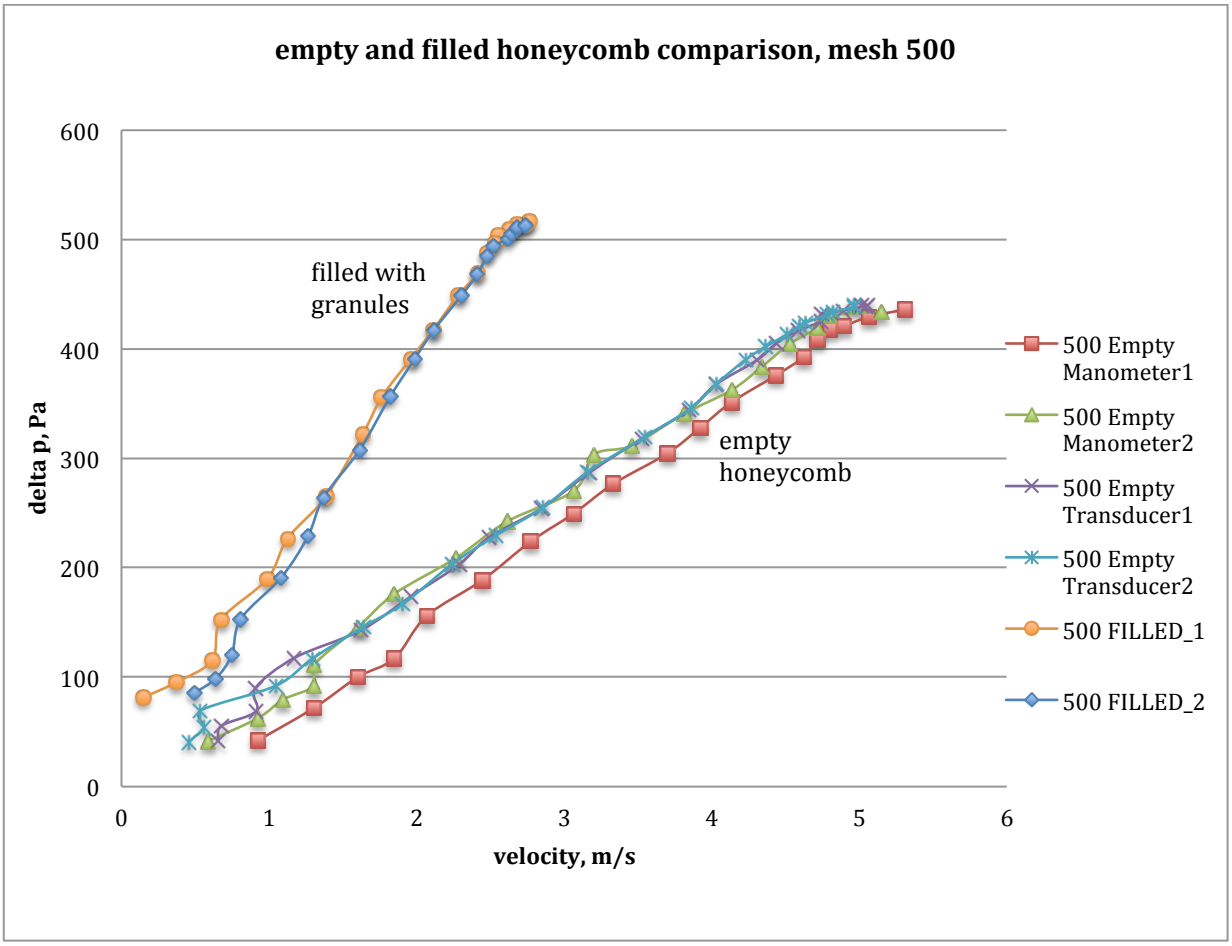


**Figure 5.24 pressure drop comparison for empty and filled honeycomb**

The CFD studies were done for outflow velocity range of 0.05 to 2.74 m/s for the filled honeycomb with mesh 500 and results were compared to the experimental results in figure 5.25. The maximum pressure drop recorded from the experiment was 523 Pa at 5 m/s, and for the CFD study, the maximum pressure drop was 605 Pa.

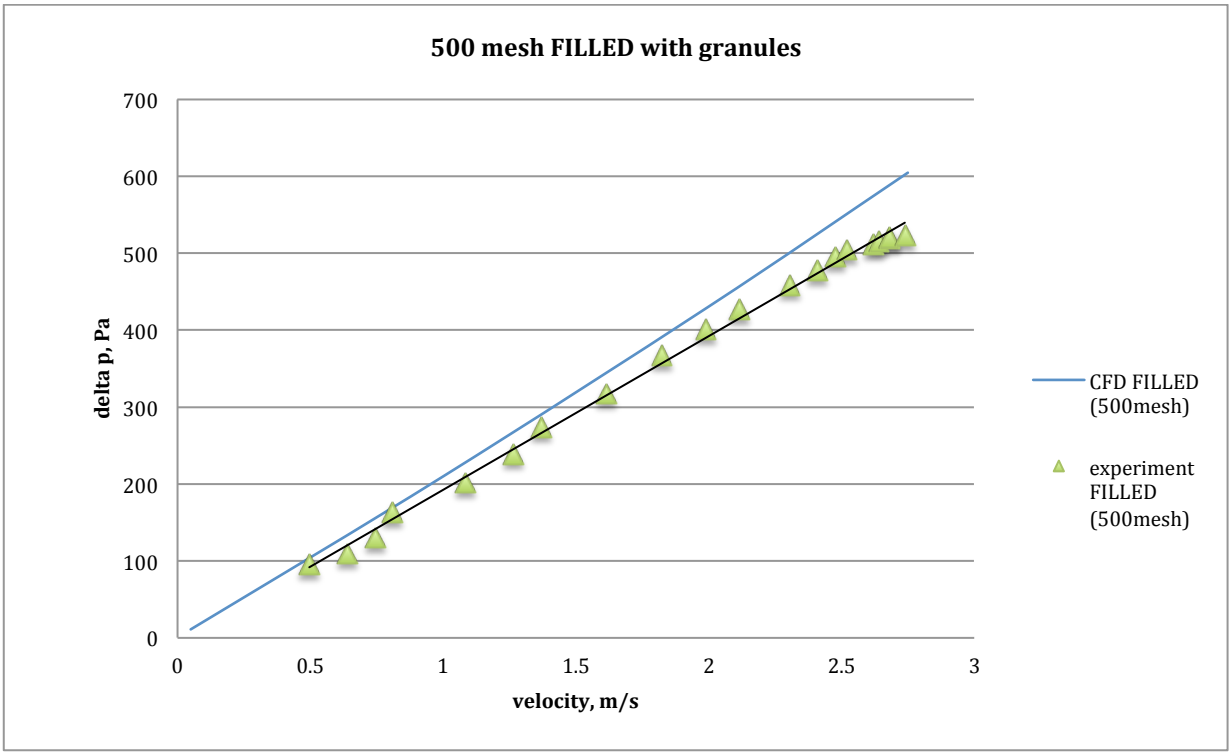


**Figure 5.25 experimental pressuyre drop with velocity caused by honeycomb filled with granules and CFD predicted values**

The percentage error calculated and plotted against velocity as shown in Figure 5.26 with the larger errors occurred at the lower velocities. As the velocity increased, the percentage error decreased and stabilized at about +10% error. Additionally, 17 out of 20 data points are below 15% error. The higher error at lower velocities may be caused by the measuring device. Even though the transducer is a high accuracy one, the very small changes in pressure nearer to the lower velocities can be difficult to detect especially since the pressure fluctuates during the experiment and the pressure that is used for the graphical analysis is of the mean pressures taken over 60 seconds where the datalogger records a value every 2 seconds.

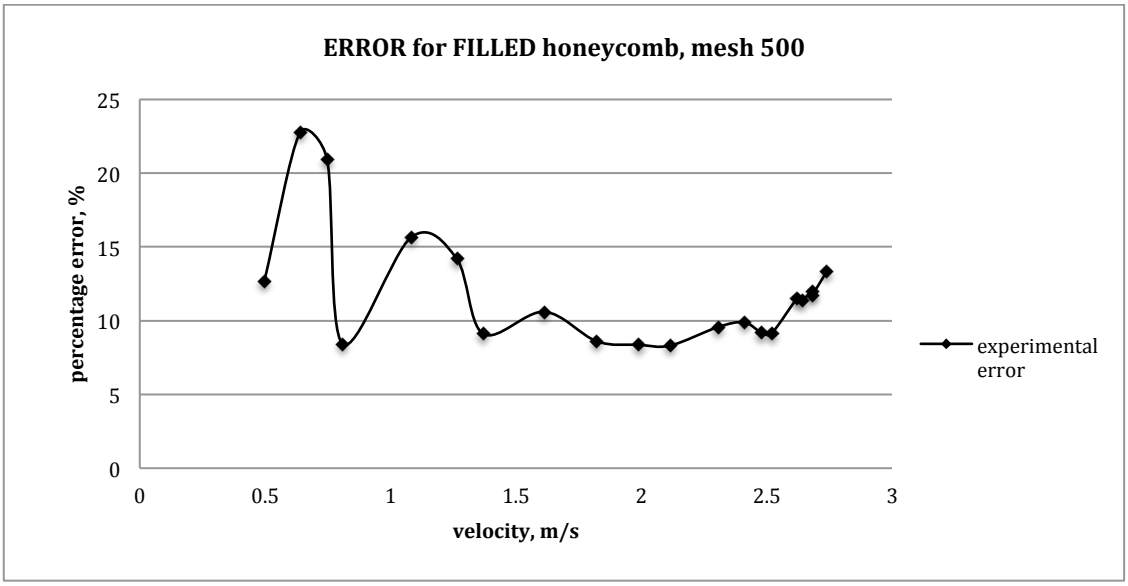


**Figure 5.26 percentage error from CFD and experimental results for honeycomb filled with granules**

### *5.4 Summary*

Simulating the granules as capsular cylinder showed CFD predicted pressure drop similar to experimental results. The pressure drop is mainly caused by the packed granules and in the case of designing an adsorption bed containing the fine material, CFD modeling would have to focus on the pressure drop effect of the adsorption material and the air flow characteristics around the fine granules.

# *Chapter 6* Conclusion

Recently, there has been significant progress in the development of advanced adsorbent material with superior adsorption capabilities but this exist in fine granules that require fine mesh to contain in adsorption beds. In this research, both experimental and computational fluid dynamic analyses are used to assess flow in adsorption bed structures consisting of porous adsorbent material packed in honeycomb cells and bound by mesh sheets. From this study several conclusions can be made:

1. For all the experimental and CFD set-ups, the pressure drop increases as the velocity is increased. The set ups include the single mesh sheet, the 10mm thick honeycomb sandwiched between two mesh sheets empty and the honeycomb filled with adsorption material granules and then sandwiched between two mesh sheets. Predictably, the honeycomb unit filled with granules caused the highest degree of pressure drop, then the empty honeycomb between two mesh sheets, the single mesh sheets and lastly the 10mm honeycomb tested on its own within the air flow duct which caused very small air pressure losses.

2. When the single mesh sheet results were compared for the four sizes, it can be seen that the highest pressure drop was caused by the mesh sheet that had the lowest porosity $\epsilon$ also known as the void fraction or the free hole area $\beta$. Since the pressure drop across a material is caused by the degree of obstruction to flow that causes form drag and friction losses, it can also be concluded to be inversely related to the permeability of a material to fluid flow which is the degree of flow allowed through the open spaces. The material with the lower porosity causes higher pressure losses therefore have lower permeability. Therefore it can be concluded that the porosity is proportional to the permeability of a material such as the mesh layers used in the study and the granule-filled honeycombs.

3. Although there has been studies involving the use of porous media physics to model a single free standing mesh, to the author's knowledge, no CFD study has been conducted that used the porous media method to model different materials next to each other using porous media physics such as in this project where the mesh screen layer has been modeled next to the packed granules and then another mesh layer all modeled as porous media with different user-defined porosity and permeability values corresponding to its material. Using this porous material method also means that for studies of adsorbent beds that uses mesh screens for securing the adsorbent material, additional CFD physics modules such as heat transfer and multi-phase flow can be added to the model without as much strain on the simulation solver compared to when using actual 3D geometry of the mesh wires. This CFD method can be used to save time and computing power.

4. The study has shown that the CFD method employing porous media modeling can be used as an acceptable method for predicting the pressure drop across meshes and granules with a $\pm$ 20% error from experimental results. The stages of CFD method includes: (1) modeling the air duct mesh sheet as 2 dimensional geometry to find the permeability of the mesh sheet, (2) modeling the granules as capsules with the same diameter as the granules arranged in a 3-D air duct geometry, to find the permeability for the granules.

5. Using the capsular solid geometry to predict the pressure drop with CFD and consequently calculating the permeability of granules has shown very promising results when compared to experimental results. This can be used as a time-saving alternative to experimental techniques to predict pressure drop across small granular structures and can even better predict the pressure and flow characteristics compared to the time consuming CFD study with repeated spherical structures. Also, the study has shown that modeling flow across microstructures whether it be spherical or capsular can be done for a small hexagonal configuration of seven granules arranged adjacent to each other and and by just using symmetry would have given the same pressure and flow results as when simulating flow across a larger cross sectional area with more

granules. Although only one size of granules have been tested for in this study, and its CFD model has been validated, it can be reasonably concluded that this validated CFD can be used to predict the performance for other sizes.

The technique developed in this study highlights the benefits of using this approach to predict the pressure losses in future bed designs, especially systems with complex and multiple components.

There are various recommendations to further improve this piece of research through improvements to the experimental set up as well as to testing procedures on the mesh and honeycomb set-up.

1. The first potential cause of inaccuracy may lie in the use of the pre-existing air duct that has a fixed velocity outlet fan and also using the method of partially blocking the inlet area to vary the air velocity within the duct. An improvement may be by using compressed gas from a cylinder to create a controlled and constant airflow within the duct that can be easily monitored using the cylinder's pressure gauge at the inlet. Using compressed gas may give a more stable airflow at low velocities such as 1 m/s and below. In the experiment, the inlet partial blocking method has caused observable fluctuations in pressure and velocity at low pressures from 1 m/s and below as the inlet is blocked more and more.

2. Also in the study, only the velocity of air flow upstream of the mesh or honeycomb set up were monitored and recorded using the pitot-static tube connected to the differential pressure transducer. Even though the CFD simulations all gave results that showed that upstream and downstream velocity are constant at steady state, the air velocity within the duct should be monitored downstream as well as upstream in the experiment so that any potential velocity losses caused by the adsorption bed unit can be recorded. The upstream and downstream pressure can be recorded by installing windmill or propeller anemometers that can

measure the overall air speed across a cross-section of the air duct rather than one point within the duct as measured by a pitot-static tube.

3. Another potential cause of error may lie with the way that the granule-filled honeycomb structure was built where the mesh sheets were glued onto the honeycomb using heated glue from glue gun that may cause added interruptions of airflow within the adsorbent-honeycomb structure that was caused by strips of solidified glue within the honeycomb. Another method of mesh sheet to honeycomb adhesion was tried using liquid silicone. However, the mesh easily pulled away from the honeycomb as the granules were packed into it, which cause the granules to drop out of the honeycomb and collect at the bottom causing uneven placement of adsorbent material. Therefore the heated glue was used to secure the meshes onto the honeycomb.

4. As can be seen from the results graph and percentage error analysis, the lower velocity data points are inconsistent of the trendlines and it can be concluded that even though a high accuracy differential manometer was used for the experiment, there was a slight amount of error but more than the high velocity data points' errors. If compressed air was used to create flow within the duct, the fluctuations may potentially be reduced compared to the blocked inlet that caused pressure fluctuations when low velocities were used. Also an even more accurate pressure transducer can be used to measure and record the pressure reading of the points along the air duct at low velocities, such as a membrane or thin film pressure transducer.

5. In the experiment, the different mesh sheets were not measured experimentally for porosity in terms of volume. The value was calculated from the data provided by the supplier and the effective pore diameter and wire diameters were measured using the microscope but the void fraction was calculated as a two-dimensional ratio. The void fraction was not measured experimentally in terms of its three-dimensional structure and is not a ratio of volumes as most void fractions are normally derived.

One way to measure void fraction of a sheet of mesh is by submerging it in water to measure the displaced volume of fluid to get the absolute volume of the mesh wires. Then the thickness of the mesh can be measured at multiple points on the mesh sheet using a micrometer and this value can the be multiplied by the area of the submerged mesh sheet to find the volume of the mesh including the openings. Then the difference between the two volumes can be said to be the volume taken up by the void or openings of the mesh sheet and this value can be used to calculate the void fraction or porosity. Unfortunately, the void fraction of the granules are difficult to measure experimentally because the granule materials cannot be submerged in water as it is highly adsorptive and its high performance qualities means that the granules take up and hold onto the water and potentially could change in size and volume. So this method would not work for finding the volume of the granules.

6. Most adsorption systems are designed as closed systems and in this study, the pressure drop has been studied experimentally and by CFD using open system models. Due to the time constrains of only 12 months, the research had to be conducted by modifying a pre-existing open air flow experimental set-up. For further work, it is recommended that a study on pressure drop across closed system adsorber design should be conducted and validated using similar CFD methods as in this research work.

**REFERENCES**


[1] Pérez-Lombard L, Adnot J, Ortiz J A, Rivière P. *HVAC systems energy comparisons for an office building*. Proceedings of Climamed Lisbon, 2004.

[2] International Energy Agency, *World Energy Outlook 2012.* OECD/IEA, 2012

[3] Wachowski, L*, Ecological Replacements of Ozone-Depleting Substances*. Polish Journal of Environmental Studies 2001 vol. 10, issue 6, p 417

[4] Grubb M., *The Economics of the Kyoto Protocol*, World Economics 4 (3) July 2003

[5] Rezk ARM, *Theoretical and experimental investigation of silica gel/water adsorption refrigeration systems.* University of Birmingham, July 2012

[6] Shelton, S.V., William, J. Wepfer and Miles, D.J., Square wave analysis of the solid-vapor adsorption heat pump. *Heat Recovery Systems & CHP,* 1989.9 : p. 233-247

[7] Hamamoto, Y., Alam, K.C.A., Saha, B.B., Koyama, S., Akisawa, A., Kashiwagi, T., Study on adsorption refrigeration cycle utilizing activated carbon fibers. Part 2. Cycle Performance evaluation. *International Journal of refrigeration*,2006. 29: p. 315-327.

[8] Saha BB, Akisawa A, Kashiwagi T. *Solar/waste heat driven two-stage adsorption chiller: the prototype.* Renew Energy (2001);23(1):93–101.

[9] Luo H L, Wang R Z, Dai Y J, Wu J Y, Shen J M, Zhang B B. *An efficient solar-powered adsorption chiller and its application in low-temperature grain storage.* Solar Energy 81 (2007) 607-613

[10] Abu Hamdeh N H, Al-Muhtaseb M A, *Optimization of solar adsorption refrigeration system using experimental and statistical techniques*. Energy Conversion and Management 51 (2010) 1610–1615

[11] Fadar A, Mimet A, Perez-Garcia M, *Modelling and performance study of a continuous adsorption refrigeration system driven by parabolic trough solar collector* Solar Energy 83 (2009) 850–861

[12] Zhai X Q. *Design and performance of a solar-powered air-conditioning system in a green building* Applied Energy 85 (2008b) 297–311

[13] Ferreira Leite A P. *Central air conditioning based on adsorption and solar*

*energy* Applied Thermal Engineering 31 (2011) 50-58

[14] Restuccia G, Freni A, Vasta S, Aristov Y. *Selective water sorbent for solid sorption chiller: experimental results and modelling.* Int J Refrig (2004); 27(3): 284–93.

[15] Clausse M, Alam K C A, Meunier F. *Residential air conditioning and heating by means of enhanced solar collectors coupled to an adsorption system.* Solar Energy 82 (2008) 885-892

[16] Habib K, Choudhury B, Chatterjee P K, Saha B B. *Study on solar heat driven dual-mode adsorption chiller*. Energy 63 (2013) 133-141

[17] Santori G, Sapienza A, Freni A. *A dynamic multi-level model for adsorptive solar cooling*. Renewable Energy 43 (2012), 301-312.

[18] Nunez T, Mittelbach W, Henning HM. *Development of an adsorption chiller and heat pump for domestic heating and air-conditioning applications*. Proceedings of the third international conference on heat powered cycles (HPC 2004).

[19] Alam K C A, Saha B B, Akisawa A. *Adsorption cooling driven by solar collector: A case study for Tokyo solar data*. Applied Thermal Engineering 50 (2013) 1603-1609

[20] Tchernev D I, *Solar air conditioning and refrigeration systems utilizing zeolites*. Proceedings of Intersociety Energy Convention, Eng Conf 1982; 2: 2070–3.

[21] Lu Z S. *Study of a novel solar adsorption cooling system and a solar absorption cooling system with new CPC collectors* Renewable Energy 50 (2013a) 299-306

[22] Lu Z S. *Performance improvement by mass-heat recovery of an innovative adsorption air-conditioner driven by 50-80C hot water* Applied Thermal Engineering 55 (2013b) 113-120

[23] Lu Z S, Wang R Z, Xia Z Z, Wu Q B, Sun Y M, Chen Z Y. *An analysis of the performance of a novel solar silica gel-water adsorption air-conditioning.* Applied Thermal Engineering 31 (2011) 3636-3642

[24] Lu Z S, Wang R Z, Xia Z Z. *Experimental analysis of an adsorption air-conditioning with microporous silica-gel-water*. Applied Thermal Engineeirng 50 (2013c) 1015-1020

[25] Buchter F, Dind P, Pons M. *An experimental solar-powered adsorptive refrigerator tested in Burkina-Faso*. International Journal of Refrigeration 26 (2003) 79-86

[26] Thomas S, Hennaut S, Maas S, Andre P. *Experimentation and simulation of a small-scale adsorption cooling system in temperate climate*. Energy Procedia 30 (2012) 704-714

[27] Hassan H Z, Mohamad A A, Bennacer R. *Simulation of an adsorption solar cooling system*. Energy 36 (2011) 530-537

[28] Hassan H Z, Mohamad A A. *Thermodynamic analysis and theoretical study of a continuous operation solar-powered adsorption refrigeration system*. Energy 61 (2013) 167-178

[29] Alghoul M A, Sulaiman M Y, Sopian K, Azmi B Z. *Performance of a dual-pupose solar continuous adsorption system*. Renewable Energy 34 (2009) 920-927

[30] Chekirou W, Chikouche A, Boukheit N, Karaali A, Phalippou S. *Dynamic modeling and simulation of the tubular adsorber of a solid adsorption machine powered by solar energy*. International Journal of Refrigeration (2003) 1-15

[31] Wang RZ. *Performance improvement of adsorption cooling by heat and mass recovery operation*. Int J Refrig (2001);24:602–11.

[32] Zhao H, Liang H, Sun W, Yu G, Cao D, Ji J. *Experimental study on solar cooling tube using thermal/vacuum emptying method.* Advances in Materials Science and Engineering Volume 2012 (2012) Article ID 808210

[33] Benelmir R, Merabtine A, Descieux D. *Energy tri-generation: combined gas cogeneration/solar cooling*. International Journal of Thermal &Environmental Engineering Volume 4, No. 2 (2012) 157-163

[34] Yang G Z, Xia Z Z, Wang R Z, Keletigui D. *Research on a compact adsorption room air conditioner.* Energy Conversion and Management 47 (2006) 2167-2177

[35] Ara Rouf R, Amanul Alam K C, Hakim Khan M A. *Effect of operating condition on the performance of adsorption solar cooling run by solar collectors*. Procedia Engineering 56 (2013) 607-612.

[36] Abdul Majeed A M, Suliman M Y, Sopian K. *Weather effect on the solar adsorption air conditioning system using activated carbon fiber/ethanol as pair of*

*refrigeration: a case study of Malaysia*. Research Journal of Applied Sciences, Engineering and Technology 7 (2014) 1069-1075

[37] Li C H, Wang R Z, Dai Y J. *Simulation and economic analysis of a solar powered adsorption refrigerator using an evacuated tube for thermal insulation.* Renewable Energy 28 (2003) 249-269

[38] Hossain A K, Thorpe R, Vasudean P, Sen P K, Critoph R E, Davies P A. *Omnigen: Providing electricity, food preparation, cold storage and pure water using a variety of local fuel*. Renewable Energy 49 (2013) 197-202

[39] Abu Hamdeh N H, Alnefaie K A, Almitani K H. *Design and performance characteristics of solar adsorption refrigeration system using parabolic trough collector: Experimental and statistical optimization technique.* Energy Conversion and Management 74 (2013) 162-170

[40] Kalogirou A, *The potential of solar industrial process heat applications.* Applied Energy Volume 76, Issue 4, December 2003, Pages 337–361

[41] Zhai X Q, Wang R Z. *Experiences on solar heating and cooling in China.* Renewable and Sustainable Energy Reviews 12 (2008a) 1110-1128

[42] Li Yang, Sumathy K. *Technology development in the solar adsorption refrigeration systems* Progress in Energy and Combustion Science 29 (2004) 301–327

[43] Henning H M. *Solar assisted air-conditioning of buildings – an overview*. Applied Thermal Engineering 27 (2007) 1734-1749

[44] Afshar O, Saidur R, Hassanuzzaman M, Jameel M. *A review of thermodynamics and heat transfer in solar refrigeration systems.* Renewable and Sustainable Energy Reviews 16 (2012) 5639-5648

[45] Sumathy K, Li Z F. *A solar powered ice maker with the solid adsorption pair of activated carbon and methanol*. International Journal of Energy Research (1999); 23: 517–27.

[46] Wang D C, Zhang J P. *Design and performance prediction of an adsorption heat pump with multi-cooling tubes.* Energy Conversion and Management 50 (2009) 1157-1162

[47] Arnoldsson, J., *Adsorption chillers,uptake of Ethanol on Type RD Silica gel.* Linköping University, The Institute of Technology, 2012.

[48] Królicki, Z., Wilk, T., Zajączkowski, B., Kaczmarczyk, J*., Research on adsorption characteristics of active carbon and silica gel and application in solar refrigeration and heat pump.*61st ATI National Congress (International Session) "Solar Heating and Cooling", 2006.

[49] Rezk, A., Elsayed, A., Mahamoud, S., Al-dadah, R., *Adsorption refrigeration. Chapter published in Advances in Engineering research*. 8.Nova published

[50] Abdullah, M.O., Tan, I.A.W., Limb and L.S., *Automobile adsorption air-conditioning system using oil palm biomass-based activated carbon: A review.* Renewable and Sustainable Energy Reviews. 2011. 15 (4): p. 2061–2072.

[51] Fang, Q.-R., Makal, T.A., Young, M.D., Hong-Cai Zhou. *Recent advances in the study of mesoporous metalorganic frameworks*. Comments on Inorganic Chemistry, 2010. 31: p. 5, 165 – 195.

[52] Henninger, S K, Habib, H A, Janiak, C, *MOFs as Adsorbents for Low Temperature Heating and Cooling Applications.* Journal of the American Chemical Society, 2009: 2776-277

[53] Chen H, Cui Q Wu J, Zhu Y et al. *Hydrothermal stability of SAPO-34 for refrigeration and air conditioning applications*. Materials Research Bulletin 52 (2014) 82-88

[54] Zheng, X. , Ge, T.S., Wang, R.Z., *Recent progress on desiccant materials for solid desiccant cooling systems.* Energy 2014: p. 1-15.

[55] Al-Dadah R K. *Compact High Energy Density Adsorption Heat Storage System Using Metal Organic Framework Materials- Prototype Development.* Presentation for the Department of Energy and Climate Change (2014). University of Birmingham

[56] Armour, J.C., Cannon, J.N. *Fluid flow through woven screens* AIChE J (1968) 14 (3) 415-420

[57] Miguel A F (1998). *Airflow through porous screens: from theory to practical considerations.* Energy and Buildings, 28(2), 63–69.

[58] Miguel A F; van de Braak N J; Bot G P A (1997). *Analysis of the airflow characteristics of greenhouse screening materials.* Journal of Agricultural Engineering Research, 67, 105–112.

[59] Teitel M (2009) *Using computational fluid dynamics simulations to determine pressure drops on woven screens*. Biosystems Engineering 105 (2010)

172–179

[60] Kouhikamali R., S.M.A. Noori Rahim Abadi, M. Hassani. *Numerical study of performance of wire mesh mist eliminator*. Applied Thermal Engineering 67 (2014) 214-222

[61] Zivkovic V, Zerna P, Alwahabi Z.T., Biggs M.J.. *A pressure drop correlation for low Reynolds number Newtonian flows through a rectangular orifice in a similarly shaped micro-channel.* Chemical Engineering Research and Design 91 (2013) 1–6

[62] Maddocks, J.R., Van Sciver, S.W. *Pressure drop and He II flow through fine mesh screens.* Space Cryogenics Workshop, Italy. 18-19 July 1988. Butterworth & Co (Publishers) Ltd

[63] Glaznev, I., Ponomarenko, I., Kirik, S., Aristov, Y., *Composites CaCl2/SBA-15 for adsorptive transformation of low temperature heat: Pore size effect*. International journal of refrigeration 2011, 34: p. 1244-1250.

[64] Scott G D, Kilgour D M. *The density of random close packing of spheres.* British Journal of Applied Physics 2 (1969) 863-866

[65] McGeary R K. *Mechanical Packing of Spherical Particles.* Journal of the American Ceramic Society 44 (1961) 513-522

[66] Ower E, Pankhurst R C. *The Measurement of Air Flow, 5th Edition*. Pergamon Press (1977)

[67] Leong K C, Liu Y. *System performance of a combined heat and mass recovery adsorption cooling cycle: A parametric study.* International Journal of Heat and Mass Transfer 49 (2006) 2703-2711